Sergiy Taylakov

Fluid-Structure Interaction Between a Piezoelectric Microactuator and a Flexible Membrane in a Fluid Channel

Sergiy Taylakov

A dissertation

submitted in partial fulfillment of the

requirements for the degree of

Doctor of Philosophy

University of Washington

2020

Reading Committee:

I. Y. (Steve) Shen, Chair

Joseph Garbini

John Kramlich

Program Authorized to Offer Degree:

Mechanical Engineering

University of Washington

Abstract

Fluid-Structure Interaction Between a Piezoelectric Microactuator and a Flexible Membrane in a Fluid Channel

Sergiy Taylakov

Chair of the Supervisory Committee:
Professor I. Y. (Steve) Shen
Department of Mechanical Engineering

An intracochlear lead-zirconate-titanate (PZT) microactuator can complement a cochlear implant electrode array to rehabilitate hearing loss patients with enhanced speech recognition. The presence of the intracochlear microactuator can significantly alter the cochlear dynamics because the actuation now results from the microactuator instead of the stapes. To understand the effect of the microactuator on the cochlear dynamics, a test rig that mimics the box model of a human cochlea was designed. The test rig consists of two connected fluid channels, one aluminum membrane sandwiched between the channels, and a PZT thin-film microactuator. Since the actuators are manufactured using a very complex process, they are not identical. To account for variability, three test rigs employing three different actuators are created. For each one, frequency response functions of the microactuator and the aluminum membrane are measured using a laser Doppler vibrometer and a spectrum analyzer. Measurements are taken when the microactuator is in air, in a petri dish surrounded by oil, and in the fluid channel inside the test rig. In addition to frequency response measurements, the distance between the actuator and aluminum membrane inside the test rig is measured using the camera with fixed focal length and adjustable position. When microactuators are moved from air into the petri dish, their natural frequencies drop because of the added mass of surrounding oil. When microactuators are moved from the petri dish (i.e., an open environment) to the inside of the fluid channels (i.e., a closed environment), their natural frequencies drop further indicating additional increase in inertia. Two out of three actuator also experience the drop in static gain when they are moved from the petri dish into the channel, indicating an increase in stiffness. After the review of the squeeze film theory, the drop in static gain is attributed to experimental inaccuracy. The cause of the inaccuracy is discussed. The inertial effect is investigated using finite element method in commercial software Ansys Acoustics. Several models are proposed. The simplest model neglects the motion of the membrane. It is used to study the effect of model uncertainties and to capture the behavior of actuators in air and petri dish. Its inability to capture the behavior of the actuators in the channel indicates that membrane motion cannot be neglected, and the inertial effect is caused by the coupling of the actuator and membrane via fluid in between. A model that includes a very stiff membrane is able to capture natural frequencies in the channel, but unable to explain the phase difference between the actuator and membrane. The membrane mode shapes are extracted using principal component analysis to explain the deficiency of the model, and to justify the need for a full model of the test rig. The full model provides a valuable insight in the physic of interaction between the actuator, fluid, and membrane inside the test rig.

TABLE OF CONTENTS

LIST OF FIGURES

LIST OF TABLES

Chapter 1. INTRODUCTION

Hearing is one of the five senses that allows a human to perceive its surroundings. Scientists and physicians have long studied how hearing is transduced. When sound waves enter the ear channel, the sound waves move the ear drum and subsequently the stapes that connects to cochlea. Inside the cochlea, two fluid channels, known as scala vestibuli and scala tympani, lie side-by-side, separated by a basilar membrane, as shown in Figure 1.1. The two channels ascend together in the form of a conical helix (like a snail shell) and are connected at the apex of the helix via a hole in the basilar membrane called helicotrema. The lower end of the scala vestibuli is connected to the stapes, which moves like a piston generating pressure waves in the two fluid channels. The pressure difference from the two fluid channels then vibrates the basilar membrane, transducing the incoming sound waves to the sense of hearing via hair cells residing on the basilar membrane.

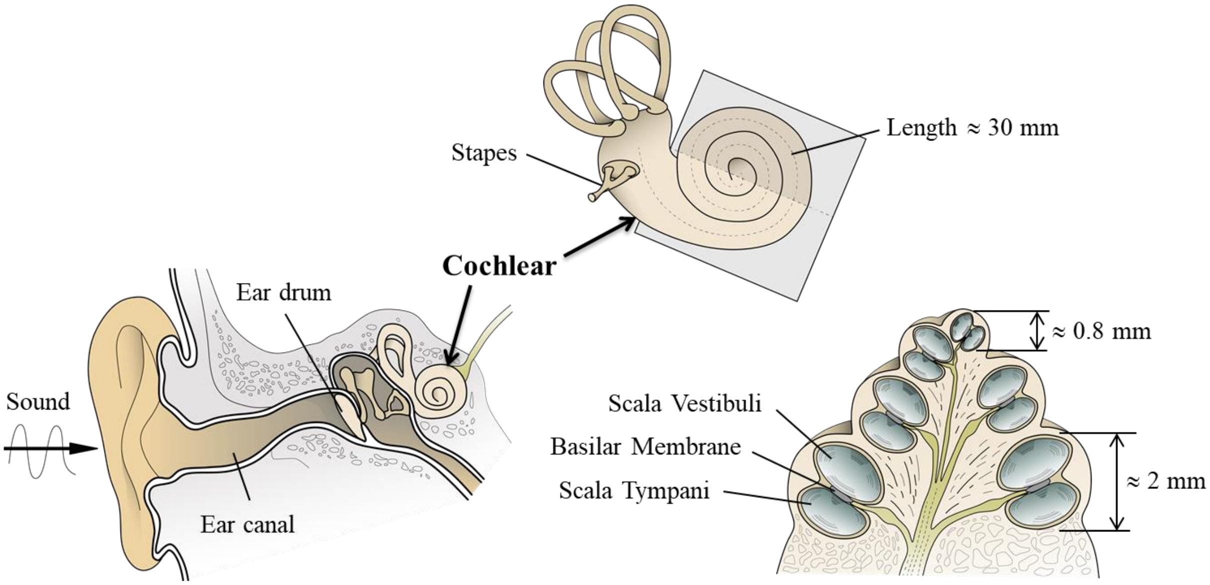

Figure 1.1. Image of the cochlear

To study cochlear dynamics, many researchers have used a box model to simulate the spiral of the cochlear; see Figure 1.2 [1-6]. The spiral is straightened, and the fluid channels are rectangular in cross section. The fluid domains are modeled as acoustic media satisfying wave equations. The basilar membrane is modeled as an elastic medium with a given distribution of impedance. The stapes' motion at one end of the scala vestibuli is modeled as a change in the displacement boundary condition. The acoustic transmission path is stapes, fluid, basilar membrane, and hearing transduction. Mechanically, it is a two-way coupling between the fluid and the basilar membrane.

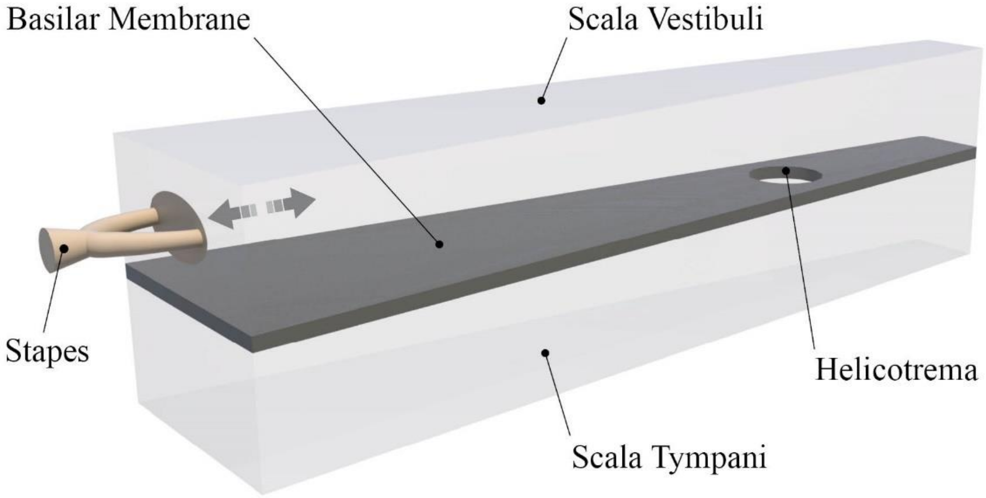

Figure 1.2. Current box model from literature

In the past, people who suffer total hearing loss received a cochlear implant, which is in the form of an electric array placed in the scala tympani, to stimulate hearing nerves electrically, bypassing the hair cells on the basilar membrane. In the last 10 years, there is a new treatment in hearing rehabilitation, known as combined electric and acoustic stimulation [7-11]. The new treatment combines a cochlear implant with a traditional, acoustics-based hearing aid that stimulates hearing by amplifying sound waves transmitted into the cochlea. The combination of electric and acoustics stimulation not only enhances speech recognition in noisy environments, but also substantially enlarges patient population because patients with residual hearing are also qualified for such treatment [8].

The acoustic stimulation component is not limited to traditional hearing aids placed in an ear channel. The acoustic stimulation could come from an intracochlear microactuator placed in the scala tympani. For example, Luo et al. fabricated and tested a lead-zirconate-titanate (PZT) thin-film microactuator probe as an intracochlear stimulation device [12] and demonstrated its feasibility via animal tests [13]. The intracochlear microactuator does not have the drawback with traditional hearing aids of blocking the ear channel leading to loss of sound quality, discomfort, and increased ear channel infection. The intracochlear microactuator can also integrate into a single device with cochlear implants because they are both placed inside the scala tympani.

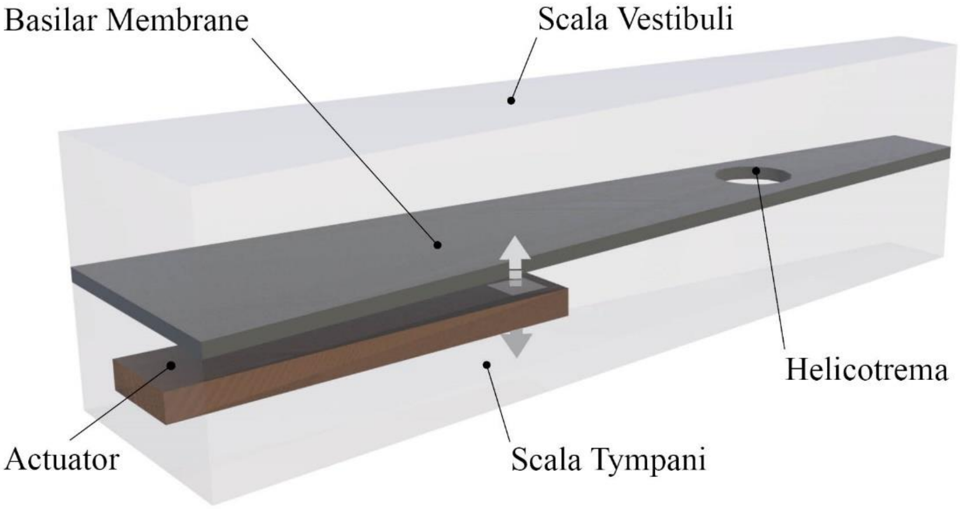

Figure 1.3. A new box model with an intracochlear actuator

The presence of intracochlear acoustic actuators, however, fundamentally changes the classical cochlear dynamics in several ways; see Figure 1.3. First, there is no stapes motion, as evident from the animal tests [13]. To generate the hearing, the actuator drives the basilar membrane locally via a small gap of fluid in between. Mechanically, it is now a three-way coupling among the acoustic actuator, the basilar membrane, and the fluid in between. In this case, the classical cochlear dynamics do not quite apply, and a new model is needed to understand the actuator-fluid-basilar membrane interaction.

This work is a first attempt to study cochlear dynamics when the excitation source is an intracochlear acoustic microactuator in lieu of stapes movement. The goal is to understand the effect of the intracochlear acoustic microactuator on the cochlear dynamics. There are several challenges in this new study of non-classical cochlear dynamics. The first challenge is to create an experimental setup that truthfully and repeatedly reflects fundamental changes of cochlear dynamics when an intracochlear microactuator is placed. To overcome this challenge, a test rig was designed based on the box model shown in Figure 1.3 with 1:1 scale based on critical dimensions of human cochlea. Walls of the fluid channels are fabricated via 3-D printing. An aluminum membrane is used to separate the two fluid channels. One fluid channel is inserted with a PZT microactuator and both fluid channels are filled with clear, non-conductive, mineral oil. This experimental setup provides a proving ground for repeatable experiments and measurements.

The second challenge is low signal-to-noise ratios. The cochlea is a very sensitive organ; stapes motion on the order of a nanometer can generate sensible hearing. In contrast, motion of the aluminum membrane in the nanometer range is very hard to measure because it is too small, resulting in low signal-to-noise ratios. To overcome this challenge, many measurements are taken to average out the noise. Also, motion of the PZT microactuator and its surrounding is measured to provide additional physical insights of the system. Extra care must be taken when interpreting data that are very susceptible to noise contamination.

The third challenge is complexity of the experimental setup. There is always a tradeoff between complexity and practicality of the experimental setup. For the box model, it is well known that the interaction of the cochlear fluid (perilymph) in the fluid channels and the basilar membrane is the key mechanism generating the sense of hearing. The property of the basilar membrane, however, can vary with a wide range of complexity. For example, the basilar membrane can have non-uniform acoustic impedance in the form of [2,3]

$$Z(\omega) = i\omega m_0 + \frac{c_0}{i\omega} e^{-\alpha x} + \delta\sqrt{m_0 c_0} e^{-0.5\alpha x} \tag{1.1}$$

where m_0, c_0, α and δ are the mass, stiffness, rate, and damping constants. Also, x is the distance along the spiral of the cochlea from its base. The impedance in Equation 1.1 mimics postmortem cochlea response fairly well [1], but live cochlea has more complex impedance. It reveals a negative real part for some portion of the basilar membrane, implying that the basilar membrane has negative damping and is giving acoustic power into the fluid [1]. Such complex acoustic impedances are impossible to recreate in controlled experiments. When an intracochlear acoustic actuator is present, the exact mechanism to induce hearing is already unknown. Experimental setup employing realistic impedance for postmortem or live cochlea (cf. Equation 1.1) becomes impractical.

To overcome this challenge, an aluminum membrane is used in the experiment. Since the impedance of the aluminum membrane is well known, the only hypothesis or uncertainty present in the experiment is the fluid-structure interaction between the intracochlear actuator and the basilar membrane. Once the hypothesis is proved in experiments, a mathematical model can then be developed to predict the response, followed by more advanced mathematical models with a more realistic basilar membrane impedance to mimic what happens in real cochlea.

In addition to experimental study, the numerical study using finite element method needs to be employed to provide additional insight into the system. The numerical study comes with its own challenges. First challenge is related to the approach used in the finite element method. Modeling fluid-structure interaction problems may require enormous computational resources. The traditional approach is to model fluid and structural domains separately using Navier-Stokes and structural equations. At each time step, both equations must be solved, and the results from two domains must be exchanged. This method requires substantial computational power and time commitment neither of which might be available. To overcome this challenge, another approach is used. The fluid domain is modeled as an acoustic medium satisfying wave equation. With this approach, both fluid and structural domain can be modeled together. The fluid-structure interaction problem can then be discretized and solved at once using commercially available software such as Ansys Acoustics. This approach has shown to accurately predict the natural frequency of the microactuator in the infinite fluid domain [14]. Its ability to explain the interaction of the actuator with aluminum membrane inside the fluid channel is to be determined.

Another challenge that comes with numerical study is the complexity of finite element model. The geometry of the experimental rig has a very high aspect ratio. Creating a consistent mesh for such geometry while keeping the size of the model at a reasonable level is a challenge. To complicate the matter, the structure of the microactuator is very complex. The thickness of the vibrating portion of the actuator is only a few microns. Moreover, it consists of several layers of different materials including PZT. If each layer is modeled, the resulting size of the model can become overwhelming even for a non-traditional approach. To overcome this challenge, the vibrating portion of the actuator is modeled using a homogeneous material without piezoelectric properties. Such approach is proven to work as demonstrated in [14]. However, with this approach, there is a lot of uncertainty in the material properties that should be used in the model. In addition, the real geometry of the actuator deviates from intended due to the complexity of manufacturing process. Measuring real geometry is impossible without destroying the actuator. This adds to uncertainty in model parameters. How these uncertainties affect numerical results needs to be investigated.

The rest of the dissertation is structured in the following way. First, the experimental setup that was used to identify the mechanism for intracochlear actuators to induce hearing is explained. Then the experimental data is presented, and the observations are discussed. The inconsistency in experimental observations leads to the review of the squeeze-film theory. Finally, several finite elements models of increasing complexity are developed. Each model serves a particular purpose. The simulated results from each model are explained and compared to the results obtained in the experiment. To supplement the comparison, the vibration mode shapes of the membrane are extracted along the way using principal component analysis.

Chapter 2. EXPERIMENTAL SETUP

The experimental setup includes a fixture, a piezoelectric actuator, and an instrumentation system consisting of precision two-axis stage, a power amplifier for piezoelectric devices, a laser Doppler vibrometer (LDV), and a spectrum analyzer.

2.1 FIXTURE

A one-of-a-kind fixture was created to mimic the box model in Figure 1.3. The fixture has two trapezoidal cavities mimicking the scala vestibuli and scala tympani (cf. Figure 1.1). In addition, a sheet of aluminum foil separates the two trapezoidal cavities mimicking the basilar membrane (cf. Figure 1.1). A hole was created on the aluminum foil by using a needle to mimic helicotrema. The design process took several iterations. The goal was to create a leakproof fixture that can be manufactured easily and repeatedly to account for the variability in actuators. A photo of the final design of the fixture is shown in Figure 2.1. In fact, the fixture has several components, which were manufactured separately and assembled together. The manufacturing and assembly process are explained as follows.

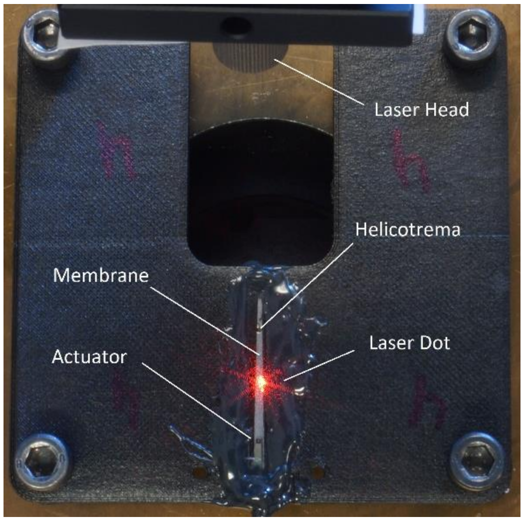

Figure 2.1. Photo of the fixture

The fixture has two components fabricated from polylactic acid (PLA) via 3D printing. One component has a first fluid channel to mimic scala vestibuli, and the other has a second fluid channel to mimic scala tympani. The two components, with the aluminum foil in between, were snapped together to form the fixture; see Figure 2.2. A PZT thin film microactuator [12] was placed in the second fluid channel near the wide side facing the aluminum foil. The cavity was complete by closing it with glass on both sides of the foil. Epoxy was used to glue the actuator in place, to close the cavity, and to secure the glass. It was then filled with UltraPro® Food Grade White Mineral Oil through the two holes drilled through the narrow side, and then sealed.

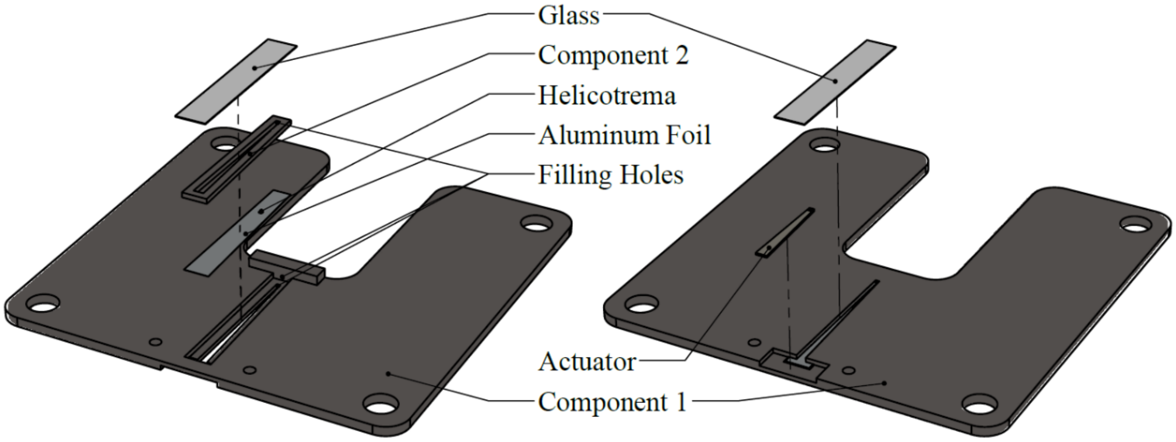

Figure 2.2. An exploded view of the fixture: (left) top side to mimic scala vestibuli, and (right) bottom side to mimic scala tympani

Dimensions of the fixture were largely guided by those of human cochlea [15-17]. In human cochlea, typical dimensions of the fluid channels (i.e., scala vestibuli and scala tympani) are on the order of 2 mm near the entrance region (e.g., stapes) and decrease to about 800 μm near the apex. The fluid channels make 2.5 turns, and the typical length of the basilar membrane along the cochlea is on the order of 25-30 mm (cf. Figure 1.1). Based on these dimensions, the two trapezoidal cavities of the fixture where designed to be 2 mm and 800 μm wide at the wide and narrow ends, respectively. However, the actual dimensions measured after the fixture was printed were 1800 and 600 µm at the wide and narrow ends, respectively. In addition, the two trapezoidal cavities both had a depth of 1 mm and a length of 30 mm. The thickness of the aluminum foil was 100 µm. The hole was created using an 800-µm diameter needle and was located at 23 mm from the wide side of the cavity.

2.2 ACTUATOR

Figure 2.3 shows schematic and dimensions of the PZT thin film microactuator used in the experiment. Its complete description including manufacturing process can be found in [12]. There are two main parts. The actuator's plate portion is the driving surface vibrating like a speaker. The actuator's beam portion is the supporting and anchoring structure for the plate portion.

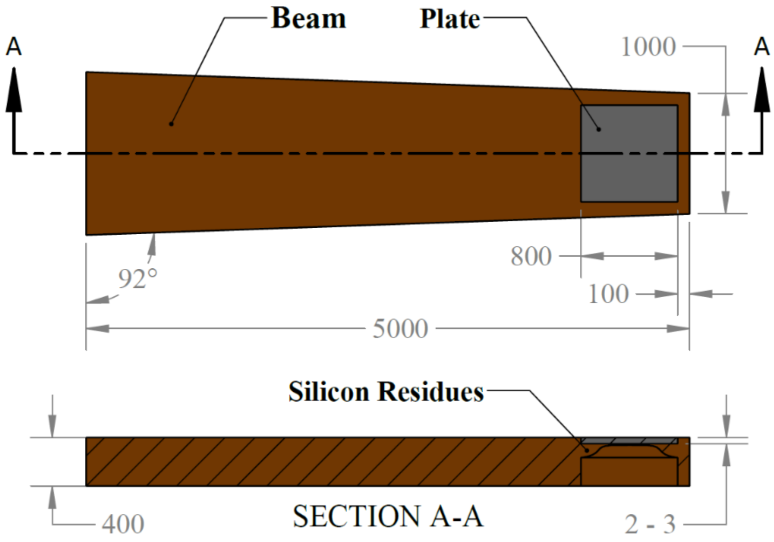

Figure 2.3. Schematics and dimensions of the actuator (µm)

The actuator's plate is very thin (2-3 µm by design) and has a complicated structure. There are multiple layers of different materials stacked on top of each other (e.g., top electrode, PZT, bottom electrode, bonding material, and base material). Moreover, there are silicon residues left after manufacturing process. The amount of silicon residues as well as the thickness of each layer are hard to control during manufacturing. As a result, the effective area of the actuator's plate is smaller than designed; its effective thickness is larger. The uncertainties in geometric parameters affect the mass and stiffness of each actuator. As a result, their natural frequencies vary. To account for this variation, three actuators were tested (labeled as Actuators 1, 2 and 3).

Each actuator was placed in its dedicated fixture approximately 5 mm from the wide side of the fixture, such that the actuator's plate was facing aluminum membrane. The distance between the actuator and the membrane could not be controlled during the assembly due to the small size of the setup and the minute movement of the actuator during epoxy curing. As a result, the distance was measured after the actuator was placed in the channel using the camera with a fixed focal length and adjustable position. Extreme care was taken to align the actuator along the channel parallel to the membrane, and to ensure that the actuator is not touching the membrane or the glass. However, after the epoxy has cured, it became clear that the alignment was not perfect.

2.3 INSTRUMENTATION SYSTEM

The instrumentation system consists of a precision two-axis stage, a power amplifier for piezoelectric devices, a laser Doppler vibrometer (LDV), and a spectrum analyzer as shown in Figure 2.4. The LDV was first fixed in space. Then the fixture was placed on the two-axis stage, which adjusted the relative position of the fixture and the laser dot from the LDV. Next, the spectrum analyzer sent a reference signal to drive the PZT thin-film actuator via the power amplifier. The LDV measured the velocity of the actuator (at the plate portion and occasionally at the beam portion) as well as the aluminum foil at various locations. The LDV measurements and the driving voltage from the power amplifier were sent to the spectrum analyzer to obtain frequency response functions (FRF).

The spectrum analyzer used in the experiment was from Stanford Research Systems model SR785. The swept sine mode was used to measure amplitude and phase of FRFs at 2047 (limit of the device) equally spaced points. The frequency range was adjusted for a particular measurement. The maximum frequency that device could operate with was 100 kHz. Because of this limitation, the natural frequencies of actuators 2 and 3 in air could not be determined. The dynamic range and averaging features were used for all measurements to increase the resolution, and to reduce noise.

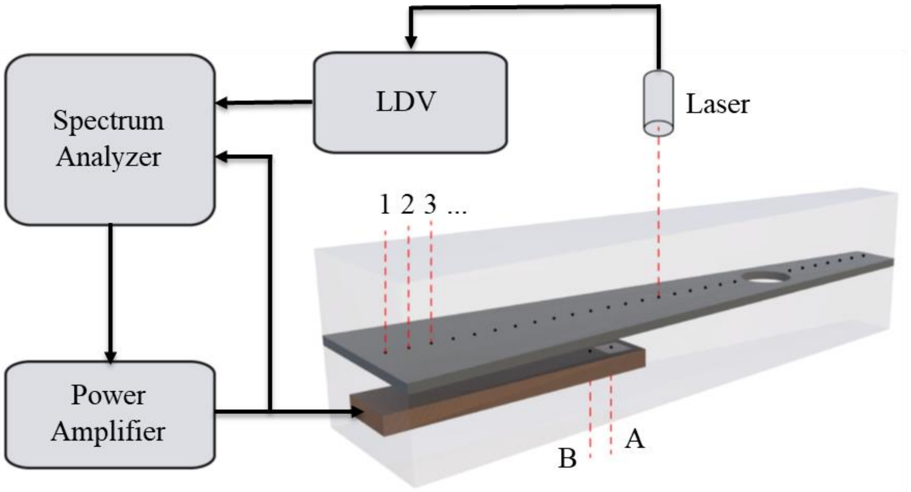

Figure 2.4. Instrumentation system

The LDV used in the experiment was from Polytec consisting of controller OFV-3001 and a sensor head OFV-511. The LDV has two velocity decoders: OVD-01 and OVD-02. OVD-01 has smaller bandwidth and a smaller signal-to-noise ratio. In contrast, OVD-02 has larger bandwidth and a larger signal-to-noise ratio. Both encoders were used in the experiment depending on the level of the noise. OVD-01 was used for all measurements, especially for the aluminum membrane due to its small displacement. OVD-02 was primarily used for actuator measurements.

Chapter 3. EXPERIMENTAL RESULTS

To study how the PZT thin-film microactuator interacted with the aluminum membrane and the fluid channels, the FRF measurements were conducted in sequence. First, FRF of the PZT microactuator was conducted in air. Since the bandwidth of the actuator in air is relatively large (compared to the bandwidth in oil), OVD-02 decoder was used for the measurements. FRF functions was obtained at 2047 data points equally spaced in the frequency domain between 1 and 100 kHz. The number of data points, as well as the upper frequency bound, were limited by the capabilities of the frequency analyzer. The lower frequency bound was set to achieve two counter dependent objectives. On one hand, higher lower bound would increase the resolution of the FRF in the region of interest (in the vicinity of the resonance frequency). On the other hand, low frequency region provides information about the stiffness of the system, which can be valuable for the analysis. Lower frequency bound of 1 kHz was chosen as a compromise. The velocity range was selected to maximize signal to noise ratio without saturating the decoder. Thus, for actuator 1 where the resonance peak was withing the range of the measurement, the velocity range was set to 25 mm/s/V. For actuators 2 and 3, where the resonance peak was outside the measurement range, the velocity range was set to 5 mm/s/V.

Next, the PZT microactuator was submerged in the mineral oil in a petri dish. FRF measurements were conducted to identify the effects of fluid in open environment. Since the bandwidth of the actuator in oil is much smaller than in air, OVD-01 decoder was used for the measurements, and the upper frequency bound was reduced to 50 kHz. The lower frequency bound and the number of data points were unchanged. The velocity range of 5 mm/s/V was used for all actuators. To fix the actuator inside the petri dish filled with oil, a special fixture was manufactured using 3D printing. Care was taken to ensure that the thickness of the fluid layers below and above the actuator was at least 2 mm. Under this arrangement, the actuator behaves as if it was submerged in the infinite fluid domain [14]. The fixture had a low bending stiffness. As a result, the FRFs were contaminated by small resonance peaks in the low frequency region.

Finally, the PZT microactuator was placed in the fluid channels inside the fixture, and the FRFs were measured again. The orientation of the actuator was such that its plate portion (cf. Figure 2.3) was facing aluminum foil. It was not possible to measure FRFs from the front of the actuator as it was done in air or petri dish. The measurements were conducted through the cavity on the back of the actuator (cf. Figure 2.3 and Figure 2.4 – Label A). This arrangement presented some challenges. To measure FRF using laser Doppler vibrometer the beam of light needs to be reflected back to the source. This task was very difficult to accomplish due to the misalignment between the actuator and the fixture. The diffraction from the edges of the cavity was contributing to the problem as well. To increase the confidence in the results, several measurements were taken for each actuator. The settings for the measurements were held the same as for the measurements in the petri dish. In addition, for actuator 2 and 3, the FRFs were also measured from the point on the beam near actuator’s plate (cf. Figure 2.3 and Figure 2.4 – Label B). OVD-02 decoder with 5 mm/s/V velocity range was used to measure FRFs from the beam inside the fixture between 1 and 100 kHz. A measurement with the same decoder and settings was also taken from the actuator’s plate for comparison.

Experimental results also contain FRF measurements at multiple points on the membrane when the actuator is inside the fluid channels of the fixture (cf. Figure 2.4). The measurement points were along the middle of the membrane, roughly 1 mm apart from each other (exact coordinates are provided in the Appendix A – C). OVD-01 decoder with velocity range set to 5 mm/s/V was used to take all measurements from the membrane. The frequency range was customized for each actuator to increase the resolution in the vicinity of the actuator’s resonance. Thus, for actuator 1 the FRFs were measured between 10 and 30 kHz, for actuator 2 – between 15 and 40 kHz, and for actuator 3 – between 5 and 40 kHz.

In summary, for each actuator, experimental results include FRF measurements from the actuator in air, in oil inside a petri dish, and inside the fixture, and measurements from the points along the membrane. Data collected for Actuators 2 and 3 also contain FRF measurements from a reference point on the actuator beam near the actuator plate. Each measured FRF contains 2047 data points equally spaced in the frequency domain. Table 3.1 summarizes instrument settings for each measurement. Appendix 1-3 provides plots of FRFs taken for actuator 1-3 respectively (all presented FRFs were converted to show deformation).

Table 3.1. Instrument settings used for the measurements

			Decoder	Frequency Range (kHz)	Velocity Range (mm/s/V)
Actuator 1	Air	Actuator	OVD-02	1 – 100	25
	Oil	Actuator	OVD-01	1 – 50	5
	Fluid Channel	Actuator	OVD-01	1 – 50	5
		Membrane	OVD-01	10 – 30	5
Actuator 2	Air	Actuator	OVD-02	1 – 100	5
	Oil	Actuator	OVD-01	1 – 50	5
	Fluid Channel	Actuator	OVD-01	1 – 50	5
		Beam/Plate	OVD-02	1 - 100	5
		Membrane	OVD-01	15 – 40	5
Actuator 3	Air	Actuator	OVD-02	1 – 100	5
	Oil	Actuator	OVD-01	1 – 50	5
	Fluid Channel	Actuator	OVD-01	1 – 50	5
		Beam/Plate	OVD-02	1 - 100	5
		Membrane	OVD-01	5 – 40	5

3.1 FREQUENCY RESPONSE FUNCTION MEASUREMENTS

To better understand experimental results, FRF measurements can be plotted on the same graph for comparison. In this section, the measurements from the actuator in air, oil, and fluid channels are compared first. Then, measurements from the actuator's beam and plate portion are compared. Finally, the membrane measurements are discussed. Only the magnitudes of selected FRFs are presented in this section. For the complete set, please refer to the appendix.

3.1.1 *Measurements from the Actuator's Plate*

Figure 3.1 shows the magnitude of FRFs of Actuator 1 measured in air, in oil, and inside the fluid channels. When Actuator 1 was in air, its natural frequency was 77.5 kHz, and its static gain (i.e., the flat portion of the FRF at low frequency) was about -160 dB. When Actuator 1 was submerged in the oil, the static gain remained roughly around -160 dB, but the natural frequency dropped to 21.6 kHz. (The several peaks below 10 kHz come from the fixture holding the actuator in the oil.) Note that the static gain is inversely proportional to the stiffness. Therefore, the absence of a significant change in the static gain indicates that the surrounding oil does not produce appreciable stiffness effect to Actuator 1. The drop of the natural frequency from 77.5 kHz to 21.6 kHz results from the added mass of the surrounding oil [14]. The drop of the natural frequency can also be predicted accurately via finite element analysis as demonstrated in [14].

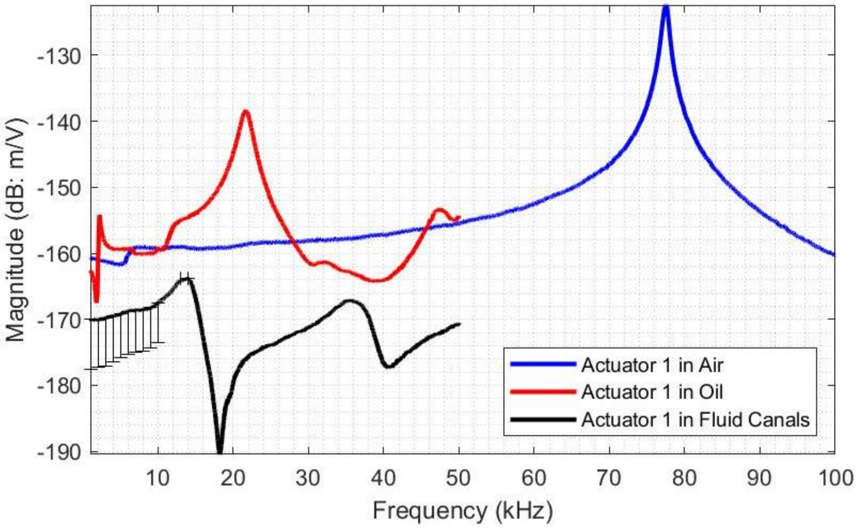

Figure 3.1. Magnitude of frequency response function of actuator 1 in air, oil, and in fluid channels

When Actuator 1 was placed inside the fluid channels facing the aluminum membrane, the static gain dropped significantly to -170 dB, and the natural frequency dropped further to 13.9 kHz (5 measurements have been made; therefore, error bars are also shown in Figure 3.1). The drop of 10 dB in the static gain indicates that the stiffness has increased roughly by $10^{0.5} \approx 3.16$ times. The drop in the natural frequency indicates that the mass effect has increase roughly by $(21.6/13.9)^2 \times 3.16 \approx 7.63$ times. Table 3.2 lists the comparison in natural frequencies and static gains.

Table 3.2. Static gains and natural frequencies from actuator measurements

	Actuator in Air		Actuator in Oil		Actuator in Fluid Channels	
	ω_N (kHz)	Static Gain (dB)	ω_N (kHz)	Static Gain (dB)	ω_N (kHz)	Static Gain (dB)
Actuator 1	77.5	-160	21.6	-160	13.9	-170
Actuator 2	>100	-160	27.3	-160	22.2	-172
Actuator 3	>100	-160	30.3	-160	11.9	-160

Actuator 2 presents similar behavior. Figure 3.2 shows the magnitude of FRFs of Actuator 2 measured in air, in oil, and inside the fluid channels. When Actuator 2 was in air, its natural frequency was above 100 kHz exceeding the measurement range of the frequency analyzer. Its static gain, however, was about -160 dB. When Actuator 2 was submerged in the oil, the static gain remained roughly around -160 dB, and the natural frequency dropped to 27.3 kHz. Again, the absence of significant change in the static gain indicates that no appreciable change in stiffness occurred when Actuator 2 was submerged in oil. The drop of the natural frequency to 27.3 kHz results from the added mass of the surrounding oil.

When Actuator 2 was placed inside the fluid channel facing the aluminum membrane, the static gain dropped significantly to -172 dB, and the natural frequency dropped further to 22.2 kHz. The drop of 12 dB in the static gain indicates that the stiffness has increased roughly by $10^{0.6}$

≈ 3.98 times. The drop in the natural frequency indicates that the inertial effect has increased roughly by $(27.3/22.2)^2 \times 3.98 \approx 6.00$ times. Therefore, the increase in stiffness and inertia when the microactuator is placed in the fluid channels is a repeatable observation. There is also a small peak around 30 kHz. It is not clear what that small peak represents.

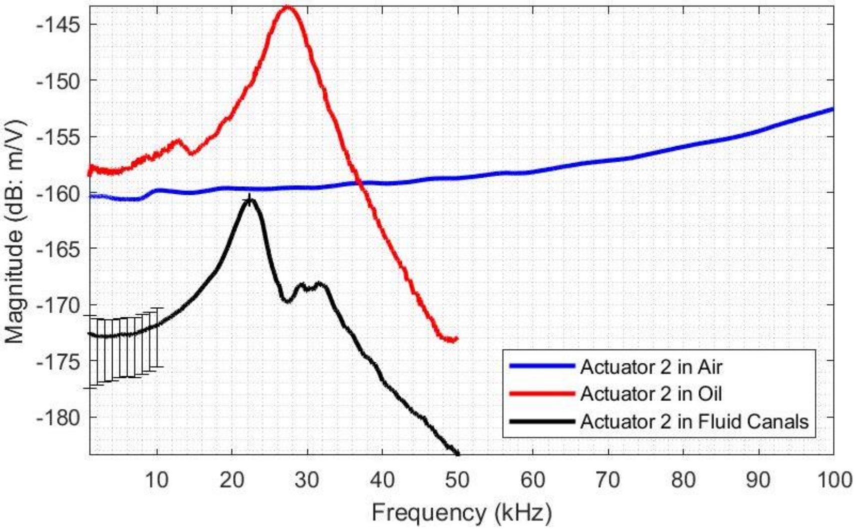

Figure 3.2. Magnitude of frequency response function of actuator 2 in air, oil, and in fluid channels

Actuator 3 presents somewhat different behavior. Figure 3.3 shows the magnitude of FRFs of Actuator 3 measured in air, in oil, and inside the fluid channels. When Actuator 3 was in air, its natural frequency was above 100 kHz exceeding the measurement range of the instruments. Its static gain, however, was about -160 dB. When Actuator 3 was submerged in the oil, the static gain remained roughly around -160 dB, and the natural frequency dropped to 30.3 kHz. Again, the absence of significant change in the static gain indicates that no appreciable change in stiffness occurred when Actuator 3 was submerged in oil. The drop of the natural frequency to 30.3 kHz results from the added mass of the surrounding oil. The frequency response function also contains several other small peaks. Peaks in the low frequency region (below 10 kHz) come from the fixture. The origin of the peak above 30 kHz is not clear.

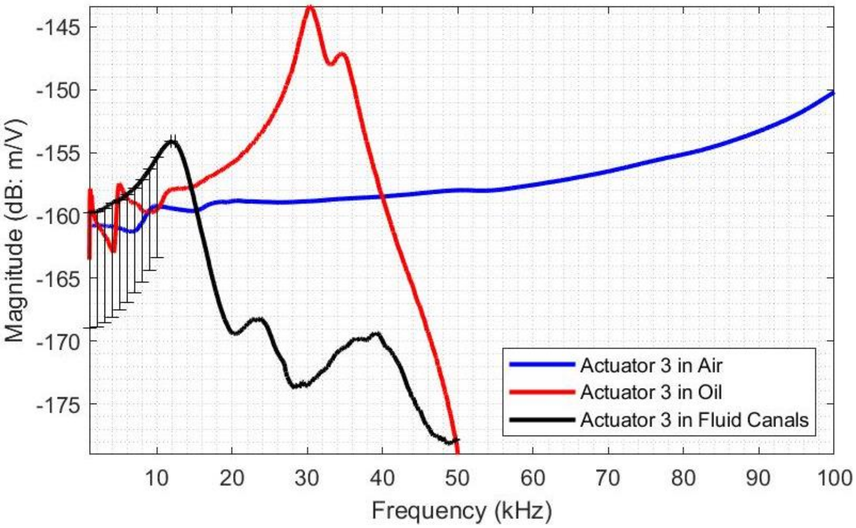

Figure 3.3. Magnitude of frequency response function of actuator 3 in air, oil, and in fluid channels

When Actuator 3 was placed inside the fluid channel facing the aluminum membrane, the natural frequency dropped further to 11.9 kHz. The static gain, however, remained unchanged at -160 dB. The constant static gain indicates that the stiffness has not changed. The drop in the natural frequency indicates that the inertial effect has increased roughly by $(30.3/11.9)^2 \approx 6.48$ times. The frequency response function also contains a couple of small peaks above 20 kHz. Their origin is not clear.

In summary, all three actuators show similar behavior when they are moved from air into the petri dish filled with oil. The static gain of the actuators remains unchanged, while the natural frequency drops. This is consistent with previous observations [14]; the reduction in natural frequency is caused by the added mass of the surrounding fluid. When actuators are moved inside the fluid channels, their behavior exhibits a similarity as well as a difference. The natural frequency of all actuators drops further when they are moved inside the fluid channels. This is a very consistent measurement as indicated by narrow horizontal error bars in Figure 3.1 – 3.3. The static gain, however, drops for actuators 1 and 2, but remains roughly unchanged for actuator 3. Also, the error bars for this measurement are quite large. The inconsistency in observation together with a large variation in static gain measurements are raising a natural question. Is the decrease in static gain for actuator 1 and 2 caused by a physical phenomenon or experimental inaccuracy? This question will be addressed in Section 3.3.

3.1.2 *Measurements from the Actuator's Beam*

Figure 3.4 compares the measured response of the actuator 2 at the plate and the beam portions. There are several observations that can be made from this measurement. First, the beam is vibrating. The FRF of the beam shows several peaks. At least two of those peaks coincide with the peaks from the FRF of the actuator's plate. Second, the largest response of the actuator's beam occurs at the frequency that coincides with the second peak on the FRF of the actuator's plate. One may expect that the largest response of the beam occurs when the beam vibrates in its first natural mode. Therefore, this observation may help explain the origin of the second peak on the FRF of the actuator's plate. Lastly, the response of the actuator's beam is extremely small, with the largest displacement being -194 dB. Such a small measurements must be interpreted with extra care.

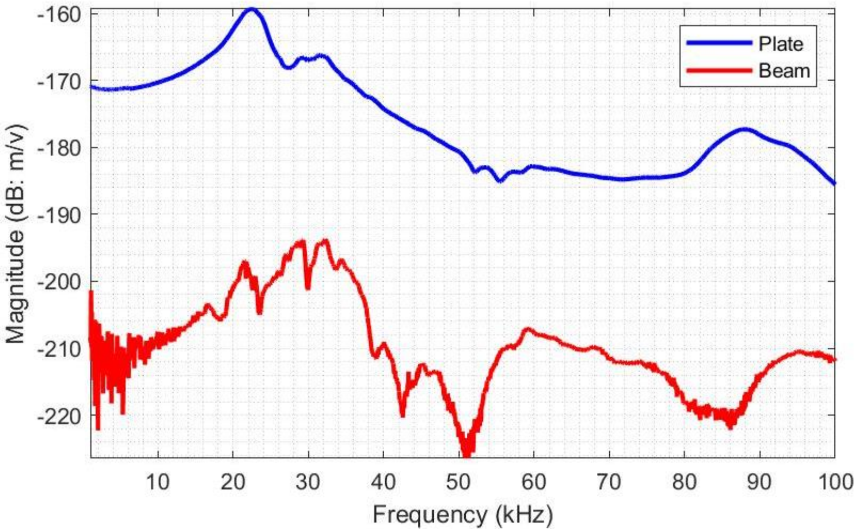

Figure 3.4. Magnitude of frequency response function of the actuator's beam and plate portion inside the fluid channels for actuator 2

Figure 3.5 compares the measured response of the actuator 3 at the plate and the beam portions. Similar observation can be made. First, there are peaks on the FRF of the beam that coincide with peaks from the FRF of the plate. Second, the largest response of the actuator's beam occurs at the frequency that coincides with the second peak on the FRF of the actuator's plate. Although, the response of the actuator's beam is extremely small and must be interpreted with extra care, the similarity between measurements from actuator 2 and 3 increases the confidence in the results from the actuator's beam.

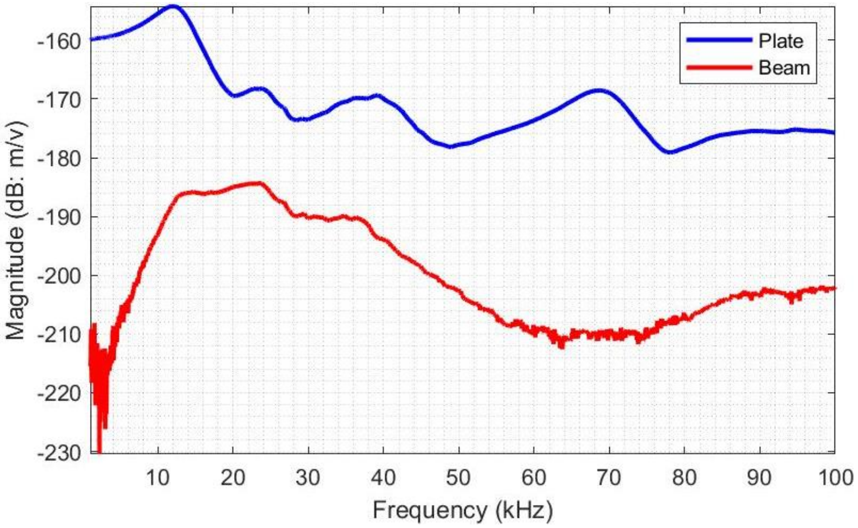

Figure 3.5. Magnitude of frequency response function of the actuator's beam and plate portion inside the fluid channels for actuator 3

3.1.3 *Measurements from the Membrane*

Figure 3.6 shows the magnitude of FRF measurements of selected points on the Aluminum membrane for the case of Actuator 1. Point 4 is roughly above the actuator plate portion, point 13 is around the mid-section of the membrane, and point 28 is at the narrow end of the aluminum membrane (i.e., far away from the actuator).

There are several issues worth noting from these measurements. First, the response of the aluminum membrane is extremely small. The largest amplitude is -186 dB occurring around 14 kHz. This corresponds to a displacement of 0.5 nm and a velocity of 44 μm/s, which is certainly approaching measurement limits of LDV. With such small measurements, noise can easily compromise the level of confidence in the measurements. Therefore, the measured FRFs of the aluminum membrane should be interpreted very carefully. Second, there are many small but local peaks as seen from the measured FRFs of the aluminum membrane. It is not clear whether these peaks truly reflect a resonance condition or simply result from noise compromising the experimental measurements. Third, the membrane response at the resonance around 13.9 kHz is larger than response from any off-resonance frequencies (e.g., 10 kHz). Finally, the amplitude difference between the actuator and the membrane is at least one order of magnitude. For example, the resonance amplitude of the actuator plate portion is -164 dB, which is 22 dB larger than the largest resonance amplitude of all points on the membrane. The difference is even larger if the amplitude of the static gains is used for comparison.

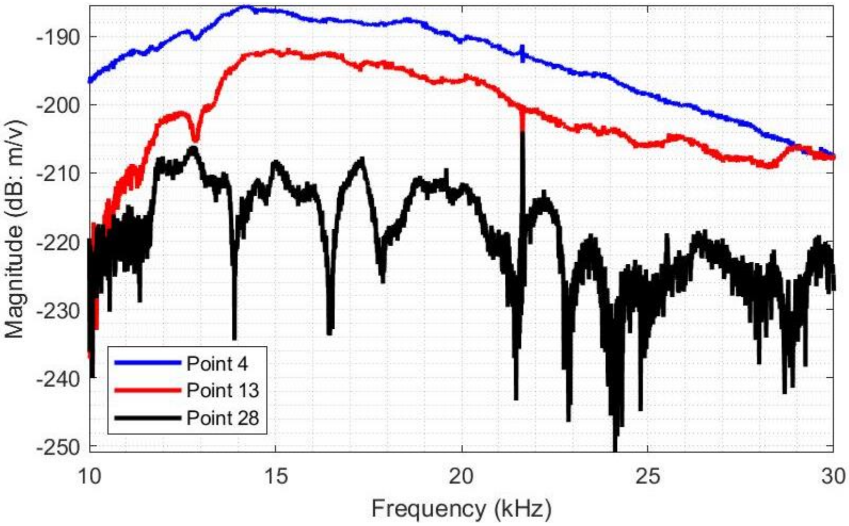

Figure 3.6. Magnitude of frequency response function of the aluminum membrane for actuator 1

Figure 3.7 shows the vibration amplitude of various points along the membrane for the resonance condition at 13.9 kHz and an off-resonance conditions at 10 and 20 kHz for the case of Actuator 1. Since the vibration amplitude is so small, interpretation based on individual data point could be extremely misleading. Nevertheless, the measurements collectively indicate two important trends. First, the vibration amplitude of the membrane tends to become smaller toward the narrow end (i.e., away from the actuator). Second, the off-resonance membrane response is generally smaller than the resonant response. Although dips appear both in the resonant and off-resonance conditions, it is not clear if the dips do represent nodal points given the small displacement measured throughout the membrane.

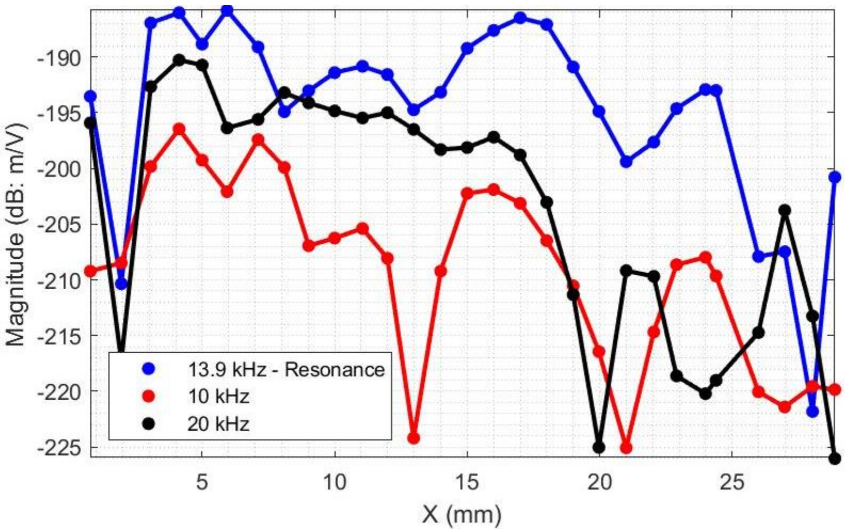

Figure 3.7. Measurements of membrane amplitude at resonant and off-resonance conditions for actuator 1

Figure 3.8 shows the magnitude of FRF measurements of selected points on the Aluminum membrane for the case of Actuator 2. Again, point 4 is roughly above the actuator plate portion, point 13 is around the mid-section of the membrane, and point 28 is at the narrow end of the aluminum membrane. Almost identical phenomena are observed here as in the case of Actuator 1. The response of the membrane is extremely small, with -188 dB as the largest amplitude near the actuator resonance roughly around 22.2 kHz. Many small peaks appear in the FRF measurements, and it is not clear if the peaks truly reflect a resonance condition or simply result from contamination by the measurement noise. Also, the membrane amplitude is at least one order-of-magnitude smaller than the magnitude of the actuator's plate, (i.e., -188 dB vs. -160 dB as shown in Figure 3.2).

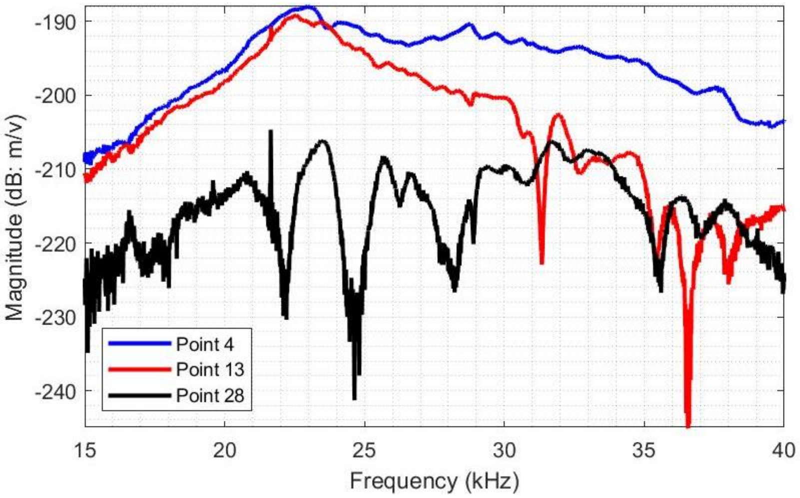

Figure 3.8. Magnitude of frequency response function of the aluminum membrane for actuator 2

Figure 3.9 shows the vibration amplitude of various points along the membrane for the resonance condition at 22.2 kHz and an off-resonance conditions at 15 and 30 kHz for the case of Actuator 2. Similar trends are observed, i.e., membrane vibration tends to be smaller toward the narrow end, and the off-resonance membrane response is generally smaller than the resonant response.

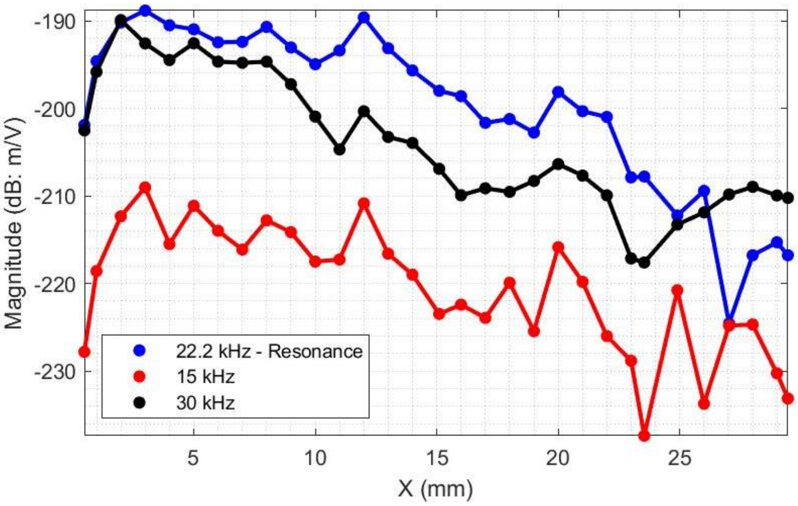

Figure 3.9. Measurements of membrane amplitude at resonant and off-resonance conditions for actuator 2

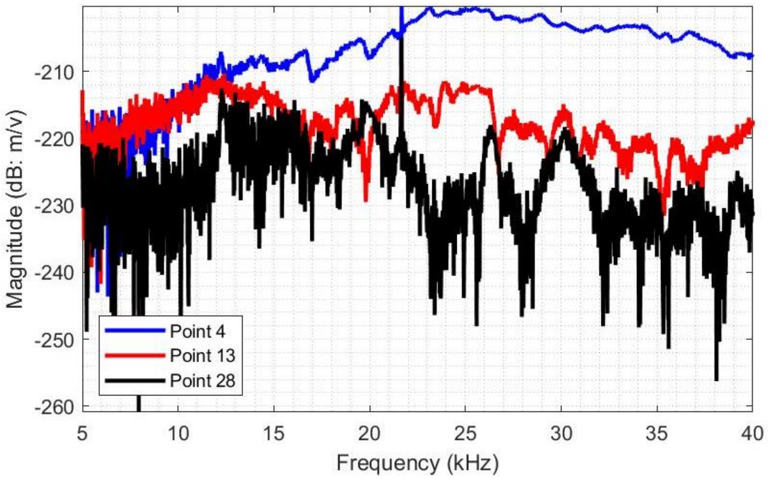

Figure 3.10. Magnitude of frequency response function of the aluminum membrane for actuator 3

Figure 3.10 shows the magnitude of FRF measurements of selected points on the Aluminum membrane for the case of Actuator 3. Again, point 4 is roughly above the actuator plate portion, point 13 is around the mid-section of the membrane, and point 28 is at the narrow end of the aluminum membrane. Once again, measurements from actuator 3 present some similarities as well as some differences as compared with corresponding measurements from Actuator 1 or 2. As before, the response of the membrane is extremely small. Many small peaks appear in the FRF measurements, and it is not clear if the peaks truly reflect a resonance condition or simply result from contamination by the measurement noise. However, the membrane amplitude is much smaller for the actuator 3 than for actuators 1 and 2 (i.e., -200 dB vs. -190 dB). It is also two order-of-magnitude smaller than the magnitude of the actuator's plate, (i.e., less than -200 dB vs. -154 dB as shown in Figure 3.3). Furthermore, the amplitude of the membrane response is no longer dominant around the resonance frequency of the actuator. There is another region around 25 kHz where the amplitude of the membrane response is comparable, or even larger than at the frequency corresponding to the actuator's resonance. This is the region where the second peak on the actuator's FRF is observed, and where the magnitude of the FRF from the actuator's beam is dominant (see Figure 3.5).

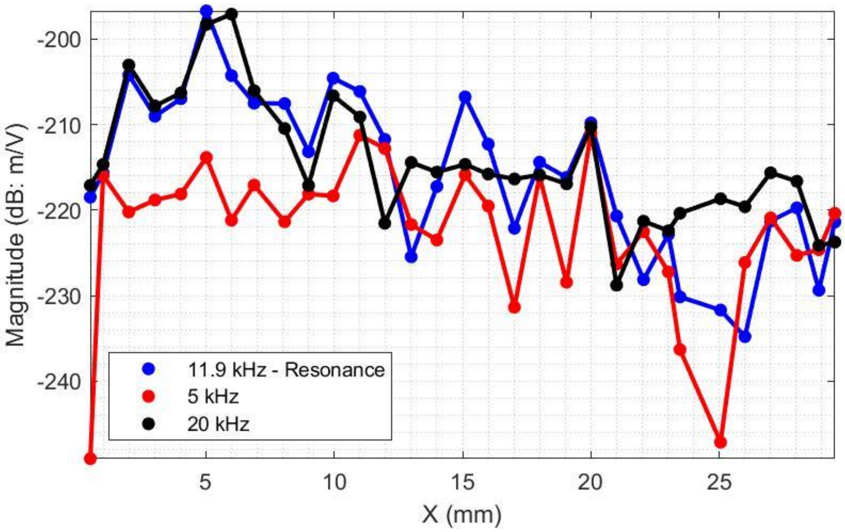

Figure 3.11. Measurements of membrane amplitude at resonant and off-resonance conditions for actuator 3

Figure 3.11 shows the vibration amplitude of various points along the membrane for the resonance condition at 11.9 kHz and an off-resonance conditions at 5 and 20 kHz for the case of Actuator 3. As before, membrane vibration tends to be smaller toward the narrow end, but the resonant and off-resonance membrane responses are now comparable.

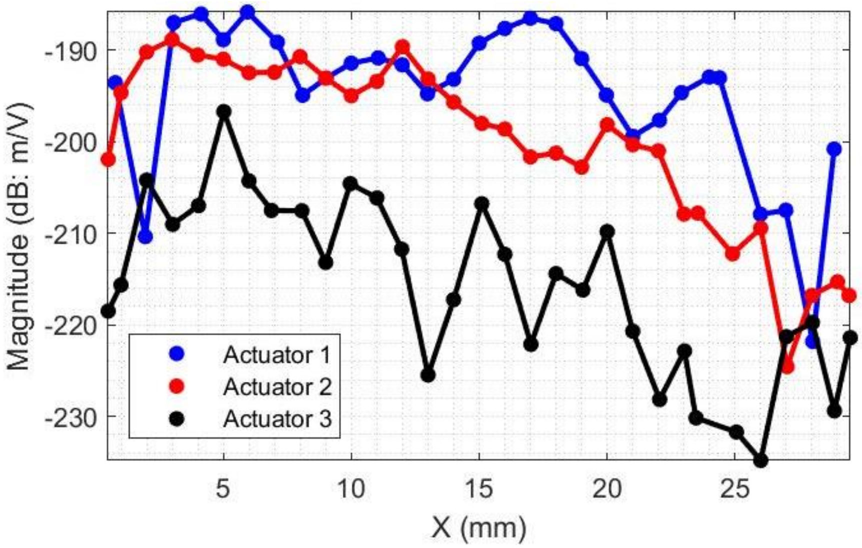

Figure 3.12. Comparison of membrane amplitude at resonant conditions for actuator 1, 2, and 3

Figure 3.12 is a comparison of the membrane response at the resonance for Actuators 1, 2 and 3. It shows that the membrane response follows the same patterns for all actuators. It also shows that the amplitude of the membrane response for actuator 3 is much smaller than for actuator 1 or 2. It is surprising, given that the amplitude of the actuator's response is the largest for actuator 3 (see Figure 3.1 – 3.3).

3.2 MEASUREMENTS OF THE DISTANCE BETWEEN ACTUATOR AND MEMBRANE

The distance between the actuator and membrane determines the thickness of the fluid film between the two surfaces. It is expected that the force acting on the actuator as well as on the membrane will depend on it. The knowledge of this parameter can be as important for the analysis as the knowledge of resonance frequencies. However, it was not possible to control the distance during the assembly process. The actuator was moving while the epoxy was settling; therefore, the distance between the actuator and membrane was measured afterwards.

The measurement was performed using a camera with adjustable position as follows. First, the camera was focused on the back of the actuator's beam (Figure 2.3), then on the back of the actuator's plate (Figure 2.3), and finally on the aluminum foil. To adjust the focus, the camera was moved normal to the plane of the actuator. The distance traveled by the camera between each surface in focus was recorded to estimate the distance between the actuator and aluminum foil.

Conceptually, only the measurement between the back of actuator's plate and the foil was necessary. However, there were few issues casting doubts on the accuracy of the measuring method. First, there is an uncertainty in the focal plane. It is not easy to tell when the surface is in focus. The error of ±20 μm can be easily attributed to guessing. Second, the actuator and the foil are not parallel. In addition, the experimental setup is not perfectly aligned with the camera. As a result, only a part of surface comes in focus during the measurement. This contributes to uncertainty in focal plane determination, further increasing the error. Lastly, the distance traveled by the camera during focal adjustment is not the same as the distance between corresponding surfaces. There is a refraction of light between the air and the glass as well as between the glass and the oil that needs to be considered. To estimate the distance between surfaces, the distance traveled by the camera needs to be multiplied by the index of refraction of the medium, which is unknown. A relatively large range of values can be found in the literature for different glasses and oils.

To estimate the accuracy of the measuring method, the measurement between the back of the actuator's beam and plate was made in addition to the measurement between the back of the actuator's plate and the foil. Since the thickness of the actuator's plate is negligible as compared to the thickness of the actuator's beam, the measured distance between the back of actuator's plate and beam portion should be approximately 400 μm (Figure 2.3). The error in this measurement would provide an insight about the accuracy of the method.

Two sets of measurements were taken for the Actuators 1 and 2, and a single set for the actuator 3. The results are reported in the Table 3.3. As seen, the method significantly underestimates the thickness of the actuator's beam; therefore, the measurement of the distance between the actuator and the membrane should be used carefully. One conclusion that can be made is that the actuator 3 is closest to the membrane, while actuator 2 is farthest.

Table 3.3. Measured distance

	Thickness of the Beam (μm)			Distance between the Actuator and Membrane (μm)		
	Set 1	Set 2	Average	Set 1	Set 2	Average
Actuator 1	230	182	206	221	258	240
Actuator 2	275	327	301	332	314	323
Actuator 3	-	278	278	-	60	60

3.3 ANALYSIS OF THE OBSERVED STIFFNESS EFFECT

The experimental results presented above prompt some important questions that require further study and investigation. First, what is the cause of the increased stiffness when the microactuator is placed in the fluid channels facing the aluminum membrane? One possible cause is the squeeze film effect of the fluid between the actuator and the aluminum membrane. According to [18], the squeeze force is inversely proportional to the thickness of the fluid film between the actuator and the aluminum membrane. When the actuator is placed inside the petri dish surrounded by oil, the bottom of the petri dish serves as a bearing surface and the gap between the actuator and the bearing surface is very large. When the actuator is placed inside the fluid channels facing the aluminum membrane, the aluminum membrane serves as a bearing surface. Consequently, the gap between the actuator and the aluminum membrane becomes so small that it significantly increases the squeeze force and the stiffness effect.

Another possible cause of the increased stiffness when the actuator is place in the fluid channels is the inaccuracy in experimental measurement. Laser Doppler vibrometer converts the phase difference between incident and reflected laser beams into the velocity measurement. When the surface velocity is not uniform (as in the case of microactuator’s plate fixed at all sides), the resulting measured value is some form of average velocity over the surface from which the beam is reflected. When the measurement is made from the front of the actuator, it is relatively easy to align the laser with the actuator’s plate, such that the entire laser beam is reflected from the vibrating structure. Even in this case the measurements can vary because the size of the laser dot is comparable to the size of the actuator’s plate. When the measurement is made from the back of the actuator, the alignment is much more challenging. A portion of the laser beam can be reflected from the surface of the actuator's beam. The velocity of actuators beam is negligible as compared to the velocity of the actuator's plate, and the magnitude of the measurement can be reduced.

As noted in Section 3.1.1, the error bars for the measurement in the low frequency region when the actuator is inside the fluid channels are quite large. This serves as an evidence supporting the idea that the stiffness effect is caused by the experimental inaccuracy. Additionally, Actuator 3, which is the closest to the membrane and where the increase in squeeze force should be the largest, does not show an increase in stiffness. This inconsistency further strengthens the argument. However, to attribute stiffness effect to the experimental inaccuracy, the squeeze film effect must be ruled out.

The squeeze film theory for compressible fluid is very well understood and can provide a valuable insight into the origin and nature of the squeeze force. It was developed over 40 years ago and has proven to predict squeeze force quite accurately (for the development and experimental verification refer to [19, 20]). According to the theory, the pressure distribution in the fluid, squeezed between two parallel plates undergoing motion in the normal direction relative to each other, is governed by the linearized Reynolds equation [21]:

$$p_a\left(\frac{\partial^2 p}{\partial x^2}+\frac{\partial^2 p}{\partial y^2}\right)-\frac{12\mu}{H^2}\frac{\partial p}{\partial t}=\frac{12\mu p_a}{H^3}\frac{\partial h}{\partial t} \tag{3.1}$$

where p_a is ambient pressure (10^5 Pa), p – deviatory pressure in the film, H film thickness, μ dynamic viscosity, h distance between two plates at time t. If the variables are normalized $\hat{p}=\frac{p}{p_a}$; $\hat{x}=\frac{x}{L}$; $\hat{y}=\frac{y}{L}$; $\hat{h}=\frac{h}{H}$; $\tau=\omega t$, Equation 3.1 can be written in non-dimensional form:

$$\frac{\partial^2\hat{p}}{\partial\hat{x}^2}+\frac{\partial^2\hat{p}}{\partial\hat{y}^2}-\sigma\frac{\partial\hat{p}}{\partial\tau}=\sigma\frac{\partial\hat{h}}{\partial\tau} \tag{3.2}$$

where σ is called the squeeze number:

$$\sigma=\frac{12\mu L^2}{P_a H^2}\omega \tag{3.3}$$

Here, L is the typical length of the plate and ω is the angular frequency. If the distance between plates varies harmonically according to:

$$h = H(1 + \delta\, cos(\omega t)) \tag{3.4}$$

where δ is the perturbation amplitude, Equation 3.2 can be solved to obtain the force on the square plate from the film [22]:

$$F = p_a L^2 \delta[-f_k(\sigma)\, cos(\omega t) + f_b(\sigma)\, sin(\omega t)] \tag{3.5}$$

where f_k and f_b are calculated using following equations:

$$f_k = \frac{64\sigma^2}{\pi^8} \sum_{m,n\ odd} \frac{1}{(mn)^2\left[(m^2+n^2)^2 + \sigma^2/_{\pi^4}\right]} \tag{3.6}$$

$$f_b = \frac{64\sigma}{\pi^6} \sum_{m,n\ odd} \frac{m^2+n^2}{(mn)^2\left[(m^2+n^2)^2 + \sigma^2/_{\pi^4}\right]} \tag{3.7}$$

The resulting force has two components. One is in phase with the motion of the plate. Its behavior is analogous to the behavior of the spring force. The other component is shifted in phase by the quarter of the cycle. Its behavior is analogous to the behavior of a viscous damping force. The non-dimensional amplitudes of these components, given by Equations 3.6 – 3.7, are plotted in the Figure 3.13.

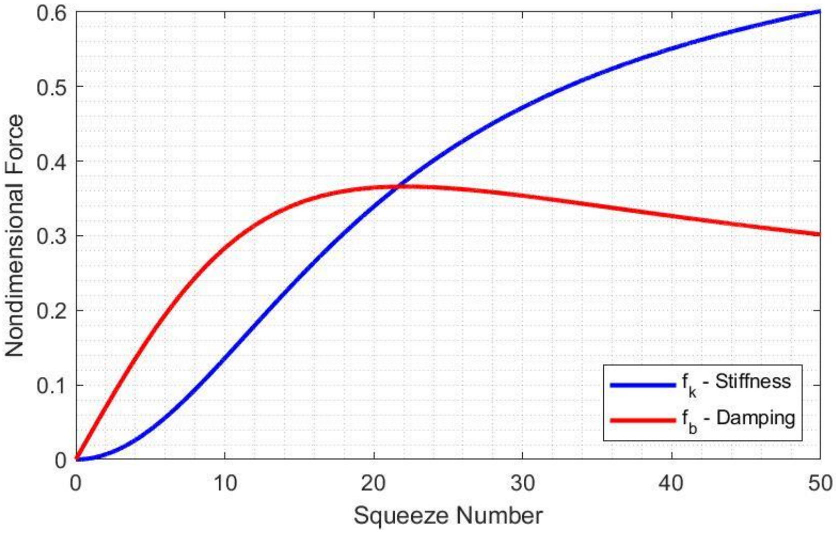

Figure 3.13. Non-dimensional amplitude of squeeze force

The central parameter in the squeeze film theory for compressible fluids is the squeeze number given by Equation 3.3. It is a measure of the compressibility of the film [23]. When the squeeze number is low, the fluid has time to escape during the motion of the plate. The viscosity, however, resists its motion providing effective damping force. In this region, the damping force is dominant. When the squeeze number is high, as in the case when the frequency of oscillation is high or the gap between plates is very small, the fluid does not have time to escape and begins to compress. In this region, the spring force is dominant. At the critical squeeze number, the damping force is equal to the spring force. For the square plate, the critical squeeze number is roughly 21 (Figure 3.13).

Figure 3.14 displays calculated squeeze number for actuators 1 and 2 in the low frequency region. It is calculated using Equation 3.3 with $\mu = 0.02\ Pa \cdot s$. As evident, the squeeze number in this region is very small for both actuators. Referring to Figure 3.13, the corresponding stiffness force must be negligible. Therefore, based on the squeeze film theory for compressible fluids, the observed stiffness effect can be attributed to the experimental inaccuracy.

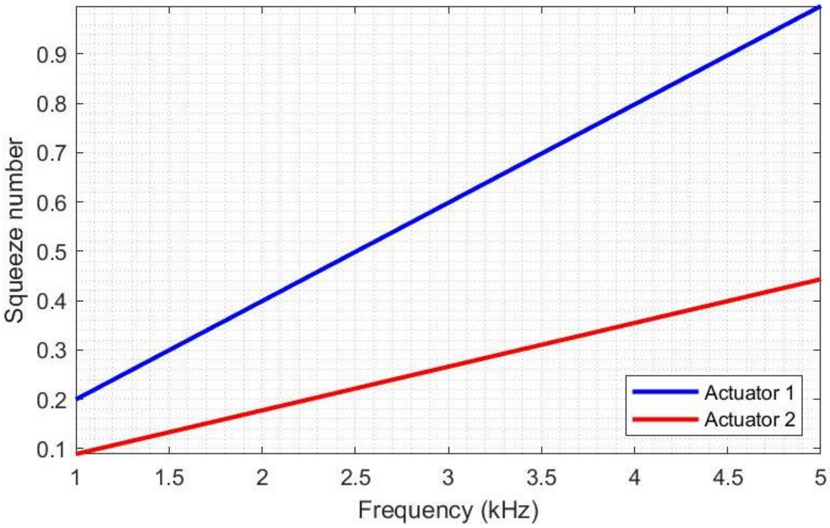

Figure 3.14. Calculated squeeze number for Actuator 1 and 2

The applicability of the theory presented above relies on several assumptions. First, the oscillation amplitude must be much smaller than the film thickness. This condition is satisfied since the displacement of the actuator is on the order of 10^{-2} μm, while the thickness of the film is four orders of magnitude larger. Additionally, the flow must be 2-dimensional (no pressure gradient across the film), laminar, fully developed, and isothermal [23]. These conditions can be verified by calculating three numbers [18]:

$$Re_C = \frac{\rho V H}{\mu}, \qquad Re_U = \frac{\rho \omega H^2}{\mu}, \qquad A = \frac{H}{L} \tag{3.8}$$

where ρ is the fluid density, and V is measured velocity. Re_C is the convective Reynolds number. It governs the strength of nonlinearities. Re_U is the unsteady Reynolds number. It determines the importance of inertial effects. A is the aspect ratio measuring the thinness of the film. For the theory to hold, all three numbers must be much smaller than unity.

The aspect ratio for actuators 1 and 2 are 0.3 and 0.4, respectively. These are certainly non-negligible, and one can expect that the theory should break down. However, numerical studies demonstrate that the squeeze force is in perfect agreement with the theory for the aspect ratios up to 0.2 [18]. For the larger aspect ratios, the squeeze force begins to deviate from prediction. When the aspect ratio is equal to one, the force predicted by the theory is about 3 times smaller than the simulated value. Since the spring force is negligible in the low frequency region (Figure 3.13), such deviation cannot explain the observed stiffness effect.

Figure 3.15 and Figure 3.16 show calculated convective and unsteady Reynolds numbers for actuators 1 and 2 in the low frequency region. The magnitude of the convective Reynolds number is on the order of 10^{-4}. Such a small value certainly satisfies the requirement for the squeeze film theory to be valid. The unsteady Reynolds number, on the other hand, is much larger than one, indicating that the inertial effects cannot be ignored. However, the modified squeeze film theory that incudes inertial effect cannot explain the observed increase in stiffness either. The mechanism for the spring force remains the same. In the low frequency region, and with the film thickness as large as it is in experiment, the fluid has enough time to escape. Moreover, the dense fluid such as oil is less compressible than gas. Squeeze film theories that include inertial effect do not even consider spring force [24-26]. In addition, the comparison of the theories with and without inertial effects demonstrate that the FRF in the low frequency region is the same [27]. The spring force does not exist in this region.

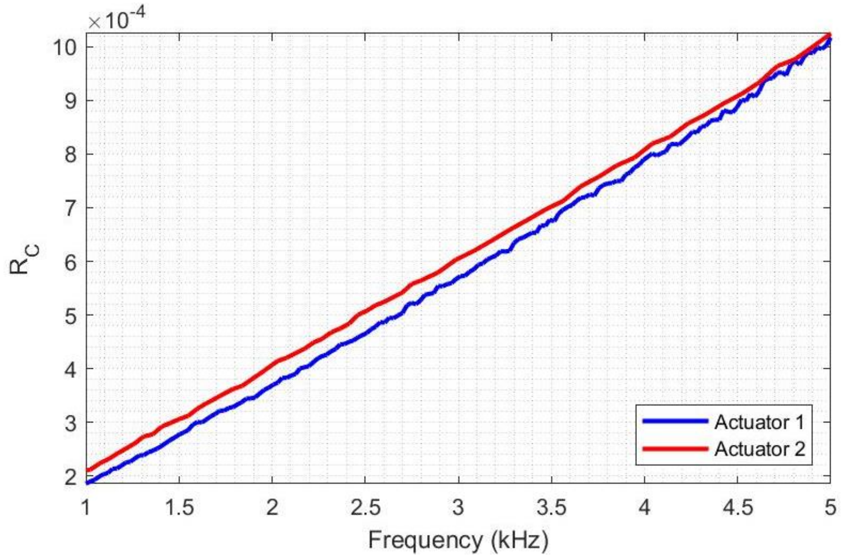

Figure 3.15. Calculated convective Reynolds number for Actuator 1 and 2

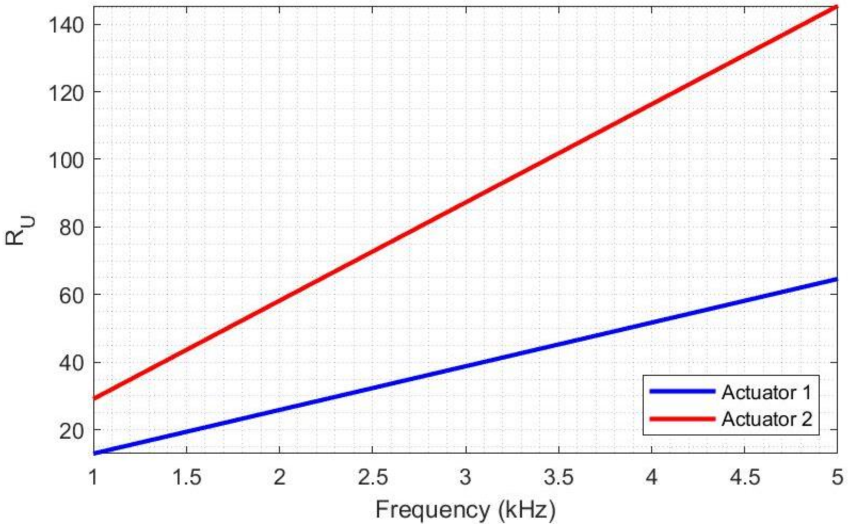

Figure 3.16. Calculated unsteady Reynolds number for Actuator 1 and 2

In conclusion, neither the squeeze film theory for compressible fluid, nor the modified theory that includes inertial effect can explain the reduction in static gain in the low frequency region. Therefore, the observed stiffness effect is attributed to the experimental inaccuracy.

Chapter 4. SIMULATION

Experimental result presented in Chapter 3 display two interesting phenomena. When the actuator is moved inside the fluid channels, the stiffness and the inertia effects have increased. The increase in stiffness was attributed to the experimental inaccuracy. The cause of the inertia effect has not been addressed yet. One possible reason for the increase in inertia is the coupling of the aluminum membrane and the actuator via the fluid film therebetween. Such coupling has been seen to reduce natural frequencies of two disks separated by a thin layer of air [28]. The reduction of natural frequencies via coupling has also been predicted theoretically and using finite element modeling for two disks separated by a water like fluid [29]. However, it is not clear how strong the coupling between the membrane and the actuator is. The amplitude of the membrane vibrations is very small (fraction of the nanometer). It is reasonable to assume that in this case the membrane behaves as a rigid wall. The frequency reduction of the structure vibrating near the rigid surface has been observed and predicted as well [14, 24, 25, 30].

To study the interaction between the actuator, fluid, and the aluminum membrane, finite element method can be employed. There are two ways that researchers commonly use to model fluid-structure interaction problems. The first approach is to model the structure and the fluid separately. The solution in structural domain is used to update the state of the fluid domain. Once the fluid domain model is solved, its solution is used to update the model in the structural domain. The process is repeated at every time step. This approach is proven to work, but it is also computationally expensive. At every time step, both, the Navier-Stokes and the structural equations are solved, and the information is exchanged. Even a relatively small problem requires enormous computational resources.

Another approach is to model fluid as an acoustic medium. There are several assumptions that must be satisfied for the approach to work. In particular, the fluid must be compressible, there should be no mean flow in the fluid, the pressure disturbance must be small [31]. With this approach, the entire model can be discretized and solved all at once using commercial package such as Ansys Acoustics. It has been demonstrated in [14] that the reduction of natural frequency via added mass effect can be predicted accurately using this method. In particular, the method was used to predict the drop in natural frequency when the microactuator is moved from air into the petri dish filled with oil. It has also been shown that structural-acoustical models are capable of predicting natural frequencies of submerged structures with nearby rigid wall [32]. Thus, if the vibration of the membrane can be neglected, the same approach can be used to predict frequency reduction of the actuator in the channel. For the case when the structural coupling is important, the capabilities of vibro-acoustic analysis are unknown. However, given resources at hand, a finite element model is developed in Ansys Acoustics to study the behavior of the actuator in the infinite fluid domain, and its interaction with the aluminum membrane inside the fluid channel.

Finite element method can be a very useful tool for the researcher; it can also be very misleading. The quality of the results obtained from the model is directly affected by the assumptions and the parameters used to build the model. The experimental setup described in Chapter 2 involves many unknown parameters. Some of them can be estimated with reasonable accuracy, others cannot be. For example, the mass of the membrane can be estimated quite well by measuring its geometric parameters and using the density of the aluminum from the engineering table. The stiffness of the membrane can be estimated using the Young’s modulus found in the same table, provided, that no stress was induced in the membrane during the assembly process. For the actuator, however, this task is not so easy.

First, the actuator’s plate is very thin (several μm) and has a complicated structure. There are multiple layers of different materials stacked on top of each other (e.g., top electrode, PZT, bottom electrode, bonding material, and base material). If each layer is modeled and meshed with few elements across its thickness, the mesh would be very fine to maintain a proper aspect ratio resulting in numerically expensive solutions. Such a fine mesh would certainly predict actuator performance well but might not necessarily enhance the understanding of the interaction among the actuator, the membrane, and the fluid. To address this challenge, the plate can be modeled as a single sheet made from the homogeneous material. This strategy had been successfully demonstrated in [14]. Piezoelectric properties can be ignored in this model, but density and stiffness are still required. No table can provide values for these parameters.

In addition, the dimensions given in Figure 2.3 are ideal. In reality, there are silicon residues left over from microfabrication at the junction of the actuator’s plate and beam. These residues affect the thickness and the effective area of the actuator’s plate. Moreover, the thickness of each layer of material within the actuator’s plate and the exact dimensions of silicon residues can only be found by destructively dissecting the actuator to examine the cross sections. This is not an option in this study. Thus, there are many uncertainties involved in the model. How these uncertainties affect the results is unknown.

To address this challenge the numerical study begins with a simpler, single degree of freedom model that serves several purposes. First, the model is used to understand how the unknown actuator’s parameters affect numerical results. Second, the model is used to determine the required geometric complexity. In particular, the effect of modeling silicon residues and the portion of the beam around actuator’s plate on numerical results is investigated. Third, the model is used to predict actuator’s resonance frequencies in air and in petri dish filled with oil. Finally, the model is used to understand the interaction of the actuator with the rigid wall. If the agreement with experimental results is achieved, then the motion of the membrane plays no role in the observed inertial effect. In this case, the more complex model that includes aluminum membrane is not required.

4.1 SINGLE DEGREE OF FREEDOM MODEL

Figure 4.1 shows the geometry of the simplest single degree of freedom models used in the study. Its primary purpose is to investigate how the actuator's unknown parameters affect the results of the simulation.

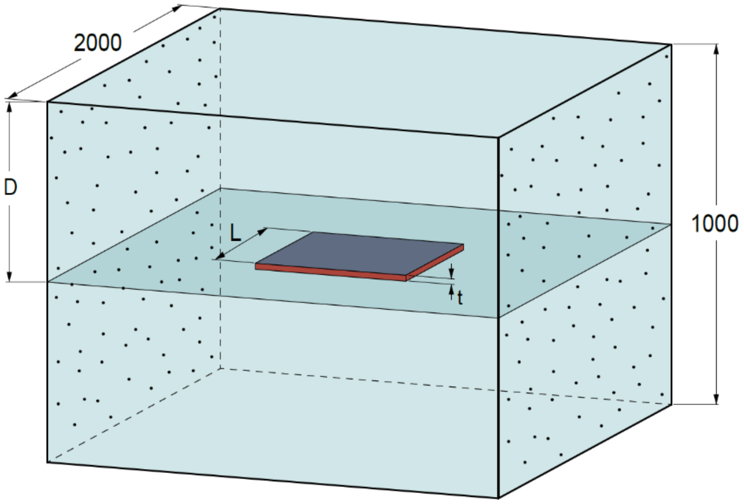

Figure 4.1. Simplest single degree of freedom model (dimensions in μm)

According to [14], the pressure disturbance produced by the actuator in the fluid is confined to the small space around it. The membrane does not cause any pressure disturbance because it is assumed to be stationary in the single degree of freedom model. As a result, only a portion of the single fluid channel in the area around actuator needs to be considered. For simplicity, the geometry of the channel is reduced to a square rectangle with a side length of 2000 μm. The height of the channel is 1000 μm matching its height in the experimental setup. The aluminum membrane as well as walls of the channel are modeled using “hard wall” boundary condition implying zero fluid velocity. This condition does not need to be specified in the modal analysis as it is a default boundary condition in Ansys Acoustics. The deviatory pressure on the remaining two faces of the fluid, where the channel was truncated (shown with dots), is set to zero. It should be noted, that since the pressure disturbance is localized to the space around actuator, zero pressure boundary condition can be omitted (implying zero fluid velocity) without affecting numerical results. There are two material properties needed to be specified for the fluid domain: density and speed of sound. They are set to 850 kg/m^3 and 1500 m/s, respectively. The viscosity of the fluid is omitted.

In this simplest case, the actuator is modeled as a square plate with an adjustable size. The plate is fixed inside the fluid at distance (D) from the wall by setting the displacement at its four side faces (shown in red) to zero. The “fluid structure interaction boundary conditions” are imposed on all its surfaces meaning that the acoustic pressure exerts a force to the structure, and the structural acceleration produced a fluid inertial load at the mesh interface. Since the material properties of the actuator are unknown, the estimate of density of 7624 kg/m^3 given in [14] can be used as a starting point (the value was adjusted to exclude perylene layer). The Youngs modulus and the size of the plate affect its bending stiffness, and as a result, its natural frequencies. If the size of the plate is set to the values given in Figure 2.3, the Youngs modulus required to match natural frequencies of the actuator in air and in petri dish filled with oil is unrealistically high (over 1000 GPa). The Youngs modulus of the materials comprising the actuator’s plate ranges from 79 GPa for gold to about 200 GPa for silicon. Given high natural frequencies of the actuators in air, the amount of silicon residues must be significant. Thus, the Youngs modulus of the plate is set to 175 GPa to be on the high side of the given range. For now, the side length of the plate (L) is kept as designed at 800 μm, while its thickness (t) is increased to 4 μm to bring the natural frequency into the range observed in experiment. Such adjustment is not unreasonable as silicon residues affect the effective size of the plate.

To model the behavior of the actuator inside the petri dish filled with oil as well as in air, the geometry of the model needs to be modified. In particular, the overall heigh of the fluid domain is increased to 2000 μm. The actuator is positioned in the middle, such that the heigh of the fluid column below and above the actuator is about 1000 μm. These conditions are sufficient to model the actuator in the infinite fluid domain as shown in [14]. The density and speed of sound in air are set to 1.225 kg/m^3 and 346 m/s, respectively.

The model is meshed using 20-noded brick elements with quadratic shape functions (FLUID 220 for fluid domain; SOLID 186 for the structural domain). When the quadratic elements are used, the fluid domain must be discretized such that there are at least six elements per wavelength of interest [31]. The wavelength can be calculated using the following equation:

$$\lambda = \frac{c}{f} \tag{4.1}$$

where c is the speed of sound in the medium; f is the frequency of excitation in Hz. The range of frequencies used in experiment is between 1 and 100 kHz. Thus, the shortest wavelength used in the experiment corresponds to the measurement in air at 100 kHz. The maximum element size for such simulation is about 500 μm.

To compare results between different simulations, as well as between different models, it is important to have a consistent mesh. The easiest way to accomplish this task is to generate a layer of nicely arranged elements that can be swept through the entire model. Given the size of the actuator, the maximum element size required by the fluid domain must be reduced to capture the behavior of the actuator correctly. The blue line in Figure 4.2 shows how the first natural frequency of the actuator is changing as the total number of elements in the model is increased; the red line shows corresponding element size. This particular study was conducted in oil with the actuator positioned in the middle of the channel, but similar results are obtained when the actuator is brought closer to the wall or moved into the infinite fluid domain.

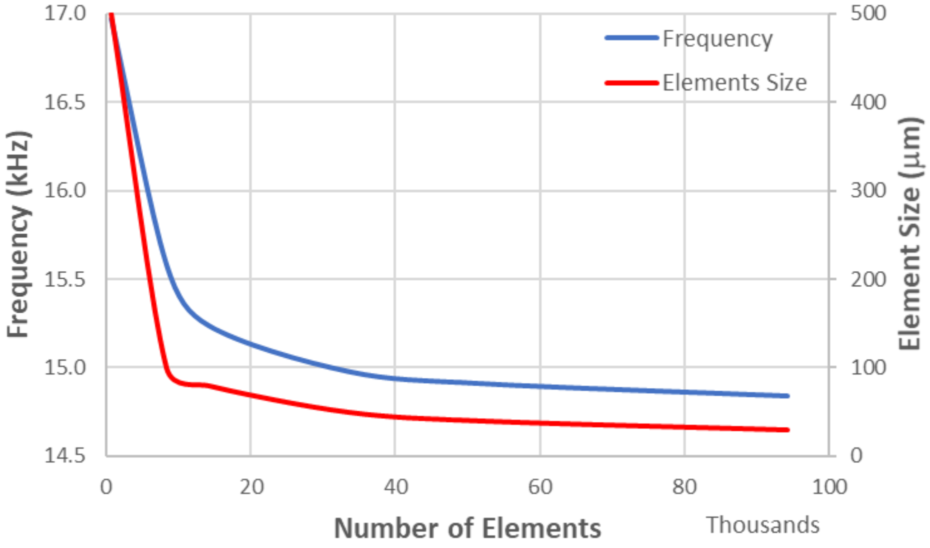

Figure 4.2. Actuator’s first natural frequency and element size versus total number of elements in the model

It is clear from the figure, as the number of elements in the model is increased, the first natural frequency of the actuator converges to some value below 15 kHz. Such convergence is desired; if no convergence is achieved, the model cannot be trusted. It also indicates the size of the error for a given element. As the elements size is decreased, the error becomes smaller, but at the same time, the computational effort increases. For the single degree of freedom model, the computational effort is relatively small. Even when the element size is reduced to 30 μm, the number of elements in the model remains under 100 thousand. However, if the full model of experimental setup is necessary, such a small element size will require enormous computational power that may not be available. As a compromise, the element size of 80 μm is chosen for all numerical studies. The resulting error in natural frequency relative to the smallest element size considered here is 3.2 %.

Another concern that must be taken into account is the number of elements across the thickness of the actuator's plate. In simulations conducted to generate Figure 4.2, the actuator was meshed using a single layer of elements. Even though the use of quadratic elements prevents shear locking problem [33], the accuracy of such mesh needs to be evaluated. Figure 4.3 shows how the first natural frequency of the actuator changes as the number of layers across its thickness is increased. Once again, the results are converging. The relative error between simulations using a single layer of elements as oppose to 8 layers is less than 3 %. Such error is acceptable; therefore, the actuator will be meshed using a single layer of elements in all numerical studies.

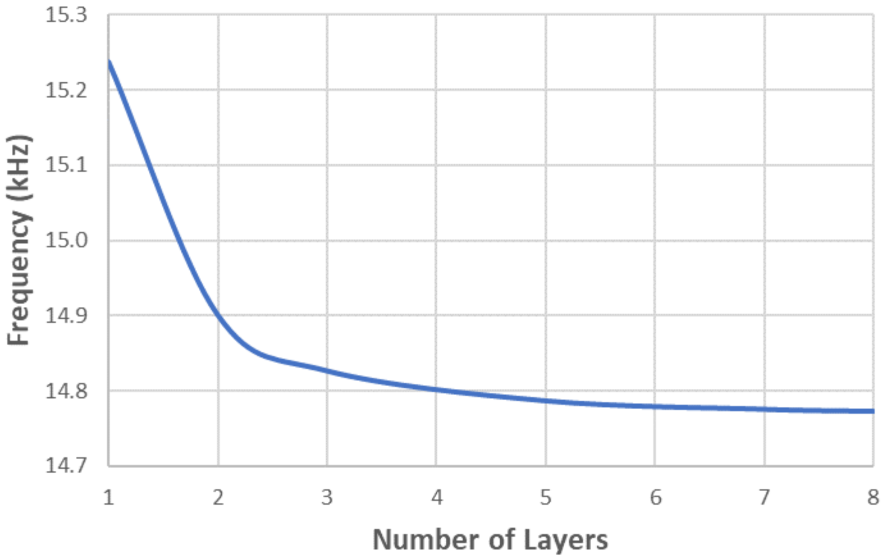

Figure 4.3. Actuator's first natural frequency versus the number of layers used to mesh it

The first step in the study is to evaluate the dependence of the simulated results on the parameters used in the model. In particular, the effect of uncertainty in actuator's Youngs modulus (E), density (ρ), and dimensions is investigated. The results of the study in air, petri dish filled with oil, and in the channel for several distances between the actuator and the wall are listed in Table 4.1. It is known that the natural frequency of the structure is inversely proportional to its mass. This fact is supported by simulations in air. When the density of the actuator is increased to

10000 kg/m^3, its first natural frequency drops from 53.7 to 47.0 kHz; when the density is decreased to 5000 kg/m^3, the natural frequency is raised to 66.1 kHz. However, for simulations in the petri dish or simulations in the channel, the change in density of the actuator has very little effect on its natural frequencies. This observation has a very simple explanation. When the actuator is moved from air into the petri dish filled with oil, its frequency dropped by 53.7/15.5 = 3.5 times. This means that the effective mass of the actuator has increased by $3.5^2 = 12$ times. Such a large increase indicates that the mass of the actuator itself is insignificant as compared with the mass of surrounding oil, and its changes are barely noticeable. Thus, the uncertainty in actuator's mass will not affect the results of numerical studies in oil.

Table 4.1. First natural frequency of the actuator predicted by the single degree of freedom model as Yong's modulus, density, and dimensions are varied

D (μm)	ω (kHz)								
50	10.5	9.7	11.2	10.6	10.4	3.8	19.0	23.7	15.4
75	11.9	11.0	12.7	12.0	11.8	4.3	21.5	26.4	17.2
100	12.8	11.8	13.7	12.9	12.7	4.6	23.0	28.0	18.4
200	14.4	13.4	15.4	14.6	14.3	5.3	26.0	30.6	20.5
300	15.0	13.9	16.0	15.2	14.8	5.5	26.9	31.3	21.1
400	15.2	14.1	16.2	15.4	15.0	5.5	27.3	31.5	21.3
500	15.2	14.1	16.3	15.4	15.1	5.6	27.3	31.6	21.4
Petri Dish	15.5	14.3	16.6	15.7	15.3	5.7	27.8	31.9	21.6
Air	53.7	49.7	57.4	66.1	47.0	26.9	80.6	86.6	70.6
	Nominal Model	E (GPa)		ρ (kg/m^3)		t (μm)		L (μm)	
		150	200	5000	10000	2	6	600	700

It is also obvious that when the Young's modulus or the thickness of the actuator is increased, or its side length is decreased, the actuator becomes stiffer. Consequently, its natural frequency should increase. When the actuator becomes more compliant (i.e. the Young's modulus or thickness is decreased, or side length is increased), its natural frequency should become lower. All the results listed in the table show such trend. Therefore, the reader may think that Youngs modulus and the geometry of the actuator affect its behavior in oil because the frequencies are changing. In this case explaining experimental observation using the simulation would be a very difficult task due to many uncertainties in the model. However, this is not the case. The drop in natural frequency when the actuator is placed in oil is due to the added mass of the fluid. Looking at the frequency itself might be misleading. A more useful way is to look at the added mass of the oil in all these simulations. One way to do it is to calculate an added mass coefficient defined as:

$$\omega_R = \frac{\omega}{\omega_{\propto,Oil}} \tag{4.2}$$

where ω is the first natural frequency extracted from the simulation in air or in the channel at particular distance from the wall; $\omega_{\propto,Oil}$ is the corresponding first natural frequency of the actuator in the petri dish filled with oil (infinite fluid domain). The results of this calculation are shown in Table 4.2.

Table 4.2. Added mass coefficient predicted by the single degree of freedom model as Yong's modulus, density, and dimensions of the actuator are varied

D (μm)	ωR								
50	0.68	0.68	0.68	0.67	0.68	0.67	0.68	0.75	0.71
75	0.77	0.77	0.77	0.76	0.77	0.76	0.77	0.83	0.80
100	0.82	0.82	0.82	0.82	0.83	0.82	0.83	0.88	0.85
200	0.93	0.93	0.93	0.93	0.93	0.93	0.93	0.96	0.95
300	0.97	0.97	0.97	0.97	0.97	0.97	0.97	0.98	0.98
400	0.98	0.98	0.98	0.98	0.98	0.98	0.98	0.99	0.99
500	0.98	0.98	0.98	0.98	0.98	0.98	0.98	0.99	0.99
Petri Dish	1.00	1.00	1.00	1.00	1.00	1.00	1.00	1.00	1.00
Air	3.47	3.47	3.47	4.20	3.07	4.76	2.90	2.72	3.26
	Nominal Model	E (GPa)		ρ (kg/m^3)		t (μm)		L (μm)	
		150	200	5000	10000	2	6	600	700

It becomes clear, that the uncertainty in Young's modulus, density, or the thickness of the actuator will not affect the quality of numerical results. The added mass coefficients, and consequently, the behavior of the actuator in oil, do not depend on these parameters (the added mass coefficients when actuator is moved from air into a petri dish vary with density and thickness because these parameters affect the mass of the actuator, and consequently its natural frequency in air). Once the frequency of the actuator in petri dish is set, its frequency in the channel depends only on the actuator's side length and the distance between the actuator and the membrane which, in this case, behaves as a wall. It can be noted, that for a given distance, the added mass coefficient is smaller for the actuator with a larger side length. Smaller coefficient means larger frequency drop and hence, larger added mass. Such observation makes perfect sense because added mass is proportional to fluid loading [34]. Larger actuator has to move more fluid. It is also apparent that for a given actuator, the added mass increases as the distance between the actuator and the membrane decreases. Such behavior can also be explained by referring to fluid loading. It depends not only on the actuator's area, but also on the pressure in the fluid surrounding it. Figure 4.4 shows pressure distribution in the cross section that passes through the middle of the channel as the distance between the actuator and membrane is varied (the actuator's side length used to generate the figure is 600 μm).

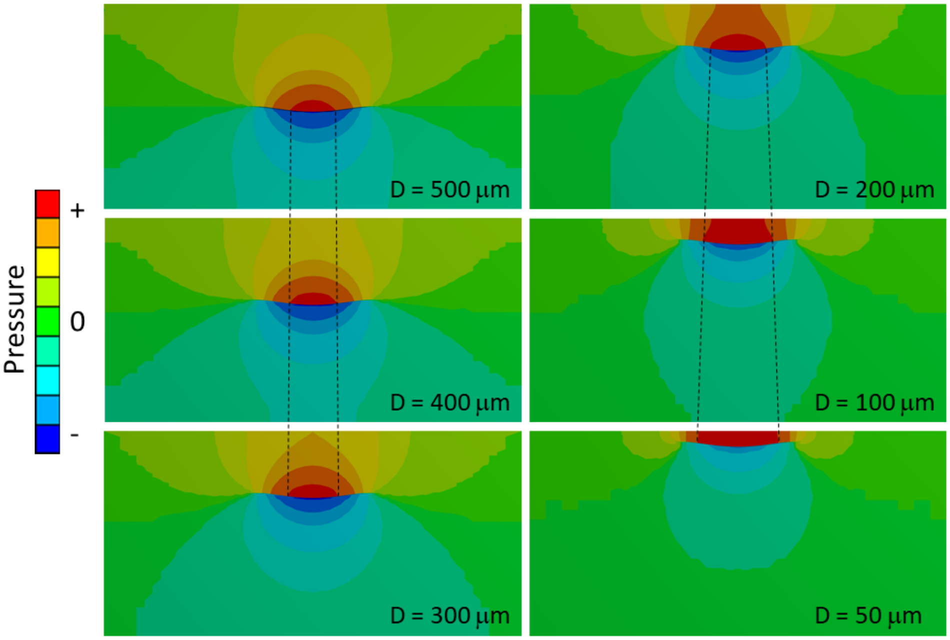

Figure 4.4. Pressure distribution around the actuator in the channel

As actuator is brought closer to the membrane, the area of high-pressure region (shown in red) expands to cover larger area of the actuator. Higher pressure over larger region results in larger fluid loading, and hence, larger added mass. It is also noticeable that when the distance between the actuator and membrane is relatively large (300 – 500 μm), the high-pressure region expands slowly. The changes in corresponding added mass coefficients are also small (0.98 – 0.99). When the distance is reduced to 200 μm and beyond, the high-pressure region expands more drastically. The corresponding added mass coefficients are also changing much faster (0.96 – 0.75). However, the added mass coefficient, even for the actuator with the larges side length, is much larger than in the experiment. For example, for actuator 1, which is located about 240 μm from the membrane, the added mass coefficient is 0.64. If the frequency of this actuator in petri dish is matched using the actuator with a side length of 800 μm (largest possible), the added mass coefficient extracted from the model is between 0.93 and 0.97. Thus, even when the side length of the actuator is maximized, the model significantly underestimates added mass in the channel for all actuators as evident from Table 4.3.

Table 4.3. Comparison of added mass coefficients obtained in the experiments with the minimum added mass coefficients predicted by a single degree of freedom model

D (μm)	ω_R	D (μm)	ω_R	D (μm)	ω_R	D (μm)	ω_R
50	0.68					60	0.39
75	0.77						
100	0.82						
200	0.93	240	0.64				
300	0.97			323	0.82		
400	0.98						
500	0.98						
L = 800 μm		Actuator 1		Actuator 2		Actuator 3	
Simulation		Experiment					

There can be a number of reasons for the discrepancy. After all, the actuator was modeled as a plate and the membrane was modeled as a wall. In the physical system, the membrane motion might be important. It is also possible that if the actuator is modeled using more realistic geometry that includes silicon residues and support structure, the added mass in the channel may increase. To narrow down the number of reasons, and to determine the required geometric complexity of the actuator in the model that includes the membrane, the effect of silicon residues on the added mass is investigated first.

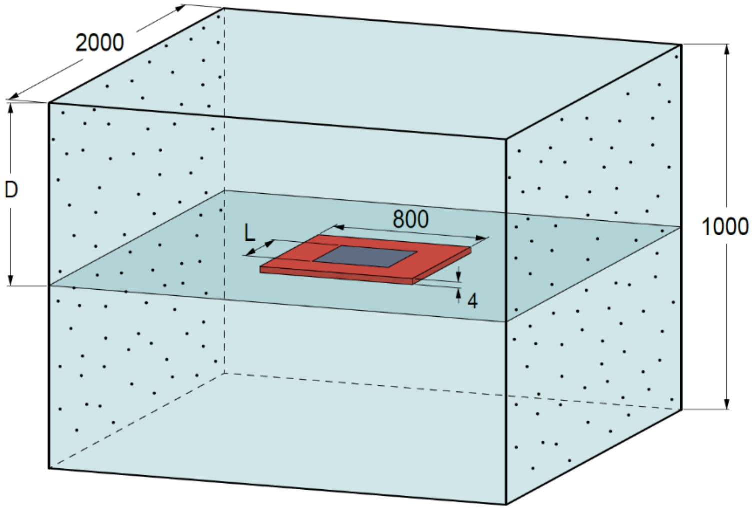

Figure 4.5. Single degree of freedom model with silicon residues (dimensions in μm)

Figure 4.5 shows the model that includes silicon residues. The only difference with the model described above lies in the geometry of the actuator. Here, the actuator's plate is divided in two regions. The outer portion (shown in red) has a side length of 800 um matching the physical size of the actuator's plate. The displacement of the outer portion is set to zero. With this setup, it is assumed that silicon residues make the outer portion of the actuator's plate very stiff and essentially motionless. The area that vibrates is represented in the model by the inner portion. Its size and the distance between the actuator and the membrane can be varied. To see the effect of silicon residues, the results of the simulation can be compared to the corresponding results obtained from the model shown in Figure 4.1. Table 4.4 presents a comparison.

Table 4.4. Comparison of the results predicted by the single degree of freedom model with and without silicon residues

D (μm)	ω (kHz)	ω_R	ω (kHz)	ω_R	ω (kHz)	ω_R	ω (kHz)	ω_R
50	23.7	0.75	15.4	0.71	21.0	0.69	14.4	0.68
75	26.4	0.83	17.2	0.80	23.7	0.78	16.3	0.77
100	28.0	0.88	18.4	0.85	25.5	0.84	17.5	0.83
200	30.6	0.96	20.5	0.95	28.6	0.94	19.7	0.94
300	31.3	0.98	21.1	0.98	29.5	0.97	20.4	0.97
400	31.5	0.99	21.3	0.99	29.8	0.98	20.7	0.98
500	31.6	0.99	21.4	0.99	29.9	0.99	20.8	0.99
Petri Dish	31.9	1.00	21.6	1.00	30.3	1.00	21.1	1.00
Air	86.6	2.72	70.6	3.26	86.6	2.86	70.6	3.35
L (μm)	600		700		600		700	
	Model without Silicon Residues				Model with Silicon Residues			

The results show that the addition of silicon residues reduces natural frequency of the actuator in the petri dish and in the channel, indicating an increase in added mass. The reason behind added mass increase can be explained by comparing pressure distribution around actuator between the two models. The comparison is presented in the Figure 4.6 for the actuator with the effective side length of 600 μm, placed in the channel 100 μm from the membrane.

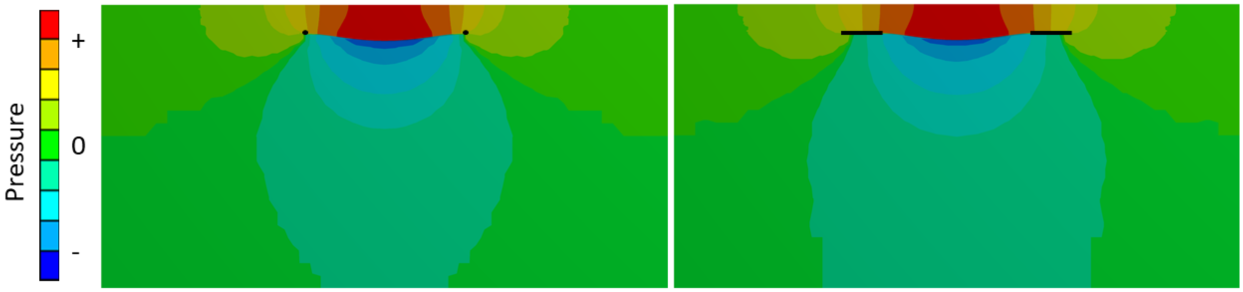

Figure 4.6. Pressure distribution around the actuator in the channel for the model with (right) and without (left) silicon residues

The pressure near the edge of the actuator modeled without residues changes gradually from positive on the top surface to negative on the bottom surface. If the residues are modeled, the gradual change in pressure occurs further from the effective area of the actuator. As a result, the region of high pressure on the top face, as well as the region of low pressure on the bottom face of the actuator are extended. Wider regions of high and low pressure increase fluid loading that leads to a larger added mass. The increase in added mass due to silicon residues is not large enough to bring experimental and simulated results in the agreement. However, the increase is significant enough for silicon residues to be included in the model of the actuator.

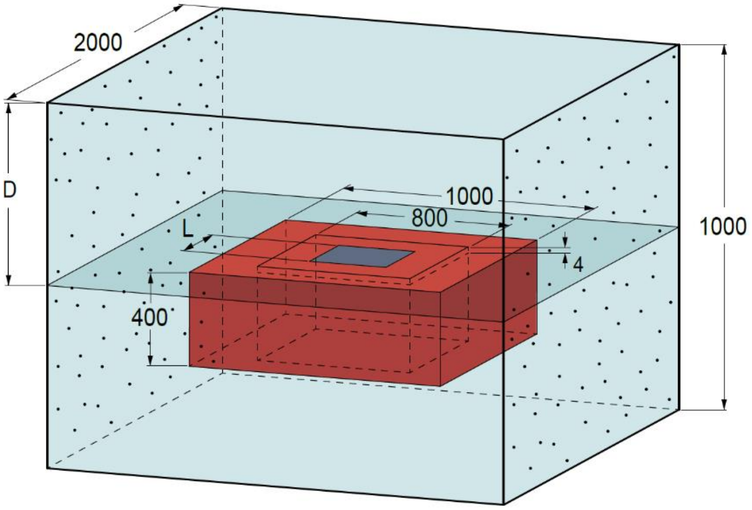

Figure 4.7. Single degree of freedom model with silicon residues and support structure (dimensions in μm)

To conclude the study of the single degree of freedom system, the effect of support structure on the actuator's behavior is investigated using the model shown in Figure 4.7. The only difference between this model and the one with silicon residues is the presence of support structure modeled as 100 μm thick walls surrounding actuator's plate. These walls represent the portion of the actuator's beam which is made from silicon (Figure 2.3). The Young's modulus and density of silicon used in all numerical studies are 202 GPa and 2330 kg/m^3, respectively. The height of the walls is 400 μm matching the height of the beam in the physical system. The rest of the actuator's beam is not expected to significantly affect the numerical results because the pressure disturbance is localized near the actuator's plate and decays rapidly; therefore, it will not be modeled. Since the deformation of the actuator's beam is much smaller than the deformation of the actuator's plate, the displacement of support structure is set to zero. In addition, the "fluid-structure interaction boundary conditions" are imposed on its surfaces. The area of the vibrating portion of the actuator and the distance between the actuator and the wall can be varied. The results of the simulation can be compared to the results obtained from the model shown in Figure 4.5. Table 4.5 presents the comparison.

Table 4.5. Comparison of the results predicted by the single degree of freedom model with and without support structure

D (μm)	ω (kHz)	ω_R	ω (kHz)	ω_R	ω (kHz)	ω_R	ω (kHz)	ω_R
50	21.0	0.69	14.4	0.68	18.2	0.69	12.1	0.68
75	23.7	0.78	16.3	0.77	20.4	0.77	13.6	0.76
100	25.5	0.84	17.5	0.83	21.8	0.82	14.6	0.82
200	28.6	0.94	19.7	0.94	24.4	0.92	16.3	0.92
300	29.5	0.97	20.4	0.97	25.2	0.95	16.8	0.95
400	29.8	0.98	20.7	0.98	25.1	0.95	16.8	0.94
500	29.9	0.99	20.8	0.99	24.2	0.91	16.1	0.90
Petri Dish	30.3	1.00	21.1	1.00	26.5	1.00	17.8	1.00
Air	86.6	2.86	70.6	3.35	84.7	3.20	70.2	3.94
L (μm)	600		700		600		700	
	Model without Support Structure				Model with Support Structure			

The results show that the addition of support structure reduces natural frequencies of the actuator in air, in the petri dish, and in the channel, indicating an additional increase in added mass. Unlike silicon residues, the support structure has a more pronounced effect on the added mass coefficient when the actuator is further from the membrane. For example, when the actuator with a side length of 600 μm is placed 100 μm from the membrane, the added mass coefficient drops from 0.84 to 0.82 when support structure is modeled. However, when the same actuator is placed 500 μm from the membrane, the added mass coefficient is reduced from 0.99 to 0.91. This behavior can be explained by comparing pressure distribution around actuator in the channel for the model that includes both silicon residues and support structure with the model that only has silicon residues. The comparison is presented in the Figure 4.8 for the actuators with the effective side length of 600 μm, placed in the channel 100 μm and 500 μm from the membrane

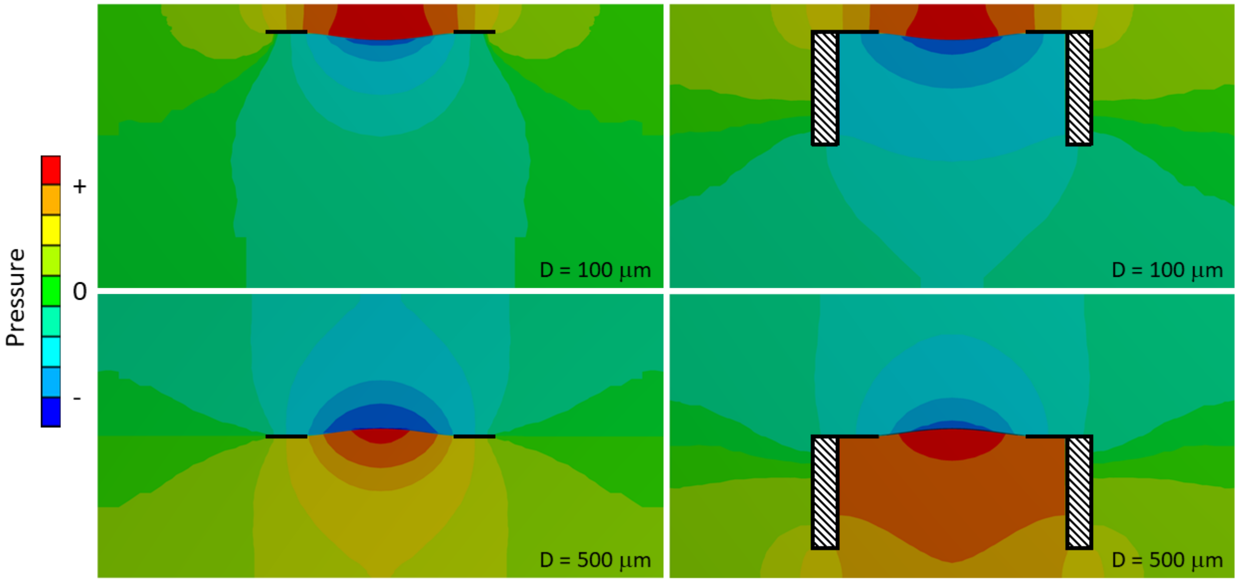

Figure 4.8. Pressure distribution around the actuator in the channel for the model with (right) and without (left) support structure

The presence of sidewalls drastically alters the pressure distribution in the channel. Just like silicon residues, they act as a barrier between pressure fields above and below actuator's plate. For example, when the distance between the actuator and membrane is 100 μm, the positive pressure field above the actuator extends further downward because the walls confine the negative pressure field within. However, the walls are located far from the area of the actuator that vibrates. As a result, the changes that the vibrating area experiences are minor and the change in added mass is small. When the actuator is moved further from the membrane, the gap between the support structure and the wall opposite to the membrane decreases. In a sense, the wall acts as a cap confining the fluid withing the support structure. The pressure in the confined fluid increases significantly during the motion of the actuator, which leads to a large increase in added mass. Therefore, the support structure cannot be neglected in the model.

This latest single degree of freedom model that includes silicon residues and support structure can be used to match natural frequencies of actuators in the experiment. First, the effective side length of the actuator is reduced to match natural frequency of each actuator in the petri dish. Material properties and geometric parameters used in the model are summarized in Table 4.6. Next, the simulation is conducted in air to determine the accuracy of the model. For actuator 1, the resulting error is under 5 %. For actuator 2 and 3 natural frequencies in air are not available because they exceed the measurement range of the equipment (100 kHz). The simulated results for these actuators are also quite high. The results in air and petri dish are compared in Table 4.7.

Table 4.6. Material properties and geometric parameters used in the model

	Actuator's Plate			Silicon Residues	Support Structure	Air	Oil
	A1	A2	A3				
Speed of Sound (m/s)	-					346.3	1500
Young's Modulus (GPa)	175			202		-	
Density (kg/m^3)	7624			2330		1.2	850
Poisson Ratio	0.33					-	
Thickness (μm)	4			4	400	-	
Side Length (μm)	650	590	570	800	1000	-	

Table 4.7. Comparison of experimental and simulated results in air and in petri dish

		Actuator 1	Actuator 2	Actuator 3
Frequency in Petri Dish (kHz)	Experiment	21.6	27.3	30.3
	Simulation	21.4	27.6	30.1
	Error (%)	0.8	1.2	0.7
Frequency in Air (kHz)	Experiment	77.5	> 100	> 100
	Simulation	81.1	98.6	102.7
	Error (%)	4.6	-	-

Finally, the simulation in the channel is performed and the results are compared in the Figure 4.9. Here, the simulated first natural frequency of each actuator is plotted in color as a function of the distance between the actuator and membrane. The experimental measurements are shown in black (as a reminder, the distance between the actuator and membrane was measured twice for actuators 1 and 2, and only once for actuator 3). It is clear, the model significantly underpredicts added mass for all actuators. The relative errors are 18, 42, and 75% for actuators 1, 2, and 3, respectively. Since it has been shown in [32] that vibro-acoustic analysis is capable of predicting natural frequencies of the submerged structure vibrating near rigid surfaces, there can be only one explanation for the discrepancy. The membrane vibrations play significant role in the system, even though they are very small. The observed inertial effect must be caused by the coupling of the actuator and membrane via fluid in between.

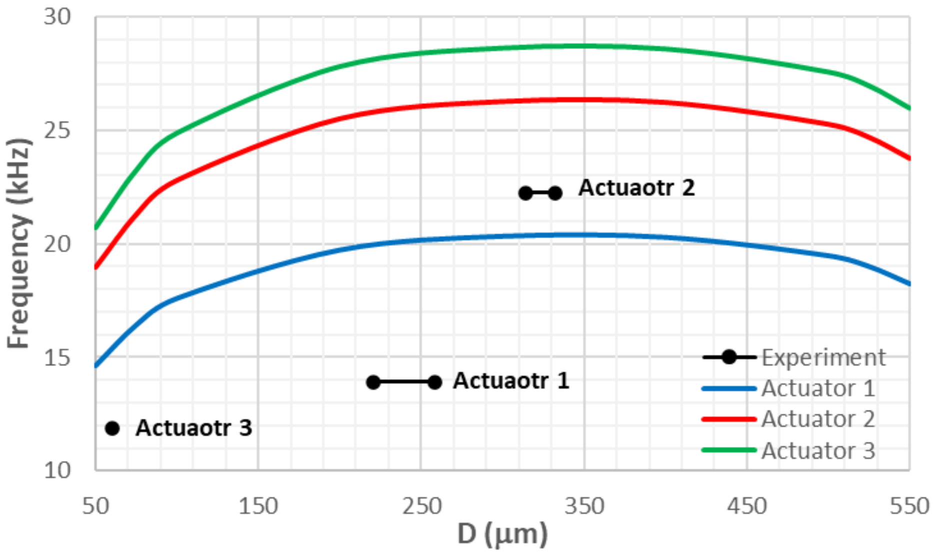

Figure 4.9. Comparison of experimental and simulated results in the channel

4.2 TWO-DEGREES OF FREEDOM MODEL

Since the behavior of the actuator predicted by the single degree of freedom model does not match experimental observations, the membrane must be included in the model. Unlike the motion of the actuator, the vibration of the membrane will affect the pressure distribution throughout the entire fluid domain. As a result, the model that includes full geometry of experimental setup might be necessary to study the interaction between the actuator and membrane. However, as an incremental step, a simpler, two-degrees of freedom model shown in Figure 4.10 is proposed first.

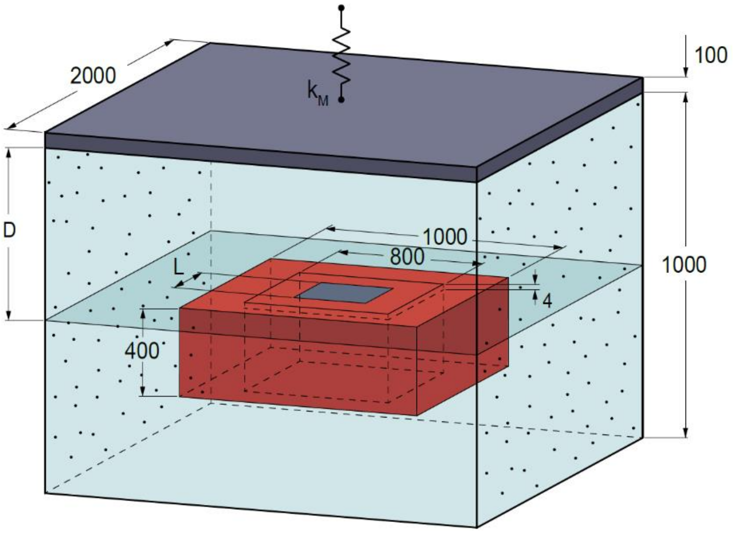

Figure 4.10. Two-degrees of freedom model with dimensions (μm)

Here, a stiff membrane, a spring, and a “fluid-structure interaction boundary condition” at the interface of the membrane and the fluid are added to a single degree of freedom model described in the previous section (model parameters are listed in Table 4.6). The density of the membrane is set to 2770 kg/m^3 – the density of aluminum found in Ansys database. Its thickness is set to 100 μm to match the thickness of the aluminum membrane used in the experiment. It is meshed with two layers of SOLID 186 elements resulting in the model with roughly 19300 elements and 84000 nodes. The longitudinal spring is attached to the entire top face of the membrane using body-ground connection and aligned along the height of the channel. Since the software does not allow non-deformable bodies to be included in the vibroacoustic analysis, the following work-around is employed. First, the Young’s modulus of the membrane is set to unrealistically high value (e.g. 10^6 GPa). Second, the motion of the membrane is restricted to a single dimension along the height of the channel. With this setup, the modes associated with elastic deformation of the membrane are shifted in the high frequency range. The frequency of the mode associated with the rigid-like motion of the membrane can be easily controlled by adjusting spring stiffness k_M. By limiting frequency range for the analysis, the study can be focused on the interaction of the actuator and membrane that appears in the two vibrations modes. One mode is associated with the first vibration mode of the actuator; another one is due to the rigid-like motion of the membrane. The goal of the study is to understand how the frequencies of these two modes are changing as parameters of the system are varied.

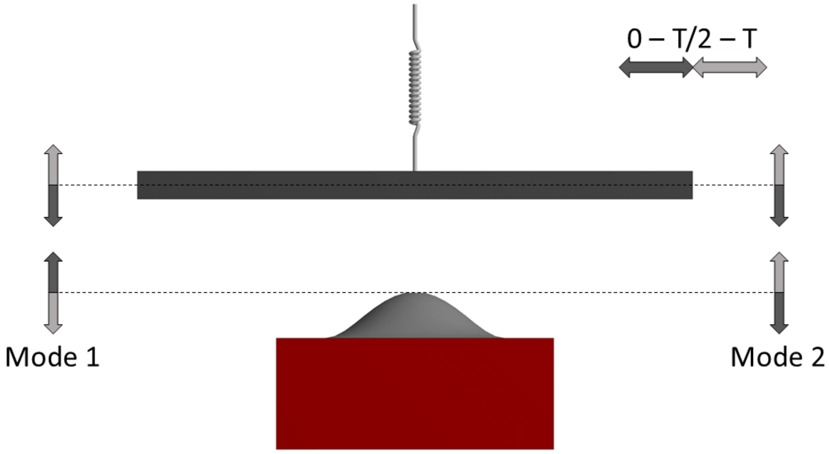

Figure 4.11. Vibration mode shapes predicted by the two-degrees of freedom model

Figure 4.11 shows the vibration mode shapes for both modes under study. Mode 1 is a lower frequency mode. In this mode, the motion of the actuator and the membrane is always out of phase. Mode 2 is the higher frequency mode. In this mode, the actuator and membrane always move in phase. Another difference between the two modes is a relative deformation of the actuator and the membrane. It varies as the system parameters are changed.

To gain confidence in the results of the two-degrees model, it is important to establish a connection with the single degree of freedom model. Afterall, rigid bodies are not supported in the vibroacoustic analysis, and work-around may compromise the results. The connection is established by considering a limiting case when the membrane behaves as a wall. When such behavior is achieved, the results of the two-degrees of freedom model should converge to the results of the single-degree of freedom model. One way to achieve wall-like behavior from the membrane is to make the spring very stiff (e.g. 10^6 N/m). The results of this simulation for different values of film thickness are compared to the results of the single degree of freedom model in the Figure 4.12. Here the resonance frequency of mode 1 is identical to the resonance frequencies of the actuator predicted by the single degree of freedom model. Therefore, mode 1 in this case, is the mode associated with the motion of the actuator; mode 2, is the mode associated with the motion of the membrane. The membrane behaves as a wall because the force required to move it is enormous.

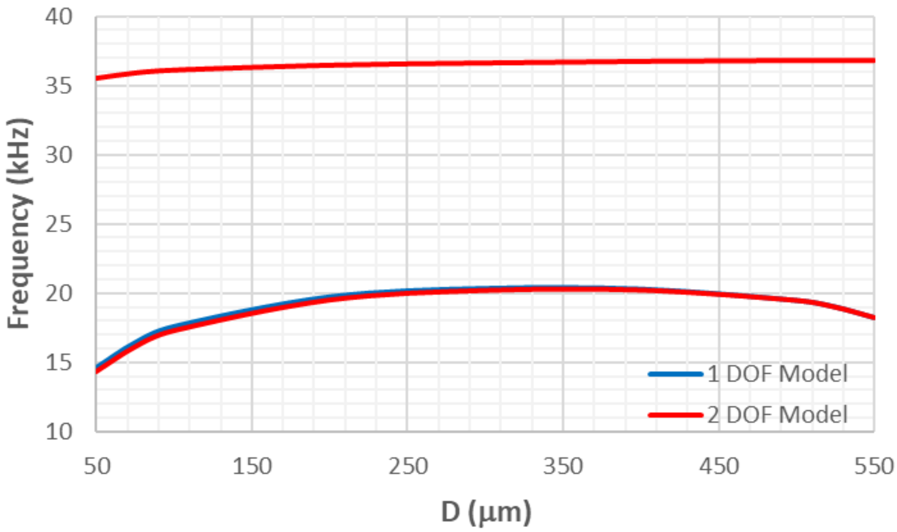

Figure 4.12. Comparison of the results predicted by the single and two-degrees of freedom models

Another way to think about limiting case is to think about relative frequencies of the two modes. When the membrane is very stiff, the resonance frequency associated with its motion is much higher than the resonance frequency associated with the motion of the actuator. Since the frequencies of two modes are far apart, the actuator vibrating at its resonance frequency does not excite the membrane. The pressure distribution near the actuator, and so is the force on the actuator, are unaffected by the presence of the membrane that is essentially motionless. As a result, the resonance frequency of the actuator is identical to the frequency predicted by the single degree of freedom model. When the difference between the resonance frequencies of two modes is reduced, actuator begins to “feel” the membrane. Figure 4.13 shows how the resonance frequencies of both modes are changing as the stiffness of the membrane is varied for two values of film thickness. The dashed line represents the frequency of the actuator predicted by the single degree of freedom model. Figure 4.14 shows how the ratio of the maximum vibration amplitude of the actuator over membrane changes for the same simulation. The solid line is the ratio for mode 1; the dashed line is the ratio for mode 2.

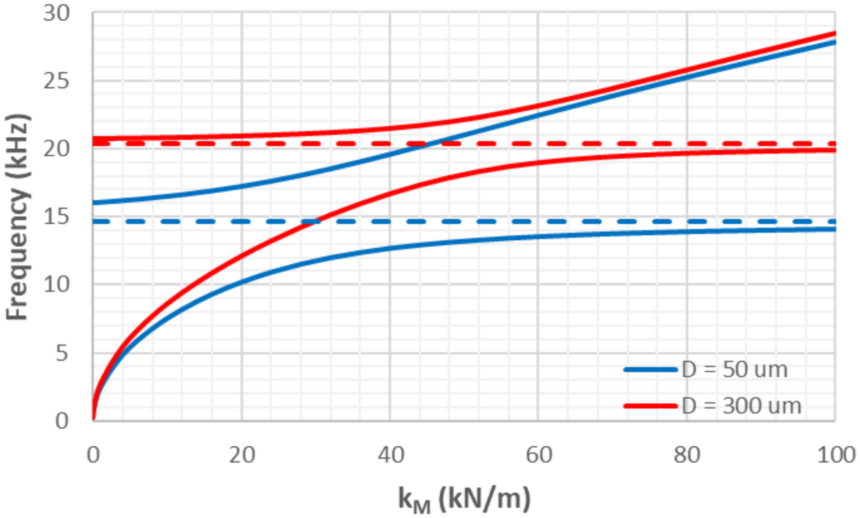

Figure 4.13. Resonance frequencies predicted by the two-degrees of freedom model (solid line) and by the single degree of freedom model (dashed line)

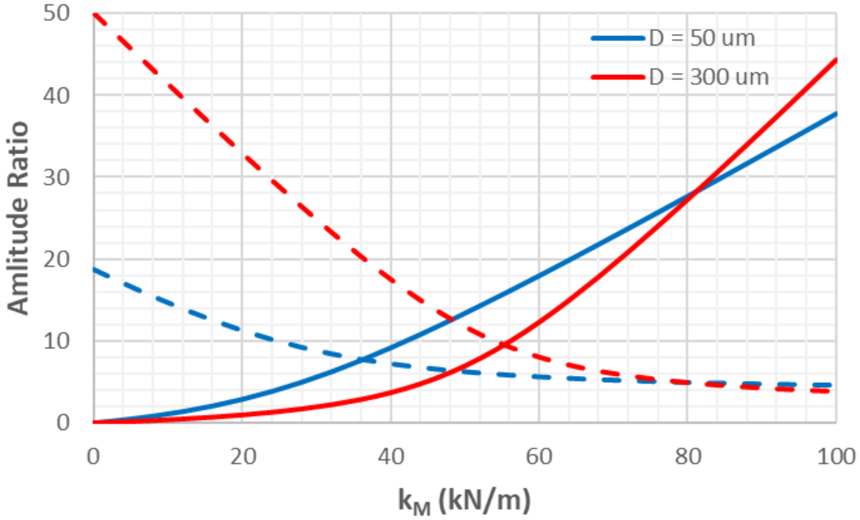

Figure 4.14. Amplitude ratios (actuator/membrane) predicted by the two-degrees of freedom model for mode 1 (solid line) and mode 2 (dashed line)

When the spring stiffness is very low (e.g. under 10 kN/m), the frequency of mode 2 approaches the frequency of the actuator predicted by the single degree of freedom model. The frequency of mode 1 is much lower. Because of the large difference in frequencies of two modes, when mode 2 is excited, the vibration amplitude of the actuator is 20 to 50 times larger than the vibration amplitude of the membrane. For the actuator, the membrane behaves like a wall in this case, and single degree of freedom model is sufficient for predicting resonance frequency of the actuator. When the spring stiffness is very high (e.g. above 90 kN/m) we get a limiting case described above. Here, mode 2 is the mode associated with the motion of the actuator. The vibration amplitude of the actuator in this mode is about 40 times larger than the amplitude of the membrane. Again, single degree of freedom model is sufficient here. In both of these cases, when the frequency of one of the modes is approaching the frequency of the actuator predicted by the single degree of freedom model, the coupling between the actuator and membrane can be defined as “weak”. When one component is excited, the other component is essentially motionless as evident from the Figure 4.14. The two-degrees of freedom model is redundant here because each component can be modeled independently.

The case of “strong” coupling occurs when the spring stiffness is chosen such that the resonance frequencies of two modes are closer to each other. Under this condition, frequencies of both modes deviate from the frequency predicted by the single degree of freedom model. It is no longer possible to say which mode is associated with the motion of the actuator, and which mode is associated with the motion of the membrane. The ratios of amplitudes between the actuator and membrane are similar for both modes. Therefore, when the actuator is excited at the frequency of either mode, the membrane responds with a relatively large amplitude. The membrane motion affects the pressure distribution near the actuator, which affect the force acting on the actuator. As a result, the resonance frequencies of both modes are different than the resonant frequency of the actuator predicted by the single degree of freedom model.

It can also be noted that the strength of the coupling depends on the distance between the actuator and membrane. For example, in the region of low spring stiffness (under 10 kN/m), the amplitude ratio for the actuator located 300 μm from the membrane is about 50, while the same ratio is about 20 for the actuator located 50 μm from the membrane (refer to Figure 4.14). The membrane response is much larger when the film thickness is smaller. This makes an intuitive sense. Actuator and membrane “feel” each other better when they are closer. Larger membrane response results in a larger change in the pressure distribution. As a result, for the given membrane, the difference between frequencies predicted by a single and a two-degrees of freedom model is larger for the actuator that is closer to the membrane (refer to Figure 4.13).

In any case, the two-degrees of freedom model predicts two modes. The frequency of mode 1 is lower than the frequency predicted by the single degree of freedom model, while the frequency of mode 2 is higher. Since the frequency of the actuator observed in the experiment is lower than the frequency predicted by the single degree of freedom model, the frequency of mode 1 can be matched to the frequency of the actuator measured in the experiment by adjusting the spring constant k_M. With this model, the experimental results can be explained fairly well. Thus, the required values of the spring stiffness are 28, 72, and 24 kN/m for actuators 1, 2, and 3, respectively. The difference between spring constants for actuator 1 and 3 is relatively small and can be easily justified. Even though the membrane in experiment is the same, the stress induced in it during the assembly can alter its stiffness. The large value for the case of actuator 2 will be addressed later. The results of the simulation for the three actuators are shown in Figure 4.15 and Figure 4.16.

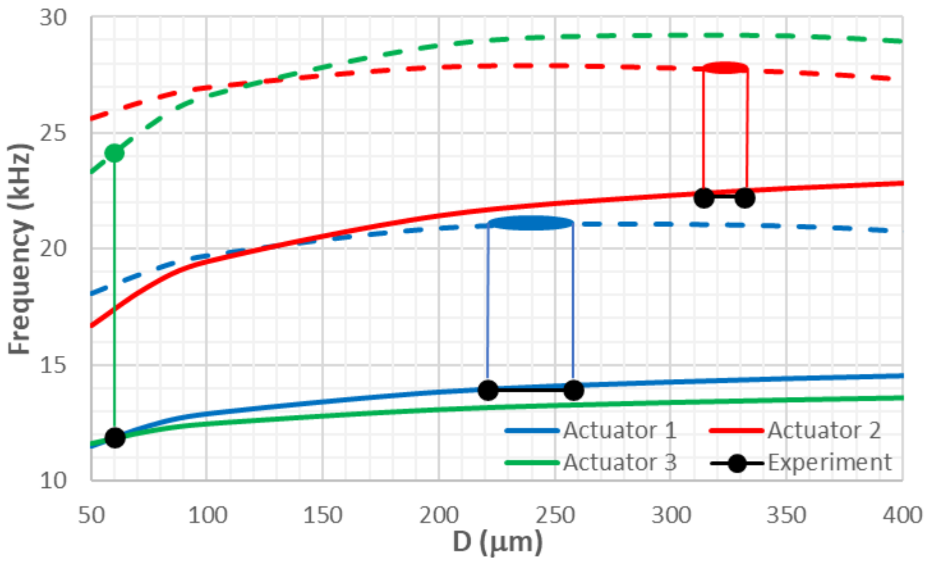

Figure 4.15. Resonance frequencies predicted by the two-degrees of freedom model for actuators 1, 2, and 3 (mode 1 – solid line; mode 2 – dashed line)

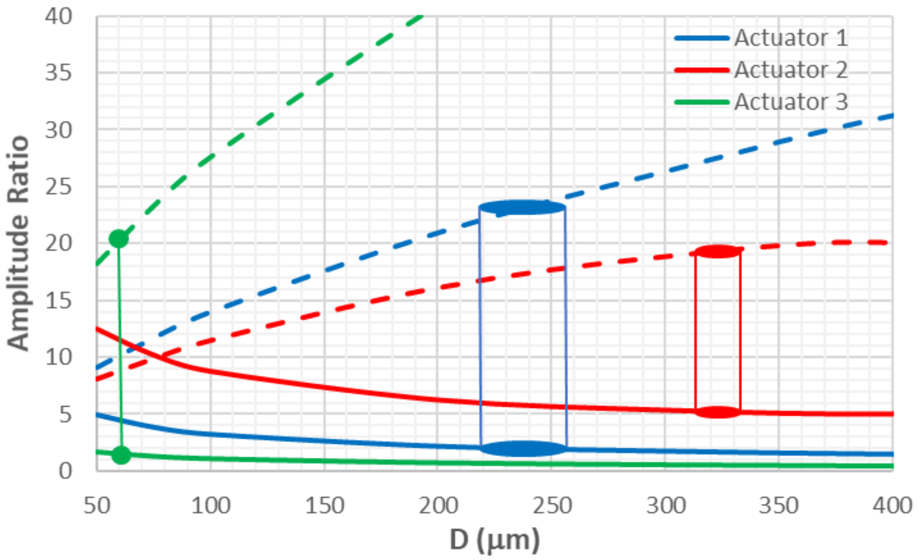

Figure 4.16. Amplitude ratios (actuator/membrane) predicted by the two-degrees of freedom model for actuators 1, 2, and 3 (mode 1 – solid line; mode 2 – dashed line)

Since the lower frequency mode is accompanied by the mode of higher frequency, the experimental results should contain additional peak at higher frequency. According to the model, these peaks are located around 21, 28, and 24 kHz for actuator 1, 2, and 3, respectively. In the lower frequency mode actuator and membrane should be moving out of phase; at the higher frequency, they should be in phase. The amplitude ratio between the actuator and membrane should be much lower in the out of phase mode as compared to the in-phase mode for all actuators.

Figure 4.17 shows several FRF measurements in the channel for the case of Actuator 1. The black line is the measurement from the actuator; color lines are the measurements from the points on the membrane located above the actuator's plate. Mode 1 corresponds do the dominant peak that occurs around 14 kHz. At this frequency, points 5 and 6 are in phase with the actuator; point 4 is lagging by about 60 degrees. The amplitude difference between the actuator and membrane is about 20 dB, which corresponds to the amplitude ratio of about 10. The peak corresponding to mode 2 is barely noticeable. It occurs around 19 kHz. At this frequency, the phase difference between the actuator and membrane is about 120 degrees. The amplitude difference is about 10 dB, which corresponds to the amplitude ratio of about 3.

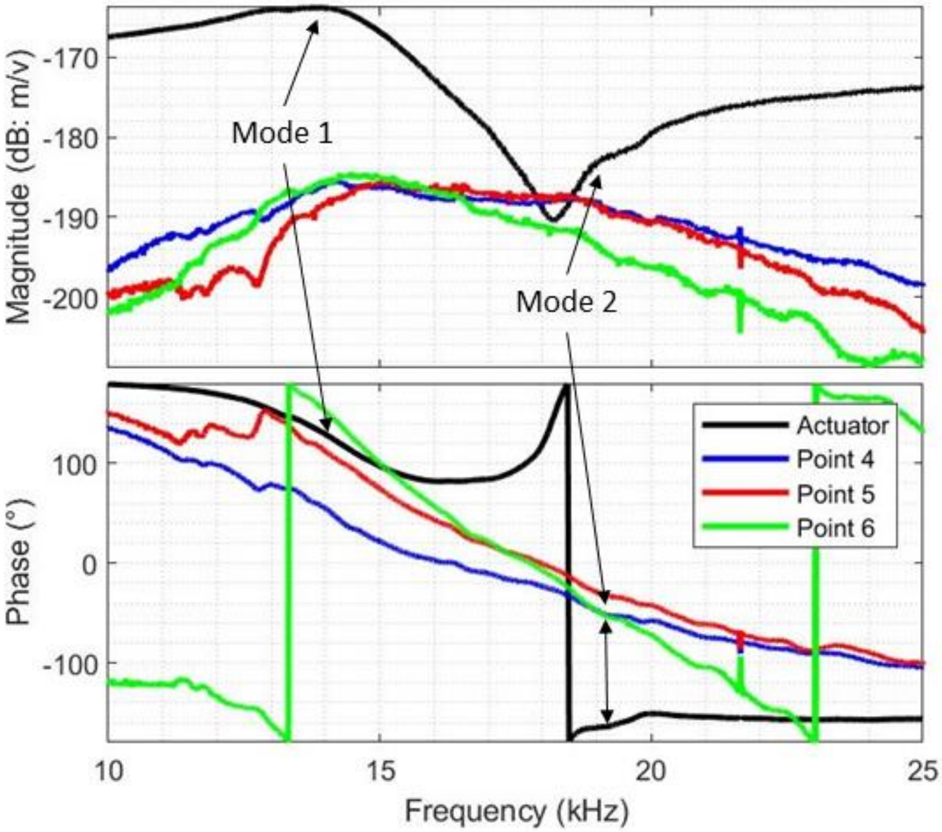

Figure 4.17. Frequency response function measurements in the channel for the case of actuator 1

Figure 4.18 shows several FRF measurements in the channel for the case of Actuator 2. As before, the black line is the measurement from the actuator; color lines are the measurements from the points on the membrane located above the actuator's plate. Mode 1 corresponds do the dominant peak that occurs around 22 kHz. At this frequency, points 4 and 5 are in phase with the actuator; point 6 is lagging by about 120 degrees. The amplitude difference between the actuator and membrane is about 30 dB, which corresponds to the amplitude ratio of about 30. The peak corresponding to mode occurs around 29 kHz. At this frequency, the phase difference between the actuator and membrane grew by 120 degrees. Point 6 is still lagging points 4 and 5 by about 80 degrees. The amplitude difference between the actuator and membrane is about 20 dB, which corresponds to the amplitude ratio of about 10.

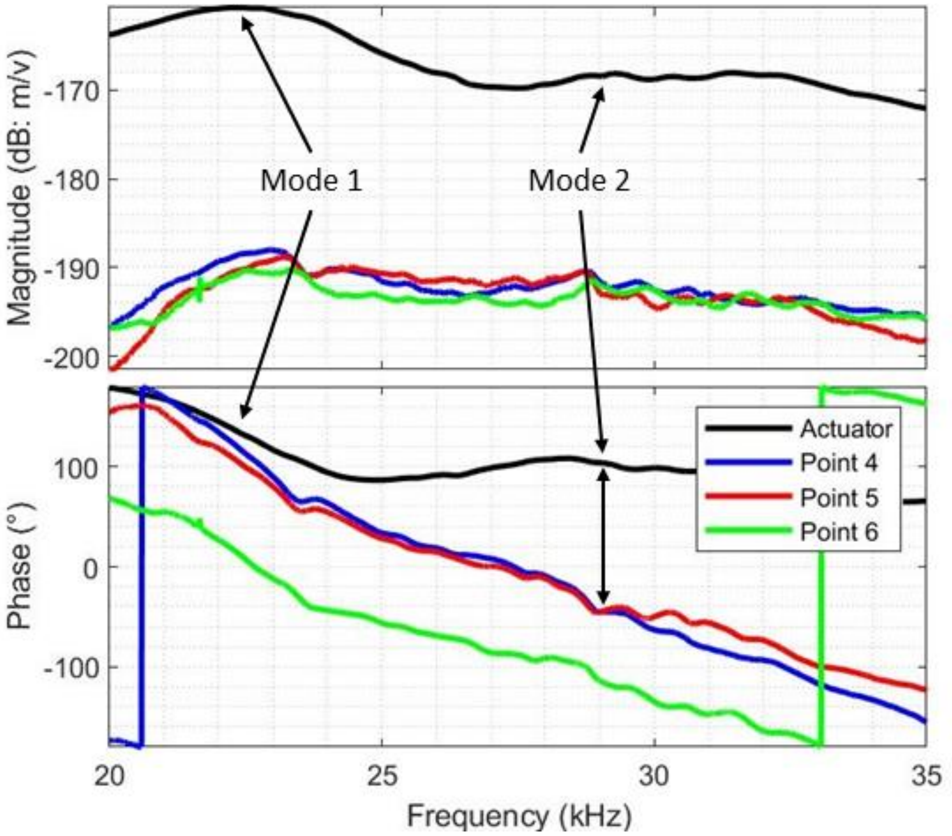

Figure 4.18. Frequency response function measurements in the channel for the case of actuator 2

Figure 4.19 shows several FRF measurements in the channel for the case of Actuator 3. Again, the black line is the measurement from the actuator; color lines are the measurements from the points on the membrane located above the actuator's plate. Mode 1 corresponds do the dominant peak that occurs around 12 kHz. At this frequency, the phase difference between the actuator and the points on the membrane is about 120 degrees; although, there is a small phase difference between three points. The amplitude difference between the actuator and membrane is more than 40 dB, which corresponds to the amplitude ratio of about 100. The peak corresponding to mode 2 occurs around 24 kHz. At this frequency, the phase difference between the actuator and membrane is less than 20 degrees. The amplitude difference is about 30 dB, which corresponds to the amplitude ratio of about 30.

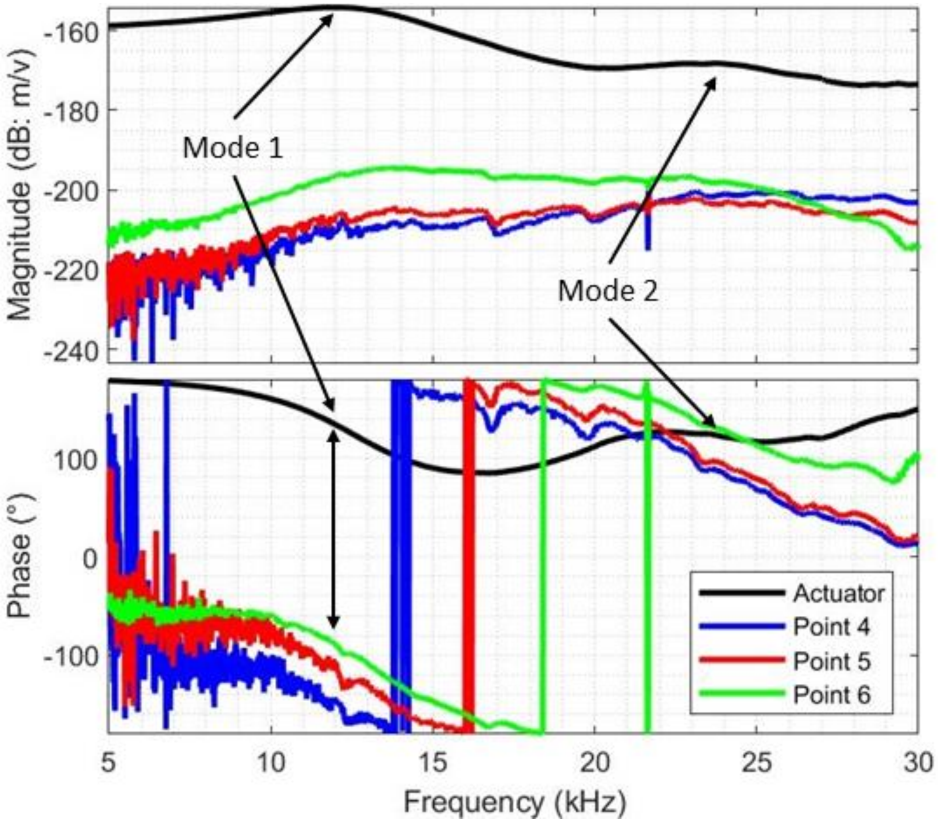

Figure 4.19. Frequency response function measurements in the channel for the case of actuator 3

The results predicted by the two-degrees of freedom model are compared to the results obtained in experiment in the Table 4.8. As seen, the frequency of mode 2 is predicted fairly accurately. The maximum relative error is under 10%. On the other hand, the phase difference and the amplitude ratio between the actuator and membrane predicted by the model significantly deviate from the experimental observations. For example, in the experiment, the amplitude ratio for mode 2 is smaller than for mode 1. The model, however, predicts the opposite. The numbers are quite different as well. These were not expected to match for several reasons. First, the FRF measurement of the actuator is taken from the back which can reduce its magnitude (refer to Section 3.3). Second, the magnitude of FRF at the resonance is governed by the damping ratio. Very wide peaks on the magnitude plots of FRFs indicate that the damping is significant in the experiment. Both, structural damping, and fluid viscosity can contribute to the damping mechanism, possibly making it frequency dependent. As a result, the amplitude ratios of two modes can be affected in a different way. The model does not include any damping.

Table 4.8. Comparison of experimental results with the results predicted by the two-degrees of freedom model

	Resonance Frequency (kHz)				Amplitude Ratio			
	Experiment		Simulation		Experiment		Simulation	
	Mode 1	Mode 2	Mode 1	Mode 2	Mode 1	Mode 2	Mode 1	Mode 2
Actuator 1	13.9	19	14	21	10	3	2	23
Actuator 2	22.2	29.2	22	28	30	10	5	20
Actuator 3	11.9	23.8	12	24	100	30	2	19

The phase difference between the actuator and membrane is another aspect not captured by the model. According to the model, the actuator and membrane should be out of phase at the lower frequency, and in phase at the higher frequency. The behavior may not be so extreme when the damping is present. Still, one would expect larger phase difference at the lower frequency, and a smaller phase difference at the higher frequency. In the experiment, this trend holds only for the actuator 3. For the actuators 1 and 2, the trend is the opposite. The bright side to this observation is that for actuators 1 and 2, the out of phase mode has a lower amplitude ratio. This is what the model predicts, except the frequencies of out of phase modes should be higher than the frequencies of in phase modes. If this is the case, then actuator 3 is once again an outlier. It should also be noted that the response of the membrane for the actuator 3 is the smallest among the three actuators. It is also larger at the higher frequency, the frequency of mode 2. For actuators 1 and 2, the membrane responds with the larger amplitude at the lower frequency, the frequency of mode 1.

In any case, it is clear that the two-degrees of freedom model cannot explain all experimental observations. One possible reason for the discrepancy is the assumed shape of the membrane. In the simulation, the membrane is very stiff and does not deform. Its motion is simply up and down. In the experiment, however, the motion of the membrane can be much more complex. FRF measurements indicate that there is a phase difference between the points on the membrane. For example, for actuator 1 vibrating at the frequency of mode 1, the motion of point 5 is almost in phase with the actuator. Point 4, however, is lagging behind, while point 6 is ahead. This indicates that the membrane may have a node in the vicinity of point 5. If this is the case, the two-degrees of freedom model is insufficient because it does not allow nodal points on the membrane. Higher fidelity model that includes the entire membrane might be necessary to explain experimental observation. Moreover, the vibration mode shapes of the membrane must be extracted from the frequency response measurements to justify the need for a more complicated model.

Also, the reader may wonder, if the shape of the membrane is important, how can such a simple model predict resonance frequency so well? This question can be answered by referring to the Rayleigh-Ritz method which is commonly used to estimate resonance frequencies and vibration mode shapes of the structure. A good overview of the method can be found in [35]. In short, for the discretized system, the square of the resonance frequency of a particular mode is given by the Rayleigh quotient:

$$R = \omega^2 = \frac{x^T K x}{x^T M x} = \frac{\sum_{i=1}^{n} \sum_{j=1}^{n} k_{ij} x_i x_j}{\sum_{i=1}^{n} \sum_{j=1}^{n} m_{ij} x_i x_j} \tag{4.3}$$

where $K\ and\ M$ are $n \times n$ stiffness and mass matrices of the system; x – is the vector representing vibration mode shape. As seen, the Rayleigh quotient is the ratio of two quadratic forms representing potential and kinetic energy of the system. Under the summation, the shape of the mode gets smoothed out. In addition, the membrane's displacement is much smaller than the displacement of the actuator; therefore, its contribution to the summation is much smaller as well. As a result, if the parameters of the system are chosen correctly (which seems to be the case here), the model will predict resonance frequency with a reasonable accuracy.

4.3 MEMBRANE'S MODE SHAPES VIA PRINCIPAL COMPONENT ANALYSIS

In order to justify the need for a more sophisticated model, it is important to understand how the membrane moves in the experiment. In the previous section, it was pointed out that there might be a nodal point on the membrane along its length. If this is the case, the model that includes the entire elastic membrane is necessary to explain experimental observations.

There are multiple ways to extract vibration mode shapes from the frequency response measurements. Perhaps, the simplest one, is to calculate the displacement of each measured point using magnitude and phase information of the FRF according to:

$$Y_p^f = \left\| FRF_p^f \right\| \cdot cos\left(2\pi f t + \angle FRF_p^f\right) \tag{4.4}$$

where subscript p stands for point (29 measured points for actuator 1; 31 for actuators 2 and 3), and superscript f stands for frequency (2047 measured frequencies). The time t, can be chosen arbitrary as long as it is the same for all points at the given frequency. Once the displacement of each point at the given frequency is obtained, it can be potted in 2D plane against the coordinates of the points along the length of the membrane X_p. The plotted points are than connected to obtain the mode shape of the membrane along its centerline. This method is very easy to implement but it is prone to errors. It only uses the single measurement of magnitude and phase to calculate the displacement of the point at the given frequency. In the current experiment, the magnitude of FRFs is very small (fraction on the nm). Relying on the single measurements, especially when the values are so small, is not a good practice.

Another method that is commonly used to extract vibration mode shapes is called “Circle Fit”. The mathematical details of the method can be found in [36]]. In this method multiple measurements around the resonance are used to calculate the displacements of a particular point. Because the method relies on the multiple measurements, it is less prone to error as compared to the method described above. However, for the Circle Fit to work, the behavior of the system at the resonance must be similar to the behavior of a single degree of freedom system. In other words, the response at the resonance should be dominated by a single mode. For this to be true, the resonance peaks on the FRF need to be distinct. This is not the case in the current experiment as evident from the Figure 4.17 through Figure 4.19. Moreover, the resonance peaks on the magnitude plots from different points are not aligned. Setting frequency bounds for the data used in calculation that are consistent between different points is impossible. As a result, the method should not be used on the current data.

Finally, the method that is used here relies on the principal component analysis (PCA). A good overview of PCA can be found in [37]. PCA has been used for over a century in the variety of applications. It has many names depending on the field of science it used in. For example, in mechanical engineering it is known as proper orthogonal decomposition (POD); in linear algebra it is called singular value decomposition (SVD). Here, the method is first used to clean up the collected data, and then to extract the mode shapes. The beauty of the method is that the entire dataset is involved in the process.

The first step in this method is to assemble a matrix of mode shapes. Each column in the matrix is the vibration mode shape calculated using Equation 4.4. The matrix is arranged such that the first column is the mode shape of the lowest frequency; the last column is the mode shape of the highest frequency. The resulting matrix has about 30 rows and 2047 columns (29×2047 for actuator 1, and 31×2047 for actuators 2 and 3). The next step is to decompose the matrix into a product of three matrices:

$$M = USV^T \tag{4.5}$$

where U (30×30) and $V(2047 \times 30)$ are orthonormal matrices; $\mathrm{S}(30 \times 30)$ is a diagonal matrix of singular values arranged in descending order ($\mathrm{S}_1 > \mathrm{S}_2 > \cdots > \mathrm{S}_{30}$). To see the value of this decomposition, Equation 4.5 can be written in the form:

$$M = U_1 \mathrm{S}_1 V_1^T + U_2 \mathrm{S}_2 V_2^T + \cdots = \sum_{i=1}^{30} U_i \mathrm{S}_i V_i^T \tag{4.6}$$

where U_i and V_i are i-s columns of U and V, respectively, S_i is corresponding singular value. Figure 4.20 shows several columns of U and V matrices for actuators 1, 2, and 3. Since S_1 is the largest singular value, the shape captured by the first column of U is the most dominant shape in the entire dataset. Its magnitude as a function of frequency is governed by the first column of V. For example, for the actuator 1, the shape given by U_1 has the largest contribution around 14 and 17 kHz; although, the shape is flipped about x-axis at 17 kHz because V_1 is negative there. The next in line is the shape given by U_2, then the shape given by U_3, and so on. It is also noticeable, that the first several columns of V have some structure. The values in these columns increase, and then decrease, peaking around frequencies some of which correspond to the peaks on the FRFs measurements for

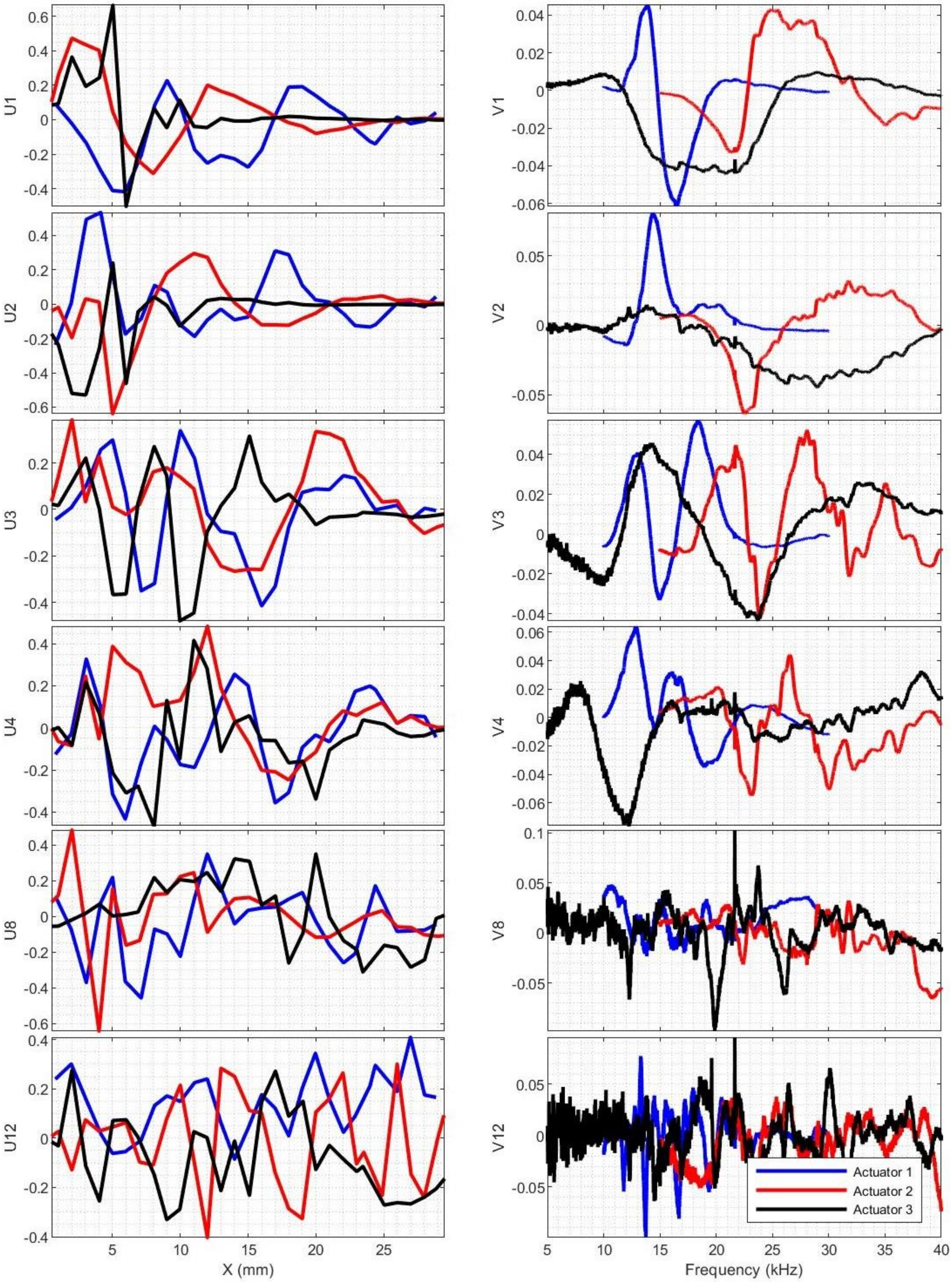

Figure 4.20. Selected columns of U and V matrices for actuators 1, 2 and 3

various points on the membrane. Eventually, this structure is lost. For example, V_8 and V_{12} look more like signals generated by electrical noise. The same observation applies to the corresponding columns of U. If these terms are removed from the summation given by Equation 4.6, the data may become cleaner.

However, before removing any terms from the summation, it is important to estimate their contribution to the dataset. This can be done by looking at the singular values. One way to estimate the contribution of individual terms is to calculate the ratio given by Equation 4.7 for each singular value. The results of this calculation are shown in Figure 4.21 (left).

$$\mathrm{S}_{R_i} = \frac{\mathrm{S}_i}{\sum_{k=1}^{30} \mathrm{S}_k} \tag{4.7}$$

Perhaps, a more useful indicator, is a cumulative ratio given by Equation 4.8. The results are also shown in Figure 4.21 (right).

$$\mathrm{S}_{C_i} = \frac{\sum_{k=1}^{i} \mathrm{S}_k}{\sum_{k=1}^{30} \mathrm{S}_k} \tag{4.8}$$

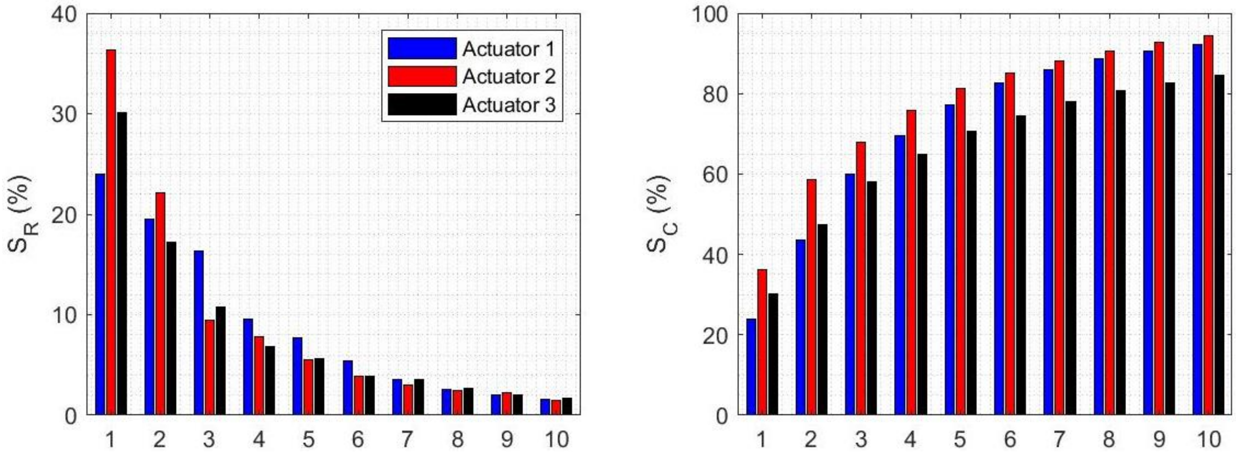

Figure 4.21. Ratio of singular values given by Equation 4.7 (left) and a cumulative ratio given by Equation 4.8 (right) for actuators 1, 2, and 3

Figure 4.21 reveals that the contribution of the first component along varies between 24 and 36 % for the different actuators. It seems that the contribution of the following components decays in the exponential manner to about 2% for the 10th component. Together, the first 10 components capture between 80 and 90% of the datasets. However, it is not clear where the summation given by Equation 4.6 should be cut. Leaving fewer components in the summation may compromise the integrity of collected data, because some of the components that are cut may represent the actual dynamic of the system. On the other hand, keeping too many components will leave most of noise in the data intact. It was already pointed out that 8th component looks like a noise, but 8 components together represent under 90 % of the dataset. With such small measurements, it is possible that 8 components are already too many.

To help solve this dilemma, it can be beneficial to look at the singular values from a different perspective. The variance in data captured by a particular component is related to a corresponding singular value by the following equation:

$$\sigma_i^2 = \frac{\mathrm{S}_i^2}{n-1} \tag{4.9}$$

where n – is number of measurements, or number of points in this case. The variance along, just like a singular value by itself, does not tell much of the story. More useful numbers are relative and cumulative variances given by Equations 4.10 and Equation 4.11, respectively. The calculations are presented in Figure 4.22.

$$\sigma_{R\,i}^2 = \frac{\mathrm{S}_k^2}{\sum_{k=1}^{30} \mathrm{S}_k^2} \tag{4.10}$$

$$\sigma_{C\,i}^2 = \frac{\sum_{k=1}^{i} \mathrm{S}_k^2}{\sum_{k=1}^{30} \mathrm{S}_k^2} \tag{4.11}$$

It is interesting to note, that for actuators 2 and 3, over 60% of variance in data are captured by a single component. For actuator 1, the 60% is split between components 1 and 3. The reason for this discrepancy is not clear. Moreover, over 95 % of variance in data for all three actuators are captured by the first five components. It is believed that the large variance represents the true dynamics of the system. Afterall, large variance in data corresponds to large motion. Therefore, the mode shape matrix can be safely approximated by the first five terms in the summation, capturing over 95% of the system dynamics.

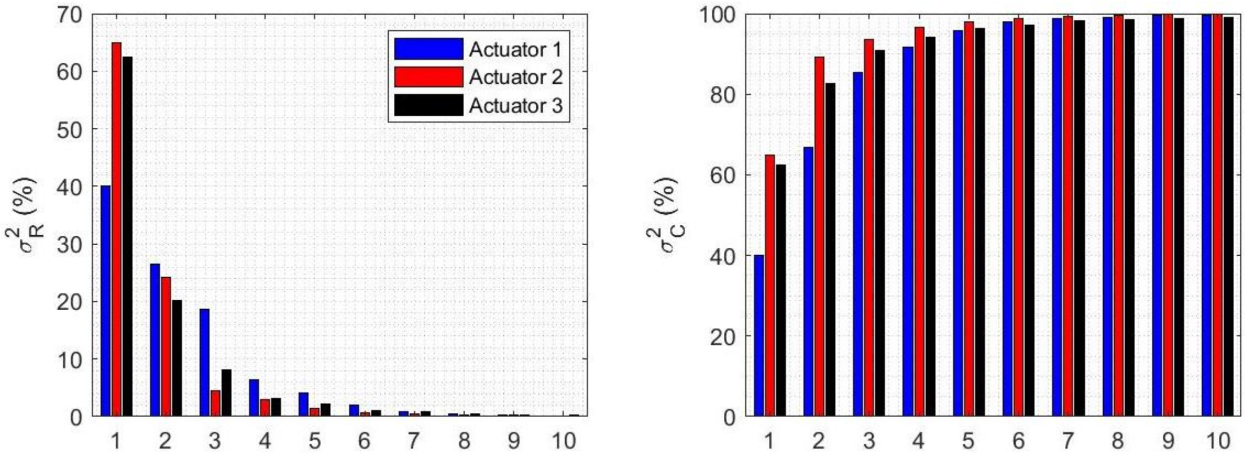

Figure 4.22. Relative variance given by Equation 4.10 (left) and a cumulative relative variance given by Equation 4.11 (right) for actuators 1, 2, and 3

Once the noise is removed from the mode matrix, the vibration mode shapes can be extracted. In vibration theory, the expansion similar to the one given by Equations 4.6 is often used to express the shape of the vibrating structure in terms of its eigenmodes. For example, the eigenmodes of the string fixed at both ends are sinusoids of increasing frequencies. The lowest eigenmode is when the entire string goes up and down. It corresponds to the sinusoid with the period equal to the twice the length of the string. The next eigenmode is when one half of the string goes up, while the other goes down. It corresponds to the sinusoid with the period equal to the length of the string. It has one nodal point in the middle – the point that does not move. The next eigenmode has two nodal points, and so on. These eigenmodes are vibration mode shapes of the string at corresponding resonance frequencies. The higher the frequency, the more complicated the corresponding eigenmode. At frequency other than resonance frequency, the vibration mode shape can be expanded in terms of these eigenmodes. Even though the eigenmode expansion is similar to the one described here, it is important to understand that the shapes captured by the columns of U matrix do not necessarily represent eigenmodes. However, if the single component of U can capture most of the system dynamics, then its shape is the vibration mode shape.

Of course, over the wide range of frequencies, the vibration mode shape of the membrane cannot be captured by the single component as evident from the Figure 4.22. The reason is simple, its changes with frequency. Similar to the string, the membrane may have a simpler shape at lower frequency, which may become more complex as the frequency is increased. However, over a small range of frequencies, the vibration mode shape of the membrane may not change by much. If the PCA is performed on the small portion of the mode shape matrix, the single component can capture the vibration mode shape. Figure 4.23 shows results produced by this method. Here, the mode shape matrix obtained in the previous step was truncated to a hundred consecutive measurements centered on the frequencies of mode 1 and mode 2 from the Table 4.8. The resulting matrix (30×100) was approximated using a single component that captured on average 93% of the mode's dynamics. Then, the mean over columns was taken to produce the results. The Matlab code can be found in the appendix (Note: the results for actuator 3 were magnified by a factor of 5 for a better comparison).

The results shown in Figure 4.23, although still very noisy, clearly show that the motion of the membrane is much more complicated than just up and down motion that two-degree of freedom model is capable to predict. The suspected nodal point directly above the actuator's plate ($X \approx 5\ mm$) seems to exist in mode 1 for all three actuators. As a result, the phase difference between the actuator and membrane predicted by the two-degree of freedom model cannot be used to explain experimental observation. A more sophisticated model that include the entire elastic membrane is necessary.

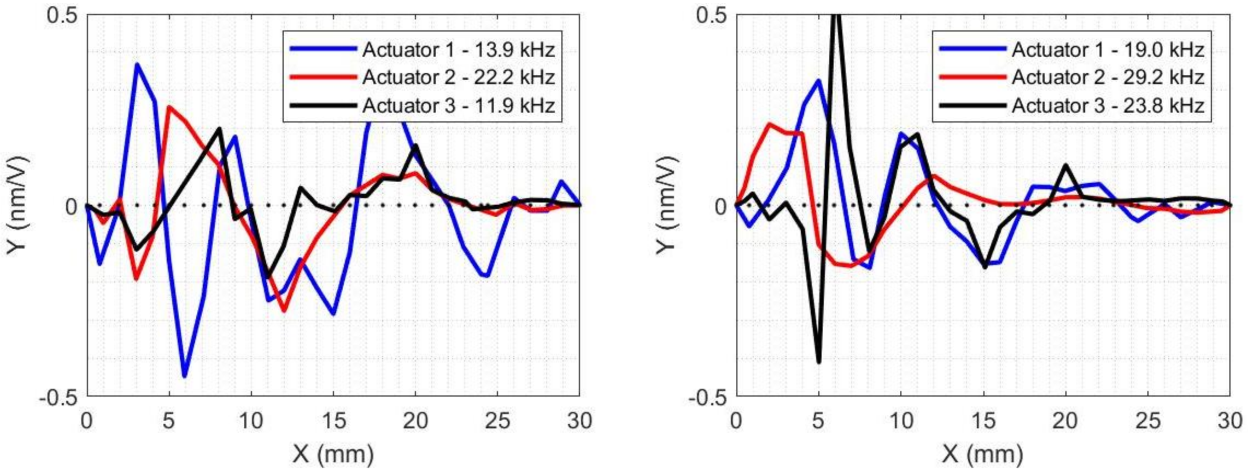

Figure 4.23. Membrane's mode shapes at the frequency corresponding to mode 1 (left) and mode 2 (right) for actuators 1, 2, and 3

Although, the concrete conclusion about the shape of the membrane cannot be made with such small measurements, some observation a worse noting. First, the shapes of the membrane in mode 1 for actuators 2 and 3, as well as the shape in mode 2 for actuators 1 and 3 resemble similarities in the number and location of nodal points. Second, the shape of the membrane for actuator 2 as well as the shape for actuator 1 in mode 2 look like sinusoids whose amplitudes decreases toward the end of the cavity. Such shapes are similar to the eigenmodes of the string fixed at both ends with material properties gradually changing along its length. Of course, the membrane is not a string, but its width is decreasing towards the end of the cavity, resulting in the increase in bending stiffness and decrease in mass. Since the mode shapes are captured along the centerline, the similarities with the string are not surprising.

This observation has prompted a search for the mode shapes that may look like eigenmodes. The results of the search for actuators 1 and 2 are shown in the Figure 4.24 (Note: the results for actuator 1 at 25.3 kHz and actuator 2 at 18.2 kHz were multiplied by a factor of -5 for a better comparison). The search performed on the data from actuator 3 did not yield any results worse showing.

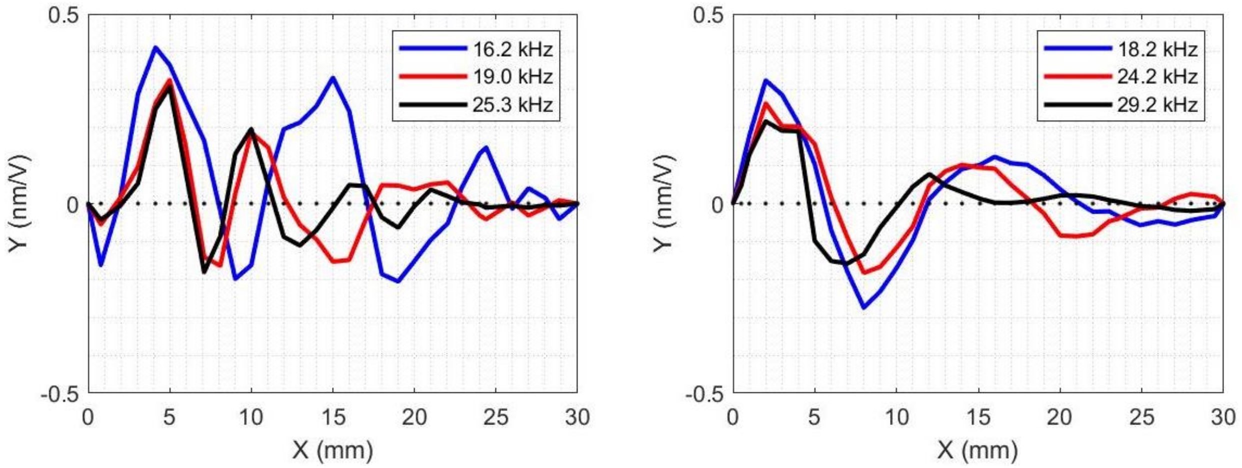

Figure 4.24. Membrane's mode shapes at selected frequencies for actuator 1 (left) and actuator 2 (right)

Again, some observation can be noted from the presented results without making any concrete conclusions. First, the shape of the membrane for both actuators seems to become more complex (more nodal points) as the frequency increases. Second, the shape of the membrane is more complex for actuator 1 that it is for actuator 2, even though the frequencies corresponding to these shapes are lower for actuator 1. Involving string analogy again, this observation indicates that the membrane corresponding to the actuator 2 is much stiffer than the membrane corresponding to the actuator 1. Recall, when two-degrees of freedom model was used, the spring stiffness had to be set to a much higher value to match experimental observation for the actuator 2. It is not clear why the membrane in the case of actuator 2 seems to be stiffer. Perhaps the stress induced during the assembly could play a role, or the glue used to assemble experimental setup may have leaked in the cavity stiffening the membrane.

4.4 FULL MODEL

The results of PCA clearly show that the membrane mode shapes are very complicated and cannot be predicted by the two-degrees of freedom model. To obtain such mode shapes, the entire elastic membrane needs to be modeled. Figure 4.25 shows the geometry and dimensions of the full model that mimics experimental setup.

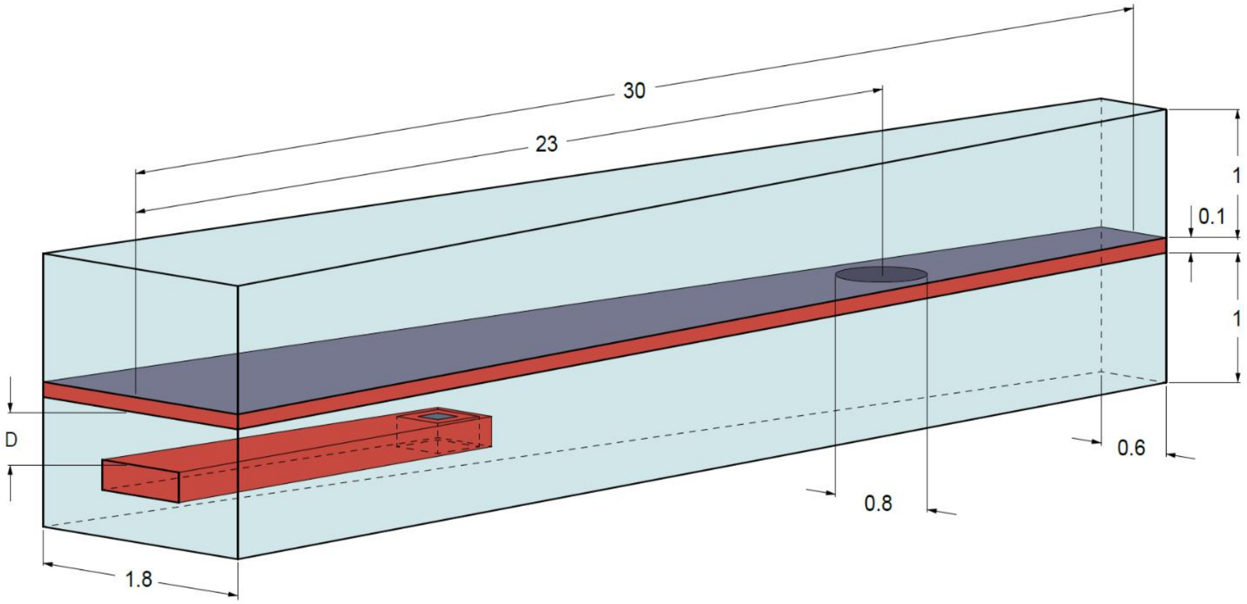

Figure 4.25. Full model with dimensions (mm)

Here, two fluid channels are connected together through the 800 μm hole in the membrane. The boundary conditions on all outside surfaces of the fluid are left out, implying zero fluid velocity (as a reminder, this is the default boundary condition in Ansys Acoustics modal analysis). A 100 μm thick aluminum membrane separates two fluid channels. The “fluid-structure interaction boundary condition” is set on the top and bottom surfaces of the membrane and on the surface created by the hole. The membrane is held in place by setting the displacement on its side surfaces (shown in red) to zero. The Young’s modulus and the density of the membrane are set to 71 GPa and 2770 kg/m^3, respectively, matching the properties of the aluminum from the Ansys database.

The parameters used to model the actuator can be found in Table 4.6 (Actuator 1 is used in the discussion that follows). In the full model, the support structure around actuator’s plate is extended to include the entire beam. Its dimensions can be found in the Figure 2.3. To simplify the analysis, the displacement of the support structure is set to zero. This simplification is justified because the magnitude of FRF taken from the point on the actuator’s beam is much smaller than the magnitude of FRF taken from the point on actuator’s plate (cf. Chapter 3). “Fluid-structure interaction boundary conditions” are imposed on all actuator’s faces in contact with the fluid.

The model is meshed using 80 μm quadratic elements. The actuator’s plate (including residues) is meshed first using a single layer of elements. Then, the single layer of elements is created on the top surface of the support structure and on surface of fluid surrounding it. This layer is swept up and down through the entire model to create a nicely arranged, hexahedral mesh. As a result, the mesh around actuator’s plate is very similar to the mesh used in the single and two-degrees of freedom models. The entire model contains around 76000 elements.

The results of the modal analysis performed on the model described above reveal many different mode shapes. In some of them, the membrane vibrates with a much larger amplitude than the actuator; in other, the actuator’s amplitude is much larger. There are also modes where the vibrations amplitudes of the actuator and membrane are comparable. In addition, there are very odd-looking modes that might be associated with acoustic modes of the fluid cavity. It is known that the frequency of acoustic modes in trapezoidal cavity, as well as in rectangular, are inversely proportional to the dimensions of the cavity [38]. When a single or two-degrees of freedom models were used, acoustic modes occurred at high frequency, outside of the range of interest. With the full model, the longitudinal dimension of the cavity has increased by 15 times. As a result, the frequency of acoustic modes might be in the range of interest of the analysis. These acoustic modes can significantly affect the frequencies of structural modes as shown in [39]. However, the results extracted from the full model are difficult to analyze on its own because the effect of coupling on the frequency of the components comprising the model is unclear. To solve this issue, each component can be analyzed separately. Once the behavior of each component is understood, the membrane and the fluid can be combined to see the effect of coupling between the membrane and the fluid. Finally, the results of the full model can be analyzed to understand the interaction of the actuator with a fluid-membrane system.

Figure 4.26 presents the first ten natural frequencies and corresponding mode shapes of the aluminum membrane in vacuum (the hole is on the left side). The natural frequencies are quite high; however, they are expected to become much lower when the membrane is coupled with the fluid in the channel. It is clear, as the natural frequency of the membrane increases, the corresponding mode shapes become more complex. This behavior is similar to the behavior of the string discussed in Section 4.3. Thus, in mode 1 the membrane does not have any nodal points along its middle section. In mode 2, one nodal point appears; in mode 3, two nodal points; in mode 4, three, and so on. It is also interesting to note, that the region of the maximum deformation of the membrane moves toward its narrow end as the frequency increases. Pass this region, the deformation of the membrane is negligible.

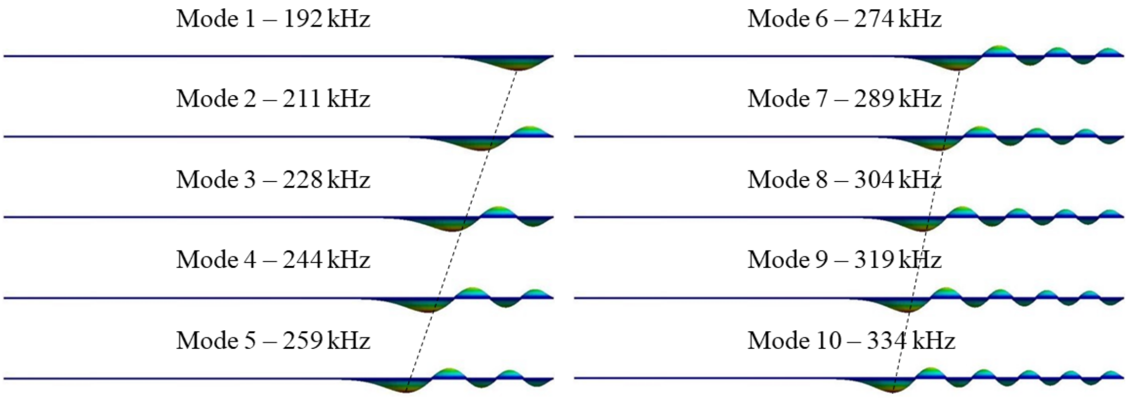

Figure 4.26. Membrane’s mode shapes and corresponding natural frequencies in vacuum

Figure 4.27 presents the first ten acoustic natural frequencies and corresponding mode shapes extracted by performing modal acoustic analysis on the fluid cavity (2 channels connected by the hole). The results can be grouped in two categories: modes corresponding to odd numbers (shown on the left), and modes corresponding to even numbers (shown on the right). For even modes, the pressure distribution in both channels is identical along the length of the channels; for odd modes, the pressure is opposite. The modes become more complex as the frequency increases. Thus, mode 1 has 1 node along the middle section of the cavity; mode 2 has 2; mode 3 has 3 and so on. However, the trend is broken in mode 5 which has only one node at the hole, where the channels are connected. In fact, all odd modes have a nodal point at this location. The whole serves as a boundary for odd modes. The pressure disturbance can propagate along the channels by taking a long pass from the wide side of one channel through the whole to the wide side of another channel (red dashed line), or short pass from the narrow side of one channel through the whole to the narrow side of another channel (black dashed line). As the frequency increases, more nodes appear along each pass. For the even modes, the pressure disturbance propagates along both channels simultaneously. The order of natural frequencies seems to depend on the length of the pass.

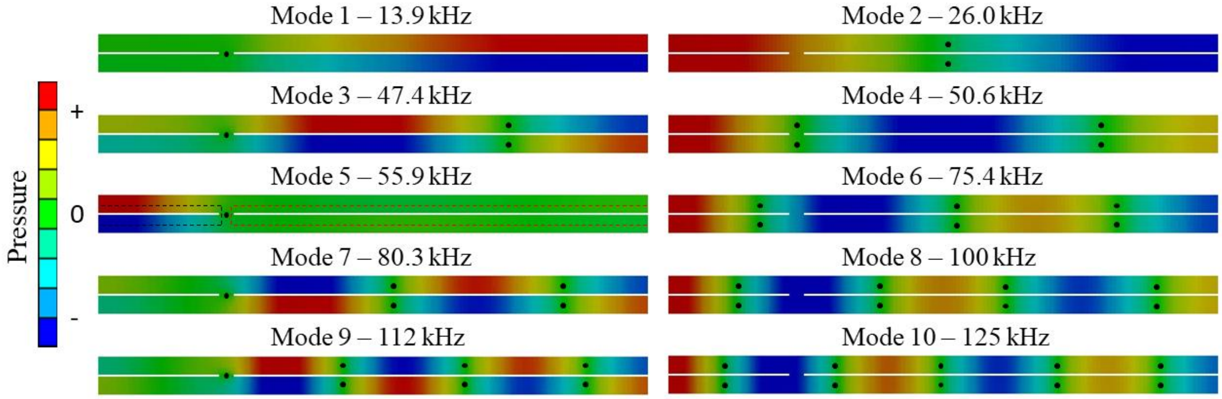

Figure 4.27. Acoustics mode shapes and corresponding natural frequencies

When the membrane is combined with the fluid channels, the acoustic and structural modes become entangled. The first ten natural frequencies and corresponding mode shapes of the system are presented in Figure 4.28. There are several observations that can be made. First, there are few structural mode shapes that look very strange (modes 3, 6, and 9). It is not clear what kind of deformation the membrane undergoes in these modes. The corresponding pressure distributions are very similar to pressure distributions of even acoustic modes.

The rest of the structural modes are comparable to the membrane's mode shapes in vacuum. Mode 1 has no nodal points; mode 2 has one; mode 4 has two, and so on. However, the shape of these modes and their frequencies have changed. The region of maximum deformation does not propagate toward the narrow end of the membrane as the frequency is increased. The location of maximum deformation seems to move back and forth, guided by the pressure distribution in the channels. In addition, the deformation of the membrane on both sides of this region is non-negligible. The corresponding pressure distributions are very similar to pressure distributions of odd acoustic modes.

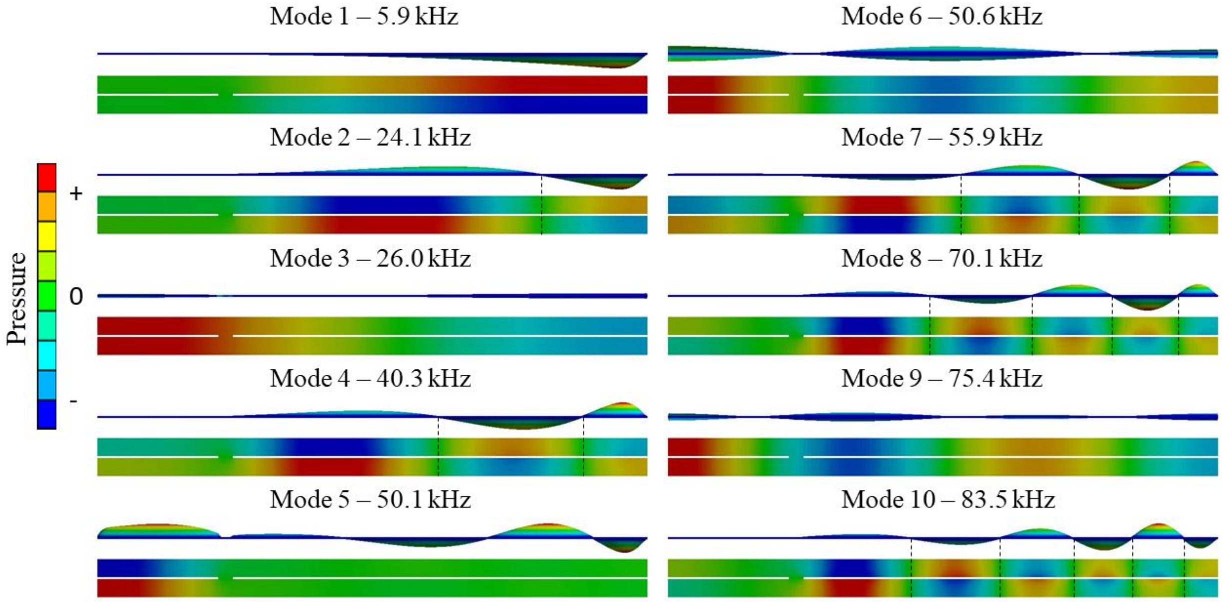

Figure 4.28. Acoustic and structural mode shapes and corresponding natural frequencies of the system that includes membrane and fluid channels

Another observation is that the acoustic and structural nodes are aligned. This observation can help explain why the shape of structural modes have changed. For example, the pressure distribution of mode 4 of the fluid-membrane system (FM4) look very similar to the pressure distribution of the mode 7 of the fluid-only system (F7). The corresponding membrane's deformation looks like a deformation of mode 3 of the membrane-only system (M3). Thus, it is reasonable to conclude that modes F5 and M3 are the most dominant contributors to the formation of mode FM4. The formation mechanism is shown in the Figure 4.29.

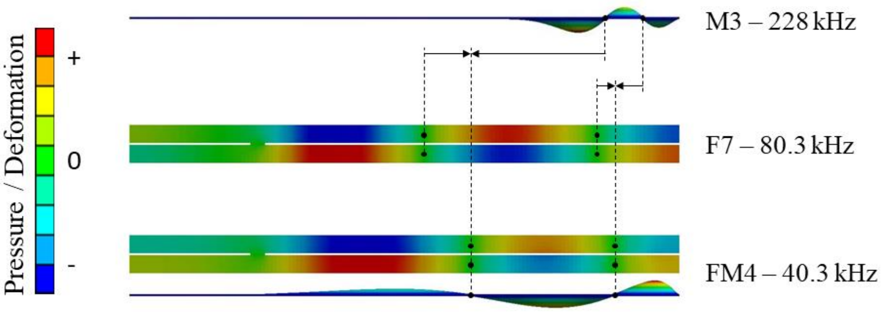

Figure 4.29. The formation of the mode shape of the fluid-membrane system

Here, the shape of the membrane has changed when it was introduced in the fluid channels because its nodes move in the direction of the acoustic nodes. The pressure distribution is affected as well because acoustic nodes move towards structural nodes. The resulting frequency is also different. However, the effect of acoustic modes on natural frequencies of the membrane cannot be determined because the contribution of the added mass from surrounding fluid and walls of the cavity is unknown. Most of the modes of combined system shown in the figure are formed in a similar way. Mode 5 (FM5) is an exception. There are more than two components that contribute significantly to its formation. It should be clear that the transverse deformation of the membrane is possible only when the pressure distribution in two channels along its length is different. Therefore, even acoustic modes do not couple to the structural modes shown in Figure 4.26.

Now, that the coupling between the membrane and the fluid in the channels is understood, the results of the full system can be analyzed. The behavior of the actuator is already well known (cf. Section 4.1). The inclusion of the entire beam in its model does not affect its behavior because the beam is assumed to be stationary. For the case of Actuator 1 modeled here, the frequency of its first mode in the petri dish (infinite fluid domain) is 21.4 kHz. The next two natural frequencies correspond to the symmetric modes occurring at 63.7 kHz. Higher modes are outside of the range of interest. The first three mode shapes of the actuator’s plate are shown in the Figure 4.30.

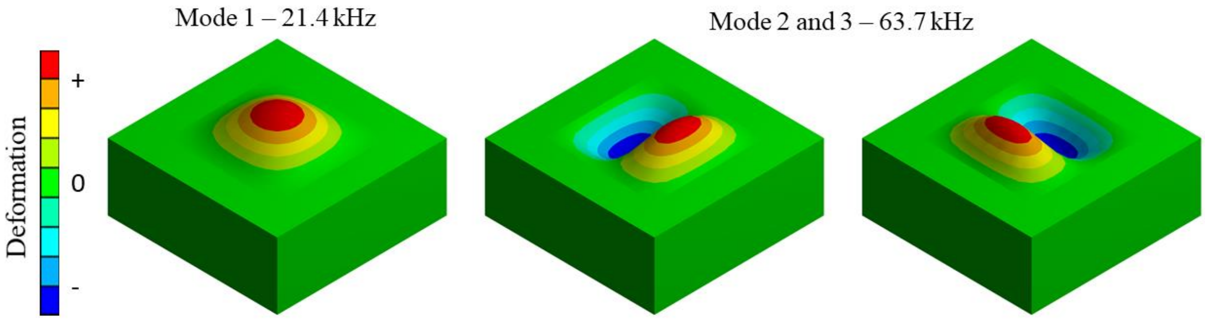

Figure 4.30. Actuator’s mode shapes and corresponding natural frequencies in the petri dish

The results of modal acoustic analysis performed on the full model are presented in the Figure 4.31. The column on the left shows first 10 structural and acoustic mode shapes for the case when actuator is located 300 μm form the membrane; the column on the right corresponds to the case when actuator is 50 μm from the membrane. The results for mode 2 also include the magnified shape of the membrane.

There are several observations that can be noted. First, there are many mode shapes that are indicative of the fluid-membrane system. For example, focusing on the case when the actuator is 300 μm from the membrane, the shapes of mode 1 and modes 3 through 8 look very similar to the first 7 mode shapes of the system without actuator. Modes 2, 9, and 10, however, are new They are the result of adding the actuator to the system. From the perspective of vibration theory, this observation makes perfect sense. Adding new degrees of freedom to the system increases the number of modes. The vibration shapes of the actuator in these modes are similar to the ones shown in Figure 4.30. The pressure distributions are localized around actuator and are comparable to the pressure distributions predicted by the single degree of freedom model. Mode 2 is most likely corresponds to one of the dominant peaks on the FRF measured in the experiment.

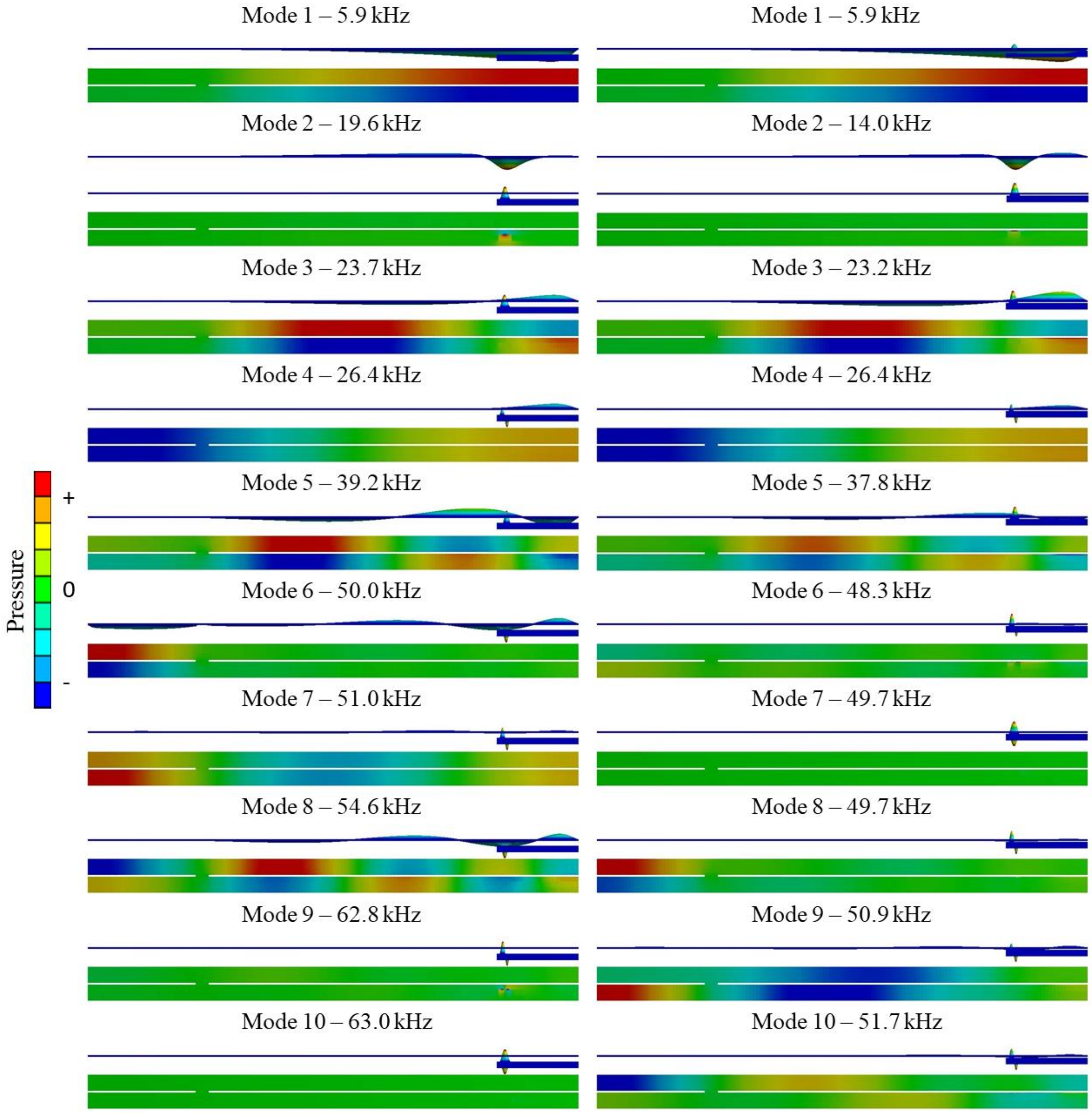

Figure 4.31. Mode shapes and corresponding natural frequencies predicted using full model for the actuator located 300 μm (left) and 50 μm (right) from the membrane

Second, the coupling of the actuator with the fluid-membrane system is not as strong as the coupling of the fluid and membrane. When the fluid-membrane system was formed, the frequency of some odd acoustic modes dropped by more than 50%. For example, the frequency of the acoustic mode 1 dropped from 13.9 kHz to 5.9 kHz when it coupled with the first structural mode of the membrane to form a first mode of the combined system. When the actuator was added, the frequency of the first mode has not changed. However, the frequency of mode 2, the mode of interest, has decreased from 21.4 to 19.6 kHz indicating an increase in added mass of the actuator. The effect of structural coupling between the actuator and membrane can be estimated by comparing the frequency of mode 2 in the channels to the frequency predicted by the single degree of freedom model. The frequencies of the actuator located 300 and 50 μm from the wall are 20.3 and 14.6 kHz, respectively. In the channel, the frequency of mode 2 for the actuator located at the same distances from the membrane, the frequencies are 19.6 and 14.0 kHz. Thus, the structural coupling reduces natural frequencies by about 4% in these cases, further contributing to the added mass that actuator experiences.

Third, the vibration of the actuator and membrane starts out of phase in mode 1 and mode 2. In mode 3, the actuator seems to be in phase with a lobe on the membrane; although, there is a nodal point nearby. Such behavior is consistent with the one predicted by the two-degrees of freedom model. In experiment, it seems to be the opposite. Also, the shape of the membrane in the experiment looks more complex. Since the membrane measurements are very small, and there is also some uncertainty in the location of the actuator's plate relative to the nodal point, it is impossible to make any definite conclusions. However, the similarities between experiment and simulation, such as phase reversal, and the presence of the nodal point, are apparent.

Forth, the presence of the actuator destroys the order in which complexity of the membrane vibration shape is increasing with frequency. Before the actuator was added to the system, the number of nodes on the membrane was increasing in orderly manner. With the actuator in, the are no nodes on the membrane in mode 1, two nodes in mode 2, one node in mode 3, no nodes in mode 4, two nodes in mode 5, and so on. Moreover, mode 4, where pressure distribution corresponds to the even acoustic mode, is coupling to the structural modes of the membrane. The presence of the actuator altered the pressure distribution in the lower channel, allowing the membrane to vibrate.

Lastly, moving the actuator closer to membrane significantly affects the frequency of the modes which were introduced into the system with the actuator. The frequencies of the modes associated with the fluid-membrane system change very little. This observation can be explained by referring to the pressure distributions. For the actuator's modes (modes 2, 9 and 10 when actuator is 300 μm from the membrane) the pressure distribution is very localized. When the actuator is brought closer to the membrane, it changes in the similar way as when the actuator is brought closer to the wall (cf. Section 4.1). Since the deformation of the actuator in these modes is much larger than the deformation of the membrane, changes in pressure distribution lead to a change in natural frequency of the mode. For the modes associated with the fluid-membrane system, the deformation of the membrane is comparable to the deformation of the actuator. When the membrane vibrates, the pressure through the entire fluid domain is affected. The local change in pressure distribution around actuator caused by moving it closer to the membrane has very little effect on the pressure distribution in the channels. As a result, the frequency of these modes, as well as its mode shapes remain essentially unchanged.

To conclude the study, it can be valuable to understand whether the behavior of the system will change if the membrane stiffness is reduced. This step may also bring the experimental and numerical results in a better agreement, as the mode shapes obtained in the experiment seem to be more complex than mode shapes obtained in the simulation indicating that the membrane in the model might be too stiff. The reason behind the disagreement might be a stress induced in the membrane during the assembly of the fixture. Also, the Young's modulus of aluminum foil used to model the membrane is that of the bulk aluminum. In reality, it can be much lower as shown in

[40]. Figure 4.32 compares the first five natural frequencies and corresponding mode shapes obtained from the simulation. The column of the left corresponds the case described above for the actuator located 300 μm from the membrane. The column on the right corresponds to the case where the membrane Young's modulus is reduced from 71 to 10 GPa.

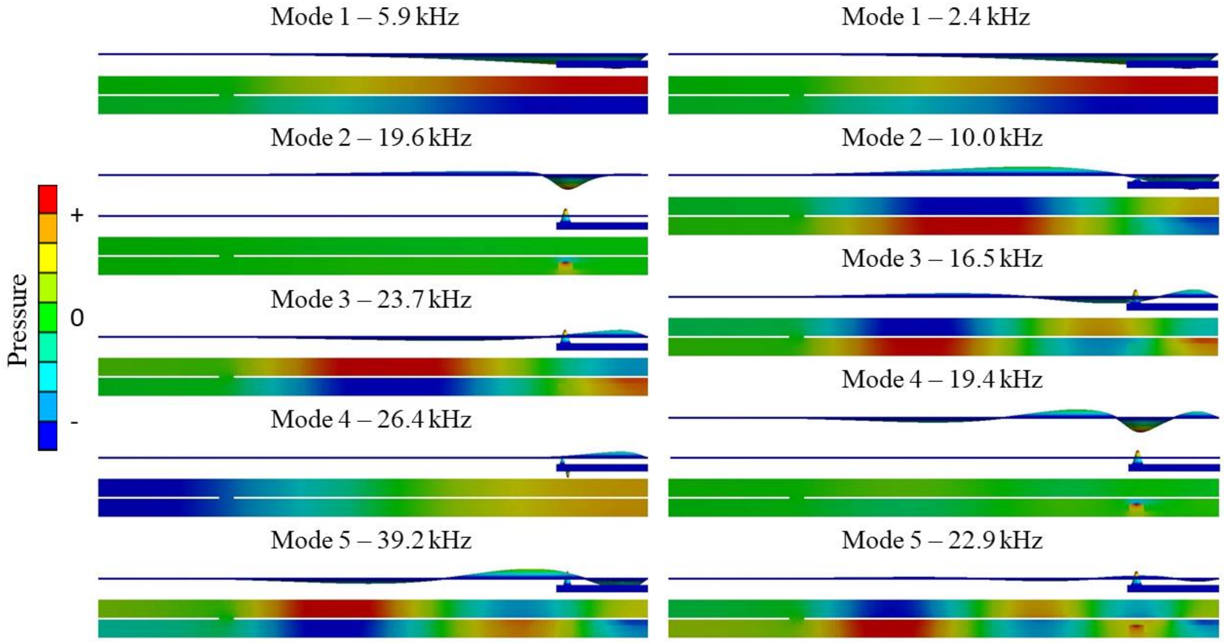

Figure 4.32. Mode shapes and corresponding natural frequencies predicted using full model for the actuator located 300 μm from the membrane

It can be noted that the overall behavior of two systems with different membranes is very similar. The actuator is out of phase with the lobe on the membrane until the frequency of the actuator's mode is reached. Pass this frequency, the vibrations are in phase. The modes associated with the fluid-membrane system and the mode associated with the motion of the actuator are easy to distinguish. In fact, the frequency of the actuator's mode remained almost unchanged. The frequencies of the modes associated with the fluid-membrane system dropped as expected; however, its mode shapes did not change. As a result, the vibration shape of the membrane at the frequency of the actuator's mode is now more complex. The relative amplitudes of the actuator and membrane are also changed. There are now 2 modes (mode 4 and 5) where the actuator’s deformation is much larger than the deformation of the membrane. These observations suggest that the properties of the membrane can be adjusted to bring numerical results in the agreement with the results observed in the experiment. However, since there is a lot of uncertainty in the membrane mode shapes due to its very small deformation, matching experimental and numerical results is not pursued.

Chapter 5. CONCLUSIONS AND FUTURE WORK

The experimental and numerical studies conducted in the research project lead to the following conclusions:

- ✓ The reduction in static gain observed in experiment when actuators 1 and 2 are placed inside the fluid channels is caused by experimental inaccuracy. In particular, in measurements of actuator's FRF in the channel, the large portion of the laser beam was reflected from the support structure which has negligible deformation as compared with the vibrating potion of the actuator.
- ✓ The reduction in natural frequency observed in experiment when actuators are placed in petri dish filled with oil, and subsequently inside the fluid channels is caused by an increase in the effective mass of the actuator.
- ✓ The numerical study using single degree of freedom model reveals that the mass of the actuator is negligible as compared to the added mass that the actuator is experiencing when it is placed in petri dish filled with oil or inside the fluid channels. In addition, the added mass is independent of actuator's thickness and elastic modulus.
- ✓ The numerical study using single degree of freedom model reveals that the added mass that the actuator is experiencing increases as the area of vibrating portion is increased, or as the distance between the actuator and membrane is decreased. The presence of silicon residues and support structure further increases added mass. The effect of support structure on the added mass is more pronounced as the distance between the actuator and membrane is increased.
- ✓ When the natural frequencies of the actuators in petri dish are matched by adjusting the area of the vibrating portion, the single degree of freedom model is able to predict natural

frequencies of the actuator in air fairly well. The relative error for actuator 1 is under 5%. For actuators 2 and 3 the model predicts natural frequencies of 99 and 103 kHz, while in the experiment they are above 100 kHz. However, when the model is used to predict natural frequency of the actuators inside the fluid channels, the resulting relative errors are 42, 18, and 75% for actuators 1, 2, and 3, respectively.

- ✓ When the stiff membrane and a spring are added to a single degree of freedom model to form a two-degrees of freedom model, and the first natural frequencies are matched by adjusting stiffness of the springs, the two-degree of freedom model predicts second natural frequency fairly well. The resulting relative errors are 10, 4, and 1% for actuators 1, 2, and 3 respectively.
- ✓ The two-degrees of freedom model predicts out of phase motion between the actuator and membrane at the lower frequency, and in phase motion at the higher frequency. The phase difference between the actuator and the point on the membrane above the actuator measured in the experiment is in agreement with prediction only for the actuator 3. For actuator 1 and 2 the trend is opposite (out of phase at lower frequency; in phase at higher frequency).
- ✓ Principal component analysis reveals that the vibration shapes of the membrane are much more complicated than the two-degrees of freedom model is capable to predict. Moreover, there is a nodal point above the actuator for most of the measurements in question.
- ✓ The numerical study using a full model reveals some similarities with the two degrees of freedom model, as well as with the experimental measurements. The phase behavior is similar to that predicted by the two degrees of freedom model. In particular, the motion of the actuator and the portion of the membrane above it starts out of phase, and switches

to be in phase at higher frequency. The vibration shape of the membrane as well as the location of nodal points can be matched to that in the experiment by adjusting its stiffness. Therefore, the discrepancy in phase behavior for actuator 1 and 2 can be attributed to the uncertainty in the location of the actuator relative to the nodal point on the membrane. It is also possible that the wiring was not consistent between the measurements from the actuator and membrane.

- ✓ The numerical study using a full model reveals that the presence of the actuator has very little effect on the dynamics of the fluid-membrane system. In particular, the changes to natural frequencies and mode shapes associated with the fluid-membrane system are very minor when actuator is introduced. This conclusion holds true if actuator is positioned farther or closer to the membrane, as well as when the membrane stiffness is reduced. In the context of cochlear dynamics, this result means that the introduction of the actuator into cochlear will not alter it functionality. Moreover, the surgeon does not need to worry about how far from the membrane the actuator needs to be placed, as long as its natural frequency is not reduced to the range of frequencies where the actuator is supposed to operate.

The numerical study can be extended to answer many questions that were not addressed in the current work. For example:

- ✓ The size of the cavity can have a significant impact on the added mass that actuator experiences. After the fixture was assembled, its measured width at both ends was 200 μm smaller than designed. Its height was not measured but it may deviate from the designed value as well. In addition to error introduced by the 3D printing process, the fixture was pressed during the assembly, which could increase an error. The sensitivity of the added mass on the height of the channel is unknown. The need for this study is enhanced by the fact that the size of the cochlear varies from person to person.

- ✓ In all numerical studies conducted in the current work, the actuator was aligned parallel to the membrane. Such alignment would be impossible to achieve during the surgery. What affect the misalignment between the actuator and membrane causes is unknown.
- ✓ The results of numerical study using the full model show that in some modes, the actuator deformation is negligible as compared to the deformation of the membrane. From the perspective of the vibration theory, the actuator is a nodal point in these modes. If the system is driven at the nodal point, the mode will not get excited. This may degrade the performance of a real cochlear. To avoid such problem, the optimal location of the actuator must be found using numerical study.
- ✓ Finally, the numerical study can be extended to provide a more useful insight into the physics of real cochlear by replacing aluminum membrane with the membrane that has more realistic properties.

BIBLIOGRAPHY

[1] E. De Boer and A. L. Nuttall, *Cochlear Mechanics, Tuning, Nonlinearity,* Oxford Handbook of Auditory Science: The Ear, DOI: 10.1093/oxfordhb/9780199233397.013.0005, 2012.

[2] E. De Boer, *Short Waves in Three-Dimensional Cochlea Models: Solution for a Block Model,* Hearing Research, Vol. 4, pp. 53-77, 1981.

[3] A. A. Parthasarathi, K. Grosh, A. L. Nuttall, *Three-Dimensional Numerical Modeling for Global cochlear Dynamics,* J. Acoust. Soc. Am., Vol. 107 (1), pp. 474-485, 2000

[4] S. Ramamoorthy, N. V. Deo, and K. Grosh, 2007, *A mechano-electro-acoustical model for the cochlea: Response to acoustic stimuli,* J. Acoust. Soc. Am., Vol. 121, pp. 2758–2773.

[5] Y.J. Yoon, S. Puria, and C. R. Steele, 2007, *Intracochlear pressure and derived quantities from a three-dimensional model,* J. Acoust. Soc. Am., Vol. 122, pp. 952-966.

[6] R. Z. Gan, B. P. Reeves, and X. Wang, 2007, *Modeling of Sound Transmission from Ear Channel to Cochlea,* Annals of Biomedical Engineering, Vol. 35, pp. 2180–2195.

[7] B. S. Wilson, D. T. Lawson, J. M. Muller, R. S. Tyler, and J. Kiefer, *Cochlear implants: Some likely next steps,* Annual Review of Biomedical Engineering, vol. 5, pp. 207-249, 2003.

[8] B. J. Gantz, C. W. Turner, K. E. Gfeller, and L. M. W., *Preservation of Hearing in Cochlear Implant Surgery: Advantages of Combined Electrical and Acoustical Speech Processing,* The Laryngoscope, vol. 115, pp. 796-802, 2005.

[9] M. F. Dorman and R. H. Gifford, *Combining acoustic and electric stimulation in the service of speech recognition,* International Journal of Audiology, vol. 49, pp. 912-919, 2010.

[10] T. Rader, Y. Adel, H. Fastl, and U. Baumann, *Speech Perception with Combined Electric-Acoustic Stimulation: A Simulation and Model Comparison,* Ear and Hearing, Vol. 36, pp. E314-E325, 2015.

[11] S. Helbig, Y. Adel, T. Rader, T. Stoever, and U. Baumann, *Long-Term Hearing Preservation Outcomes after Cochlear Implantation for Electric-Acoustic Stimulation,* Otology and Neurotology, Vol. 37 (9), pp. E353-E359, 2016.

[12] Chuan Luo, G. Z. Cao, and I. Y. Shen, *Development of a Lead-Zirconate-Titanate (PZT) Thin-Film Microactuator Probe for Intracochlear Applications,* Sensors and Actuators A—Physical, Vol. 201, pp. 1-9, 2013:

[13] Chuan Luo, Irina Omelchenko, Robert Manson, Carol Robbins, Elizabeth C. Oesterle, G. Z. Cao, I. Y. Shen, Clifford R. Hume, *Direct Intracochlear Acoustic Stimulation using a PZT Microactuator*, Trends in Hearing, Vol. 19, pp.1-14, 2015.

[14] C. Luo, W. C. Tai, C. W. Yang, G. Z. Cao, and I. Y. Shen, *Effect of Added Mass on Lead-Zirconate-Titanate (PZT) Thin-Film Microactuators in Aqueous Environments,* ASME Journal of Vibration and Acoustics, Vol. 138, pp. 061015-1 to 061015-10, DOI: 10.1115/1.4034613, 2016.

[15] Rask-Andersen, Helge, et al. *Human Cochlea: Anatomical Characteristics and Their Relevance for Cochlear Implantation.* Anatomical Record (Hoboken, N.J. : 2007), vol. 295, no. 11, 2012, pp. 1791–1811.

[16] Shin, Kang-Jae, et al. *Quantitative Analysis of the Cochlea Using Three-Dimensional Reconstruction Based on Microcomputed Tomographic Images.* Anatomical Record (Hoboken, N.J. : 2007), vol. 296, no. 7, 2013, pp. 1083–1088.

[17] Liu, Wei, et al. "Macromolecular Organization and Fine Structure of the Human Basilar Membrane - RELEVANCE for Cochlear Implantation." Cell and Tissue Research, vol. 360, no. 2, 2015, pp. 245–262.

[18] Marrero, V. A., Borca-Tasciuc, D., & Tichy, J. *On squeeze film damping in microsystems,* ASME Journal of Tribology, Vol. 132(3), pp. 1-6, 2010.

[19] Langlois, W. (1962). *Isothermal squeeze films*. Quarterly of Applied Mathematics, 20(2), 131-150.

[20] Andrews, M., Harris, I., & Turner, G. (1993). *A comparison of squeeze-film theory with measurements on a microstructure.* Sensors & Actuators: A. Physical, 36(1), 79-87.

[21] Bao, M., & Yang, H. (2007). *Squeeze film air damping in MEMS*. Sensors & Actuators: A. Physical, 136(1), 3-27.

[22] Blech, J. (1983). *On Isothermal Squeeze Films.* Journal of Lubrication Technology, 105(4), 615-620.

[23] Pratap, R. K., Mohite, S., & Pandey, A. (2007). *Squeeze film effects in MEMS devices*. Journal of the Indian Institute of Science, 87(1), 75-94.

[24] Naik, T., Longmire, E., & Mantell, S. (2003). *Dynamic response of a cantilever in liquid near a solid wall*. Sensors & Actuators: A. Physical, 102(3), 240-254.

[25] Harrison, C., Tavernier, E., Vancauwenberghe, O., Donzier, E., Hsu, K., Goodwin, A., Mercier, B. (2007). *On the response of a resonating plate in a liquid near a solid wall.* Sensors & Actuators: A. Physical, 134(2), 414-426.

[26] Tichy, J., & Modest, M. (1978). *Squeeze film flow between arbitrary two-dimensional surfaces subject to normal oscillations.* TRANS. ASME SER. F, J. LUBR. TECHNOL., 100(2), 316-322.

[27] Timo Veijola. (2004). *Compact models for squeezed-film dampers with inertial and rarefied gas effects.* Journal of Micromechanics and Microengineering, 14(7), 1109-1118.

[28] J.-G. Tseng; J. A. Wickert, *Split Vibration Modes in Acoustically-Coupled Disk Stacks,* ASME Journal of Vibration and Acoustics, Vol, 120(1), pp. 234-239, 1998

[29] Jeong, Kyeong-Hoon. *Free Vibration of Two Identical Circular Plates Coupled with Bounded Fluid.* Journal of Sound and Vibration, vol. 260, no. 4, 2003, pp. 653–670.

[30] Motley, Michael R, et al. *Free Surface and Solid Boundary Effects on the Free Vibration of Cantilevered Composite Plates.* Composite Structures, vol. 96, 2013, pp. 365–375.

[31] Howard, Carl, and Cazzolato, Benjamin. *Acoustic Analyses Using Matlab and Ansys.* CRC Press, 2015.

[32] Rodriguez, C.G, et al. *Capability of Structural–Acoustical FSI Numerical Model to Predict Natural Frequencies of Submerged Structures with Nearby Rigid Surfaces*. Computers & Fluids, vol. 64, 2012, pp. 117–126.

[33] Logan, Daryl L. *A First Course in the Finite Element Method.* 5th ed., Cengage Learning, 2012.

[34] Yadykin, Y, et al. *The Added Mass of a Flexible Plate Oscillating in a Fluid.* Journal of Fluids and Structures, vol. 17, no. 1, 2003, pp. 115–123.

[35] Meirovitch, Leonard. *Fundamentals of Vibrations*. McGraw-Hill, 2001.

[36] Ewins, D. J. *Modal Testing : Theory and Practice*. Research Studies Press ; Wiley, 1984.

[37] Kutz, Jose Nathan. *Data-Driven Modeling & Scientific Computation : Methods for Complex Systems & Big Data.* First ed., Oxford University Press, 2013.

[38] Hamery, Pascal, et al. *Acoustic Fields in Trapezoidal Cavities.* Acta Acustica United with Acustica, vol. 83, no. 1, 1997, pp. 13–18.

[39] Bossio, Matias, et al. *Numerical Study on the Influence of Acoustic Natural Frequencies on the Dynamic Behaviour of Submerged and Confined Disk-like Structures.* Journal of Fluids and Structures, vol. 73, 2017, pp. 53–69.

[40] Kack, Britta. *Aluminium foil at multiple length scales: mechanical tests and numerical simulations in Abaqus*. 2015.

APPENDIX A

MEASUREMENTS FROM ACTUATOR 1

Table A1. Coordinates of measurement points along the length of the membrane for Actuator 1

Point #	1	2	3	4	5	6	7	8	9	10	11
X (mm)	0.78	1.95	3.06	4.13	5	5.94	7.11	8.1	9.02	10	11.05
Point #	12	13	14	15	16	17	18	19	20	21	22
X (mm)	11.99	12.98	14	15	16	17	18	19	19.97	21	22.04
Point #	23	24	25	26	27	28	29				
X (mm)	22.9	23.99	24.39	25.99	26.98	28.03	28.87				

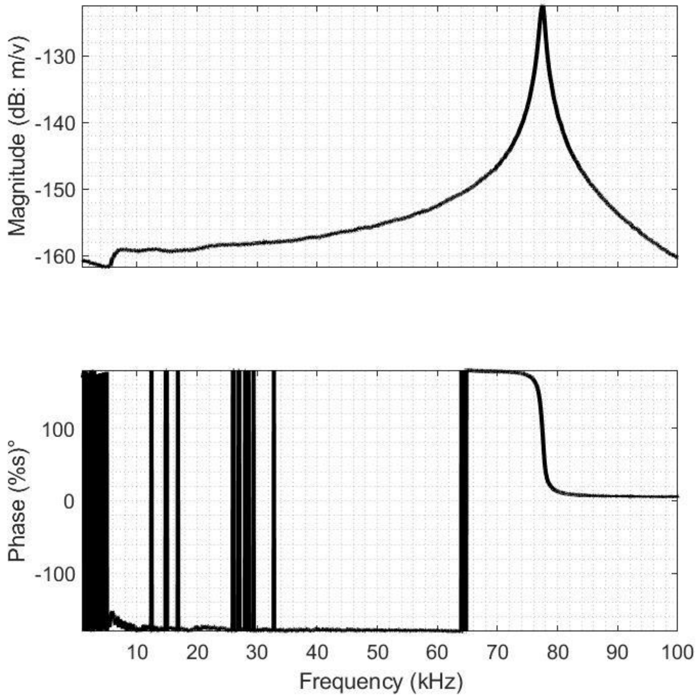

Figure A1. Frequency response function of actuator 1 in air

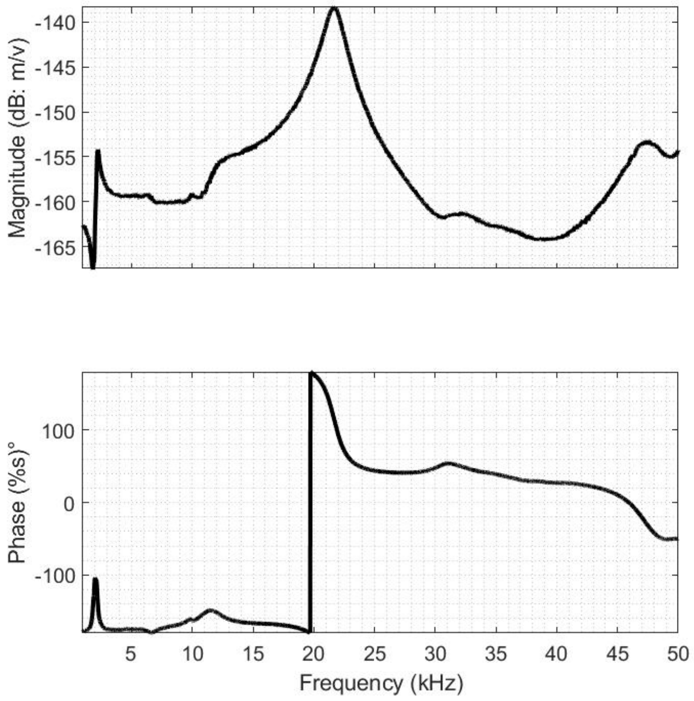

Figure A2. Frequency response function of actuator 1 in oil

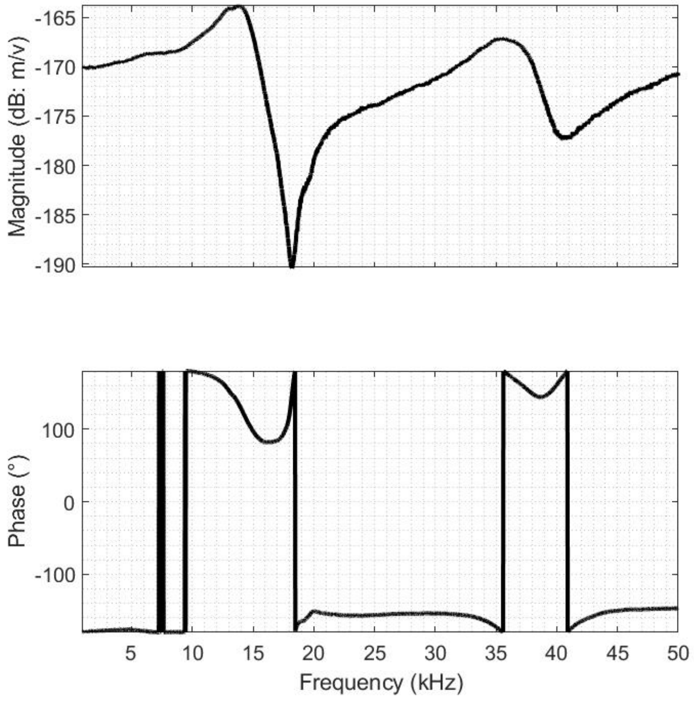

Figure A3. Frequency response function of actuator 1 in fluid channels

Figure A4. Frequency response function of the aluminum membrane for actuator 1

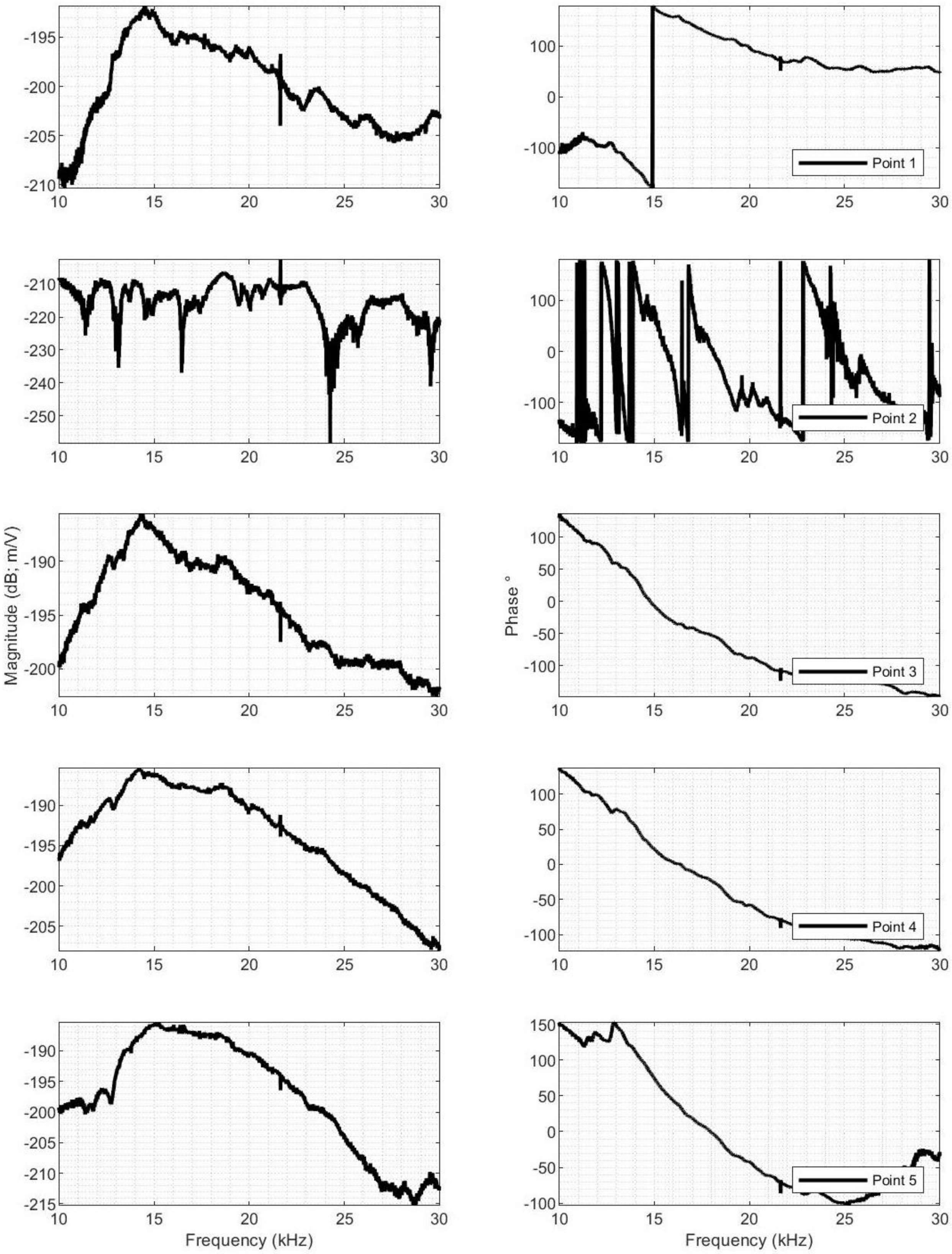
Magnitude (dB; m/V)
Phase °
Frequency (kHz)
Frequency (kHz)
Point 1
Point 2
Point 3
Point 4
Point 5
-195
-200
-205
-210
-220
-230
-240
-250
-190
-215
100
50
0
-50
-100
150
10
15
20
25
30

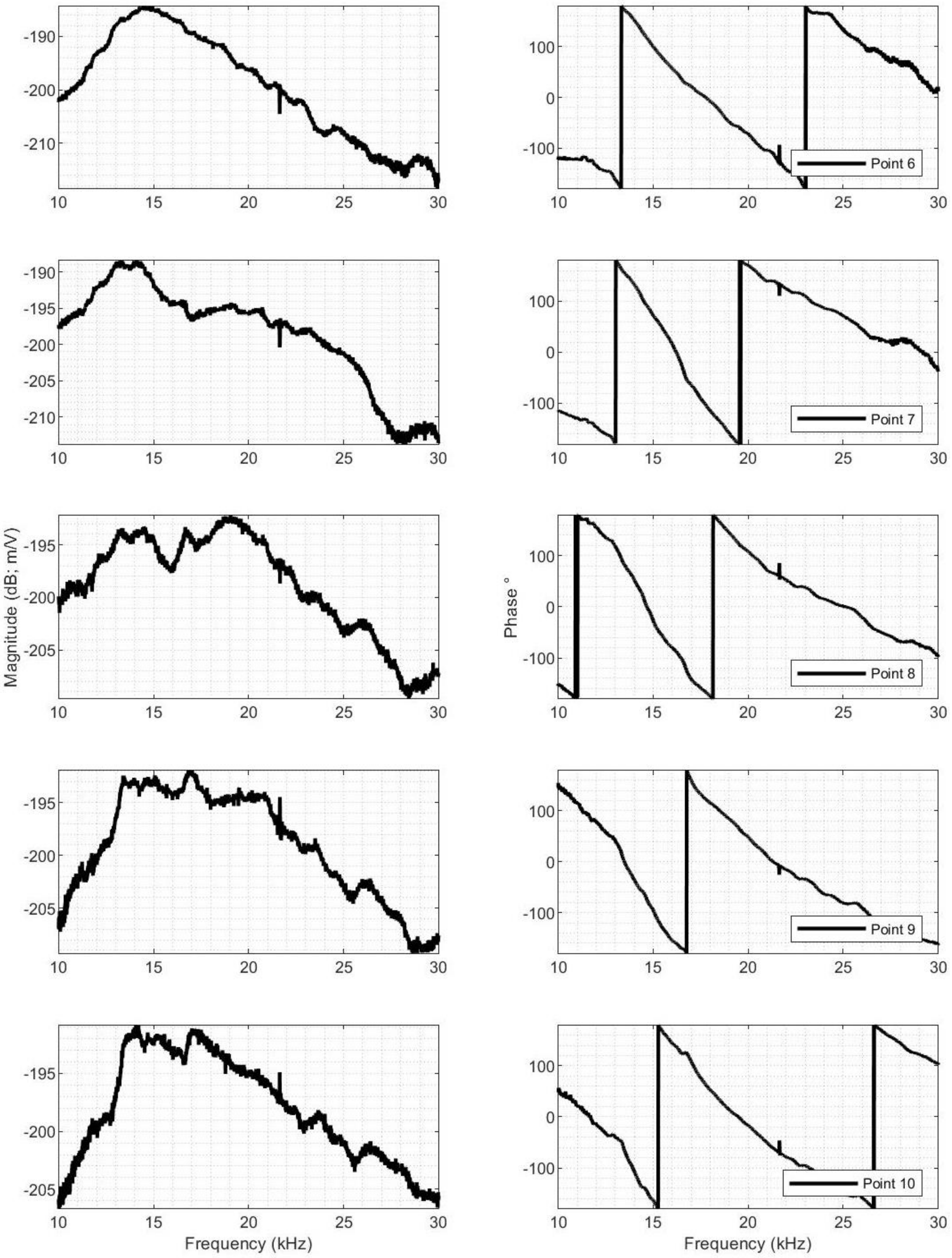
Magnitude (dB; m/V)
Phase °
Frequency (kHz)
Frequency (kHz)
Point 6
Point 7
Point 8
Point 9
Point 10
-190
-200
-210
-195
-205
100
0
-100
10
15
20
25
30

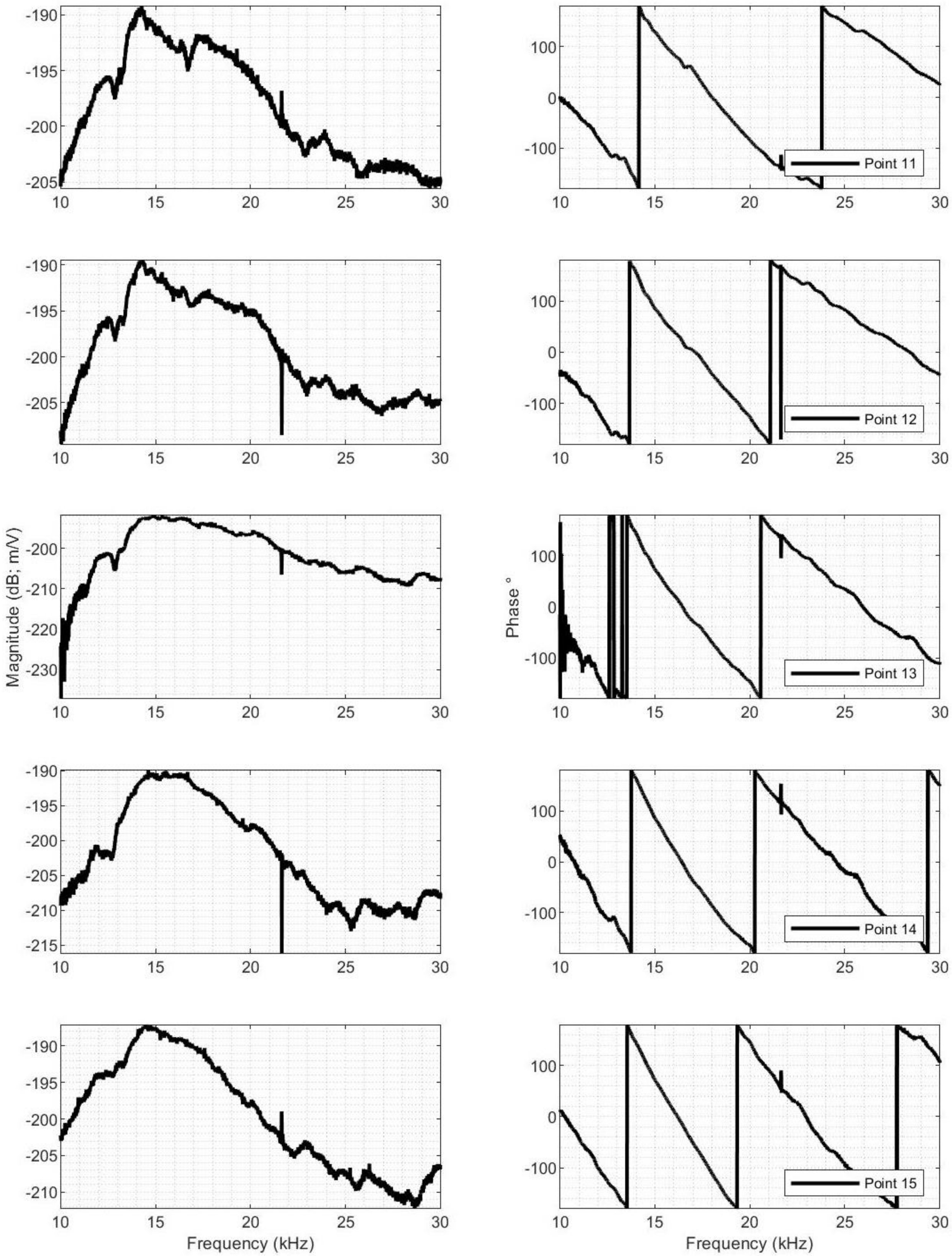
Magnitude (dB; m/V)
Phase °
Frequency (kHz)
Point 11
Point 12
Point 13
Point 14
Point 15
-190
-195
-200
-205
-210
-215
-220
-230
100
0
-100
10
15
20
25
30

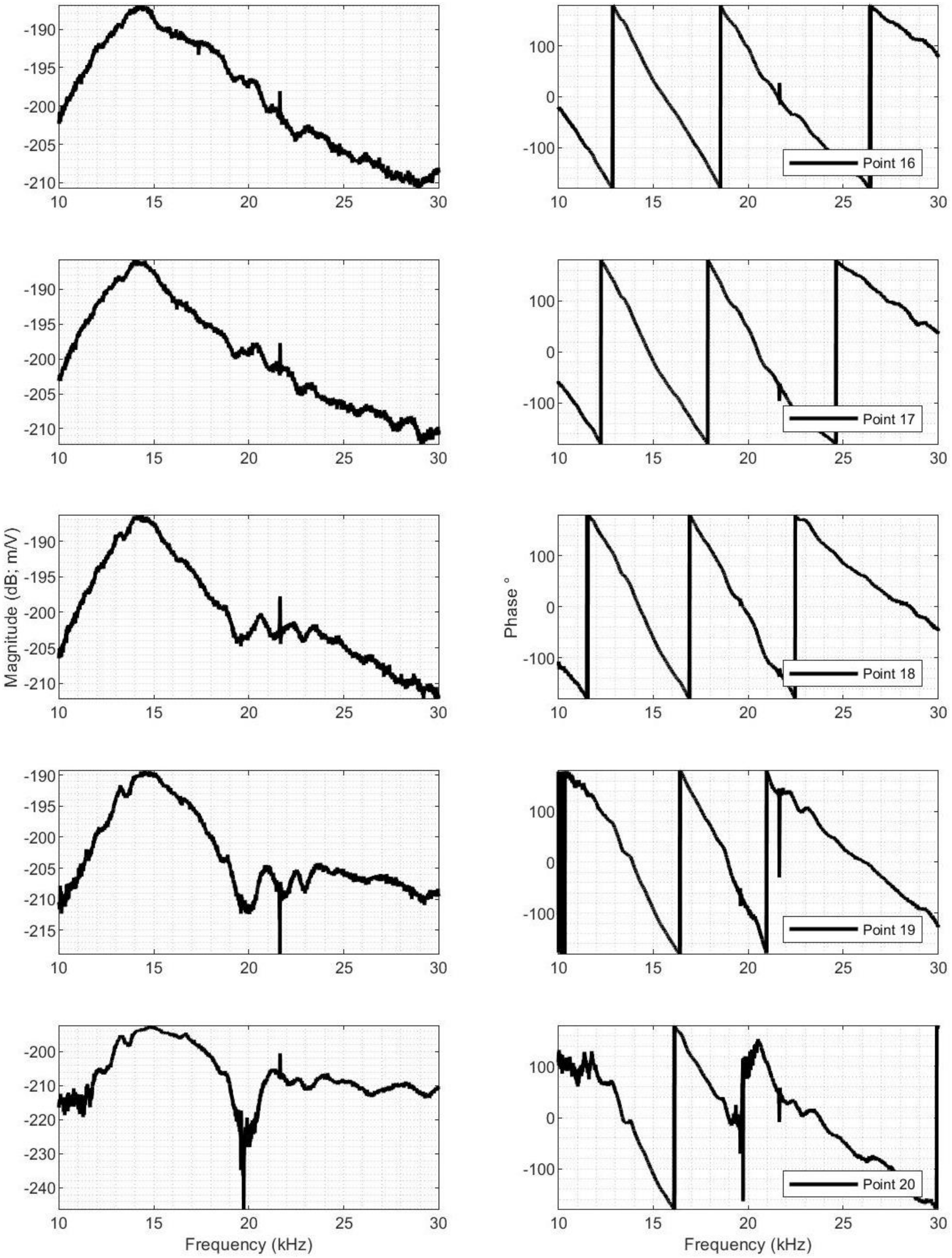
Magnitude (dB; m/V)
Phase °
Point 16
Point 17
Point 18
Point 19
Point 20
-190
-195
-200
-205
-210
-215
-220
-230
-240
100
0
-100
10
15
20
25
30
Frequency (kHz)
Frequency (kHz)

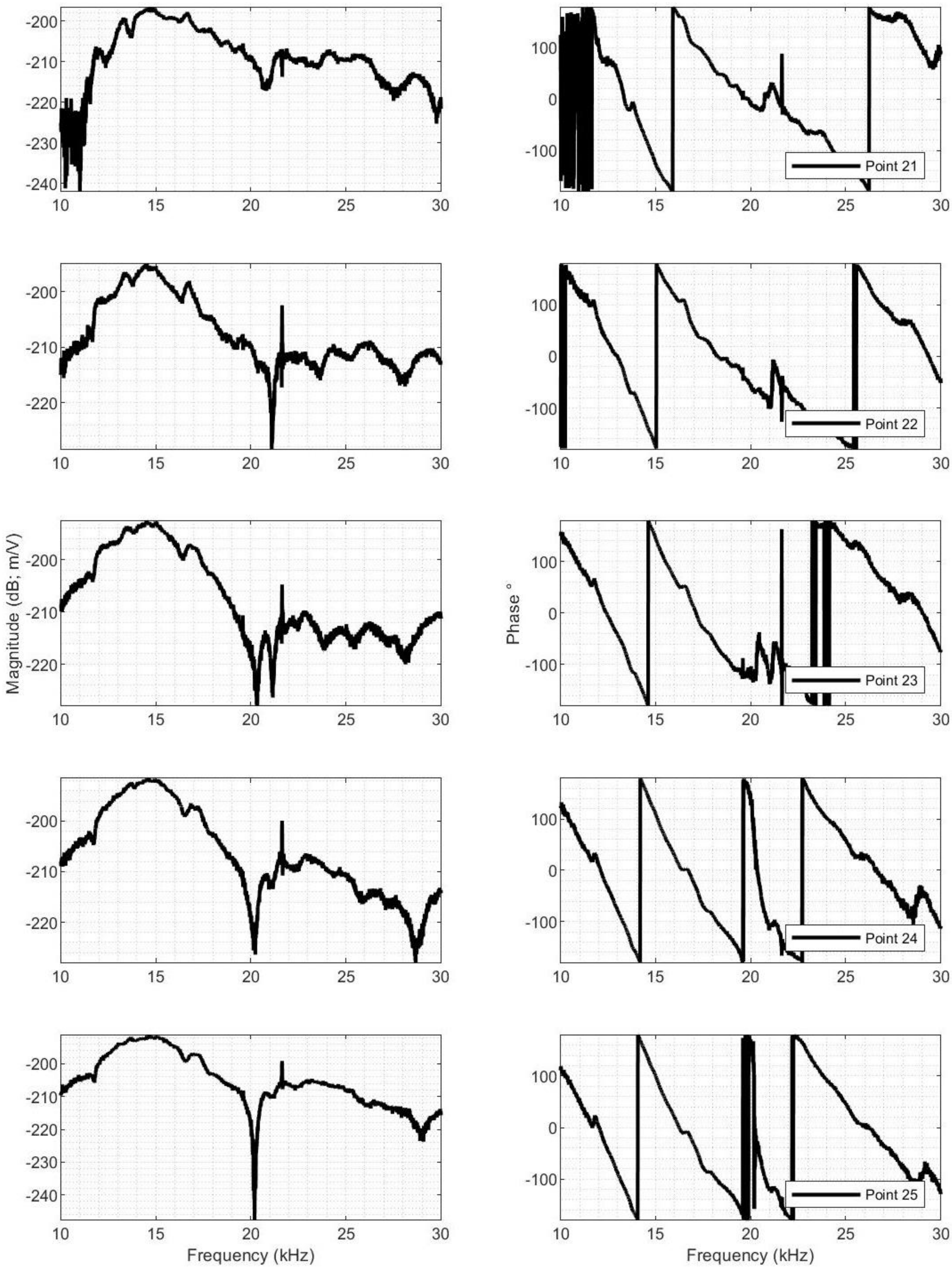
Magnitude (dB; m/V)
Phase °
Frequency (kHz)
Frequency (kHz)
Point 21
Point 22
Point 23
Point 24
Point 25
-200
-210
-220
-230
-240
100
0
-100
10
15
20
25
30

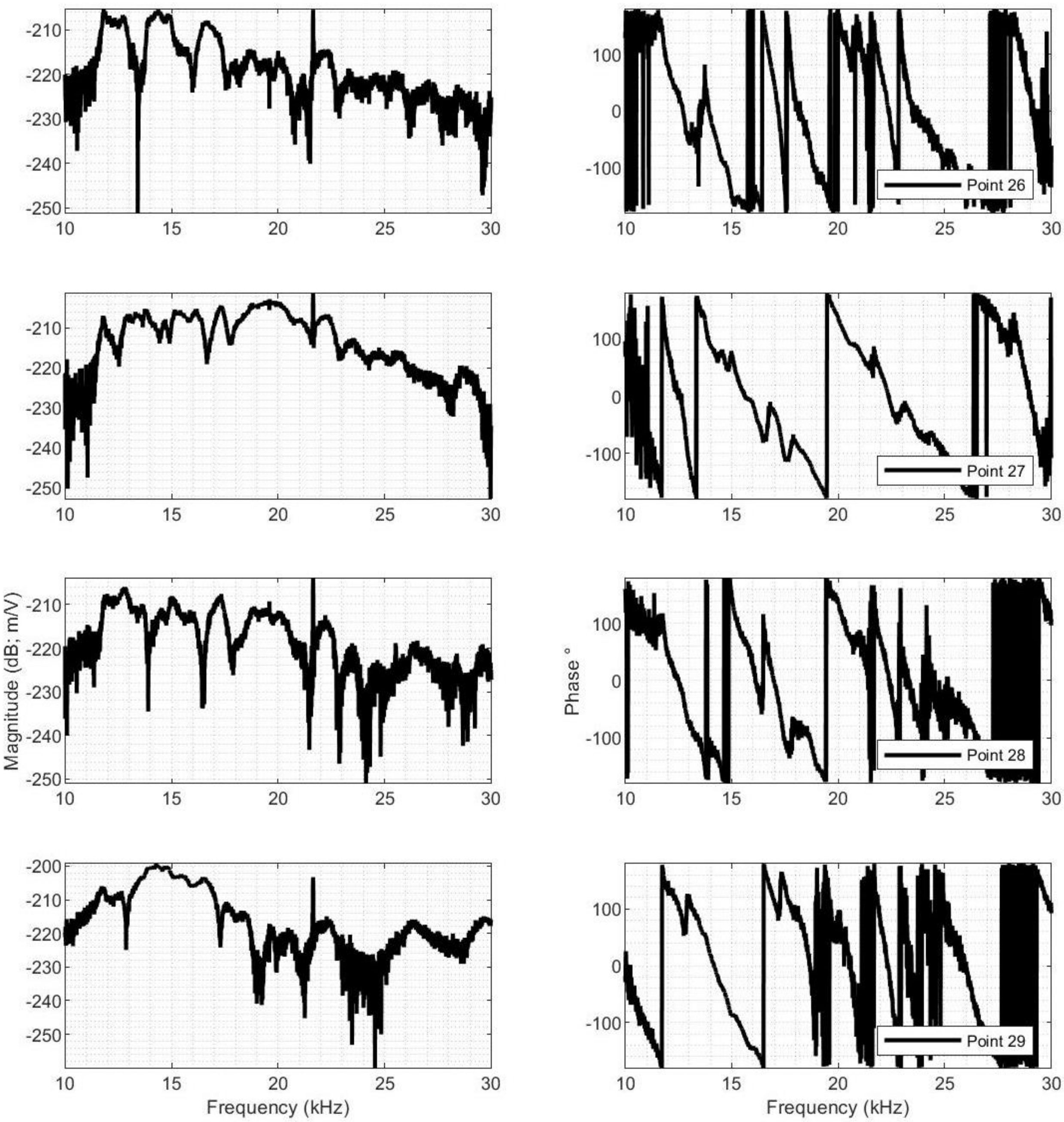
Magnitude (dB; m/V)
Phase °
Frequency (kHz)
Frequency (kHz)
-200
-210
-220
-230
-240
-250
100
0
-100
10
15
20
25
30
Point 26
Point 27
Point 28
Point 29

APPENDIX B

MEASUREMENTS FROM ACTUATOR 2

Table B1. Coordinates of measurement points along the length of the membrane for Actuator 2

Point #	1	2	3	4	5	6	7	8	9	10	11
X (mm)	0.5	1	2	3	4	5	6	7	8	9	10
Point #	12	13	14	15	16	17	18	19	20	21	22
X (mm)	10	11	12	13	14	15.1	16	17	18	19	20
Point #	23	24	25	26	27	28	29	30	31		
X (mm)	22	23	23.54	24.9	26	27.03	28	29	29.45		

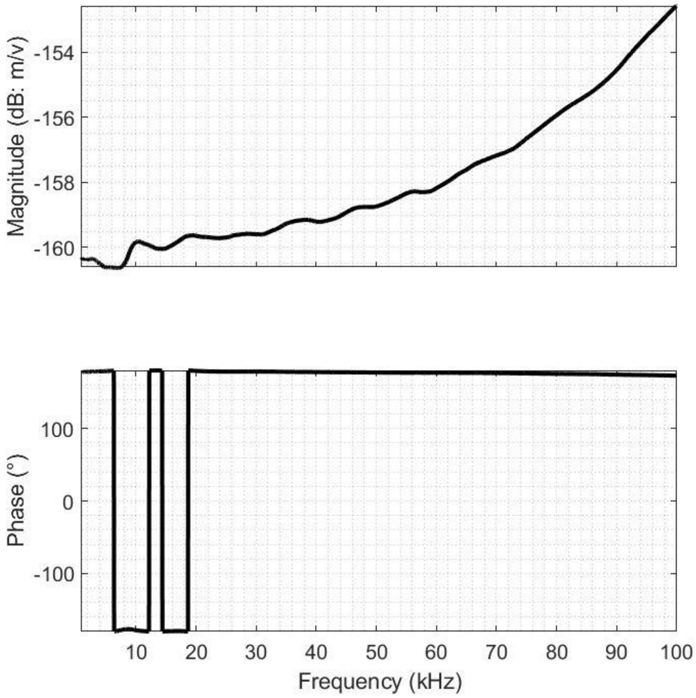

Figure B1. Frequency response function of actuator 2 in air

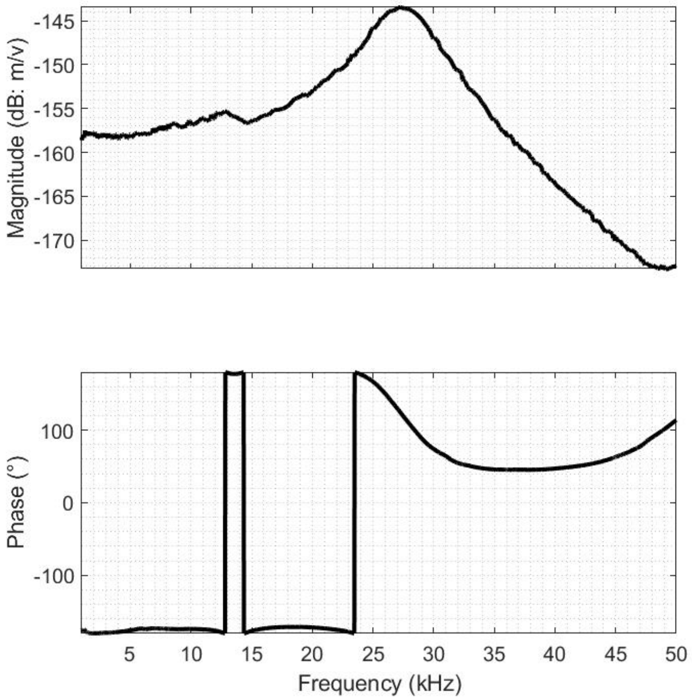

Figure B2. Frequency response function of actuator 2 in oil

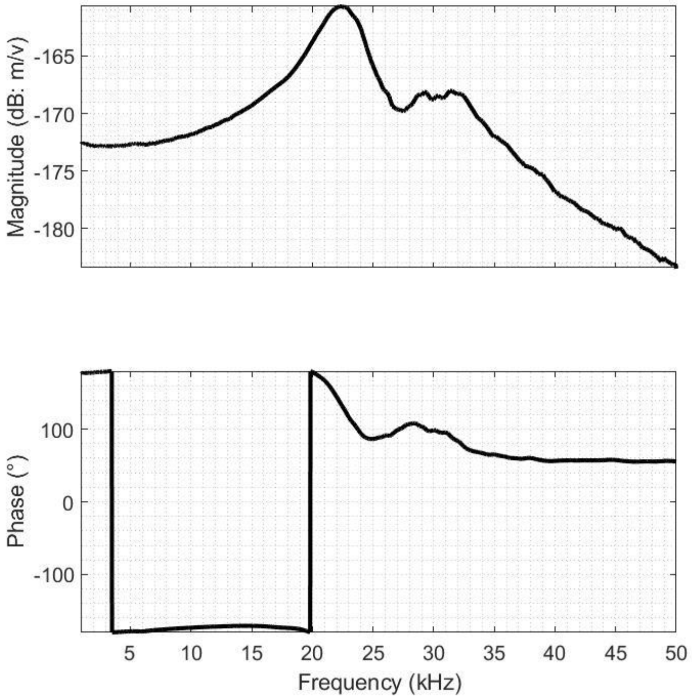

Figure B3. Frequency response function of actuator 2 in fluid channels

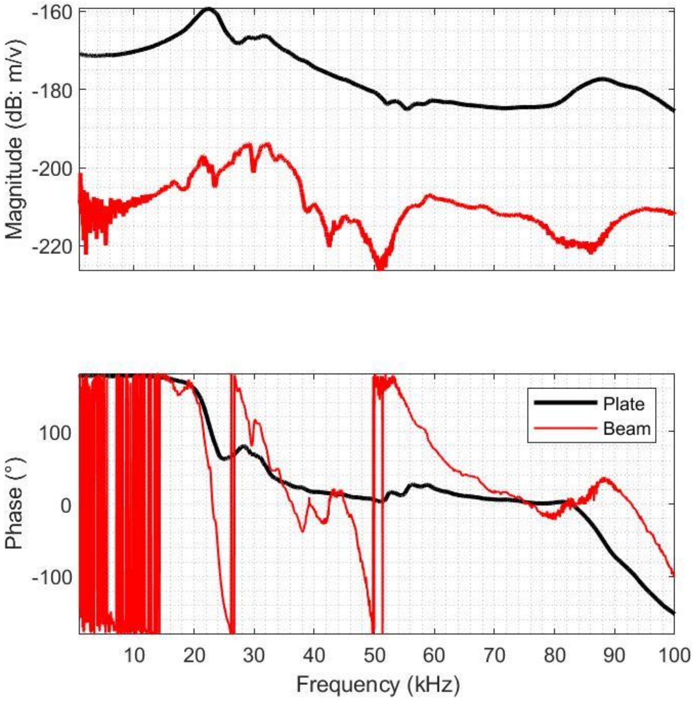

Figure B4. Frequency response functions of the actuator’s beam and plate portion inside the fluid channels for actuator 2

Figure B5. Frequency response function of the aluminum membrane for actuator 2

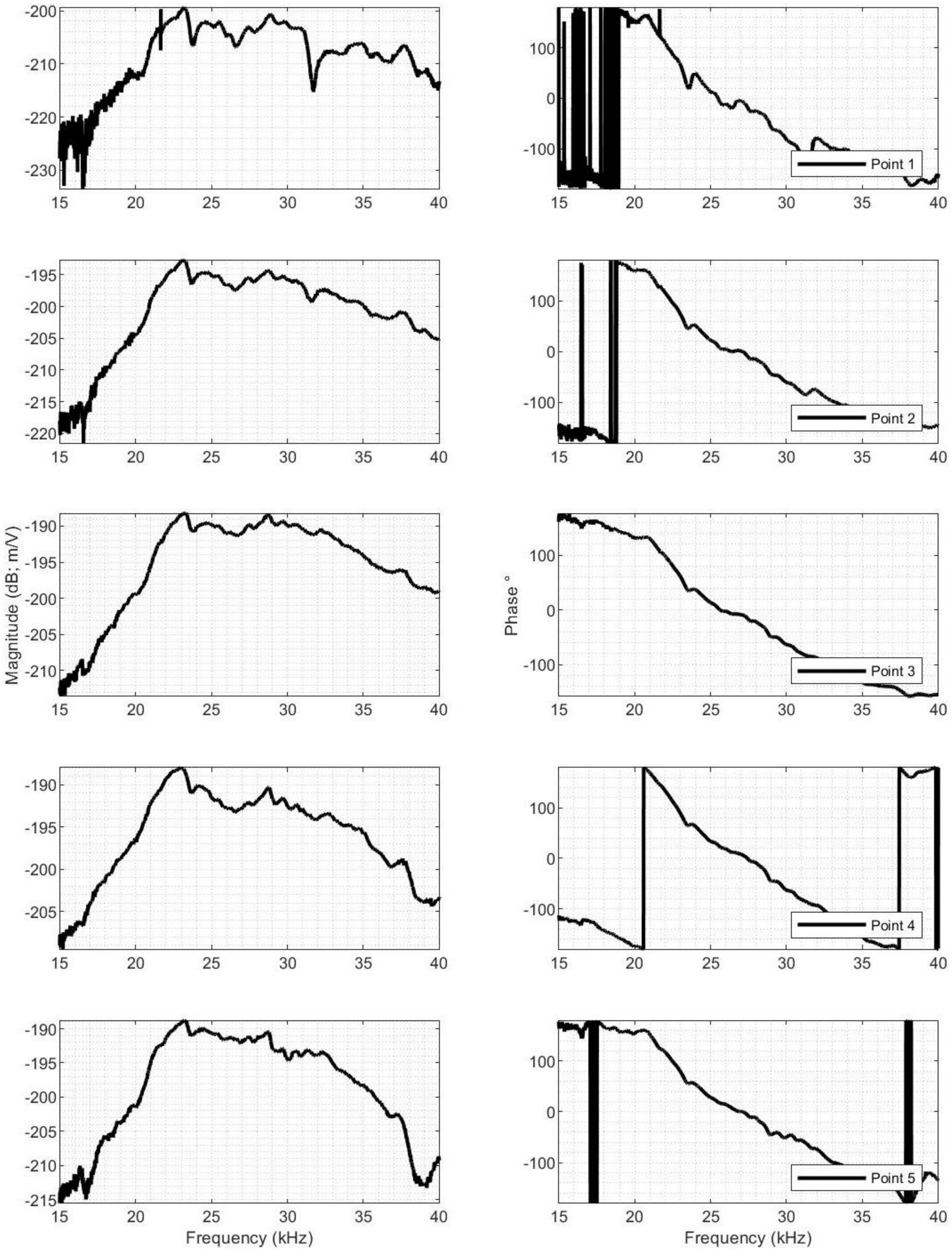
-200
-210
-220
-230
-195
-200
-205
-210
-215
-220
-190
-195
-200
-205
-210
-190
-195
-200
-205
-190
-195
-200
-205
-210
-215
Magnitude (dB; m/V)
100
0
-100
Phase °
Point 1
Point 2
Point 3
Point 4
Point 5
15
20
25
30
35
40
Frequency (kHz)
Frequency (kHz)

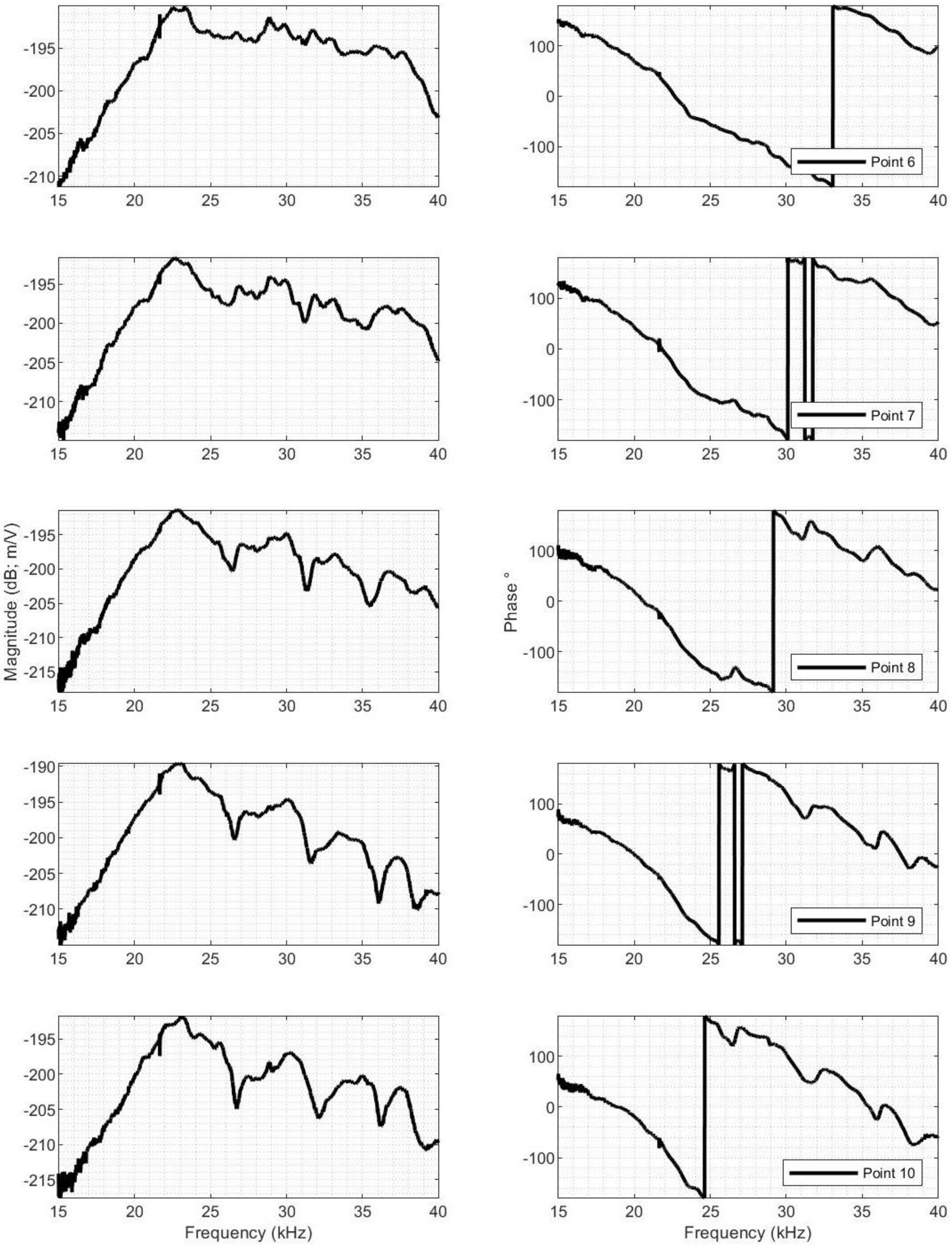
Magnitude (dB; m/V)
Phase °
Frequency (kHz)
Frequency (kHz)
15
20
25
30
35
40
-190
-195
-200
-205
-210
-215
100
0
-100
Point 6
Point 7
Point 8
Point 9
Point 10

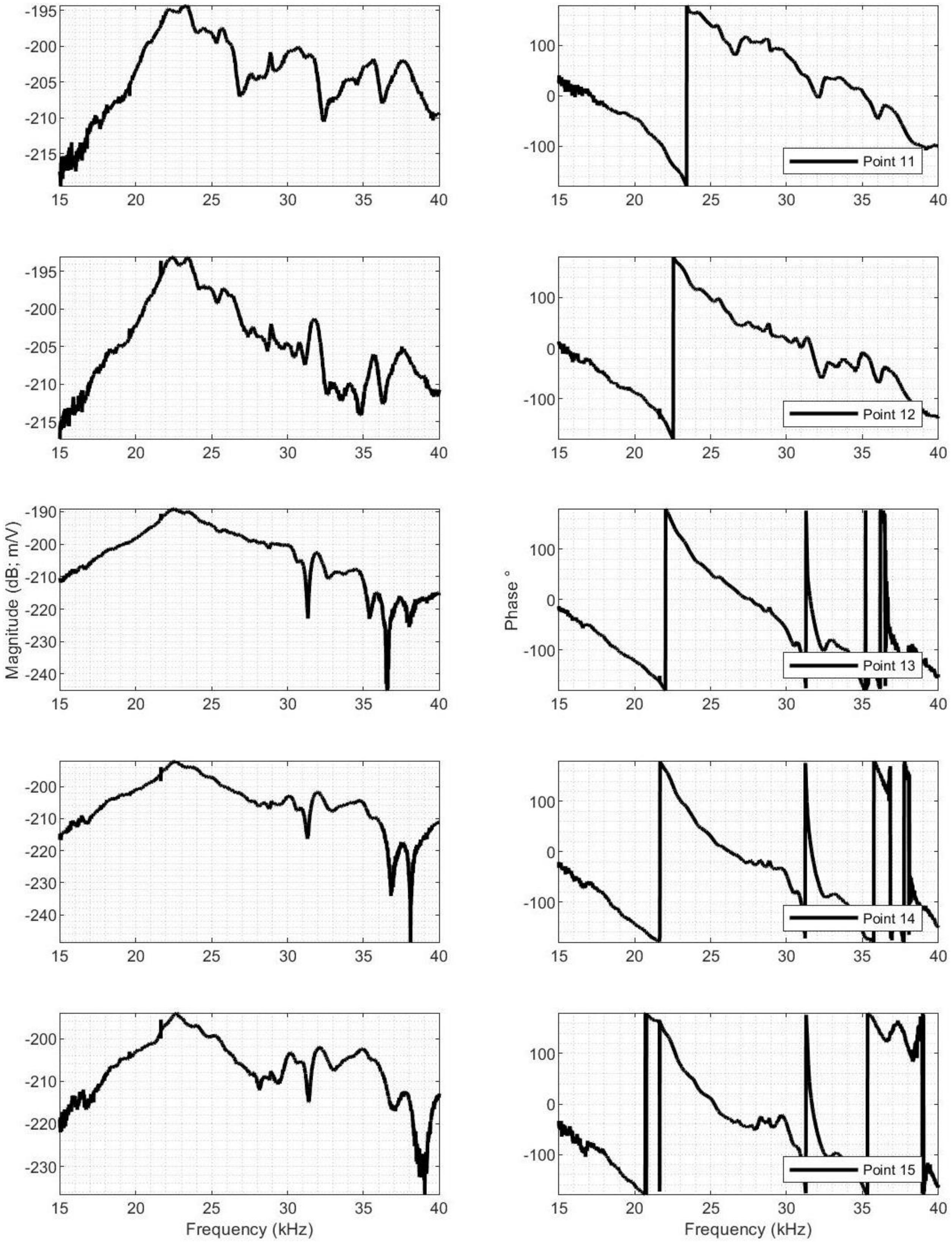
Magnitude (dB; m/V)
Phase °
Frequency (kHz)
Frequency (kHz)
15
20
25
30
35
40
-195
-200
-205
-210
-215
-190
-220
-230
-240
100
0
-100
Point 11
Point 12
Point 13
Point 14
Point 15

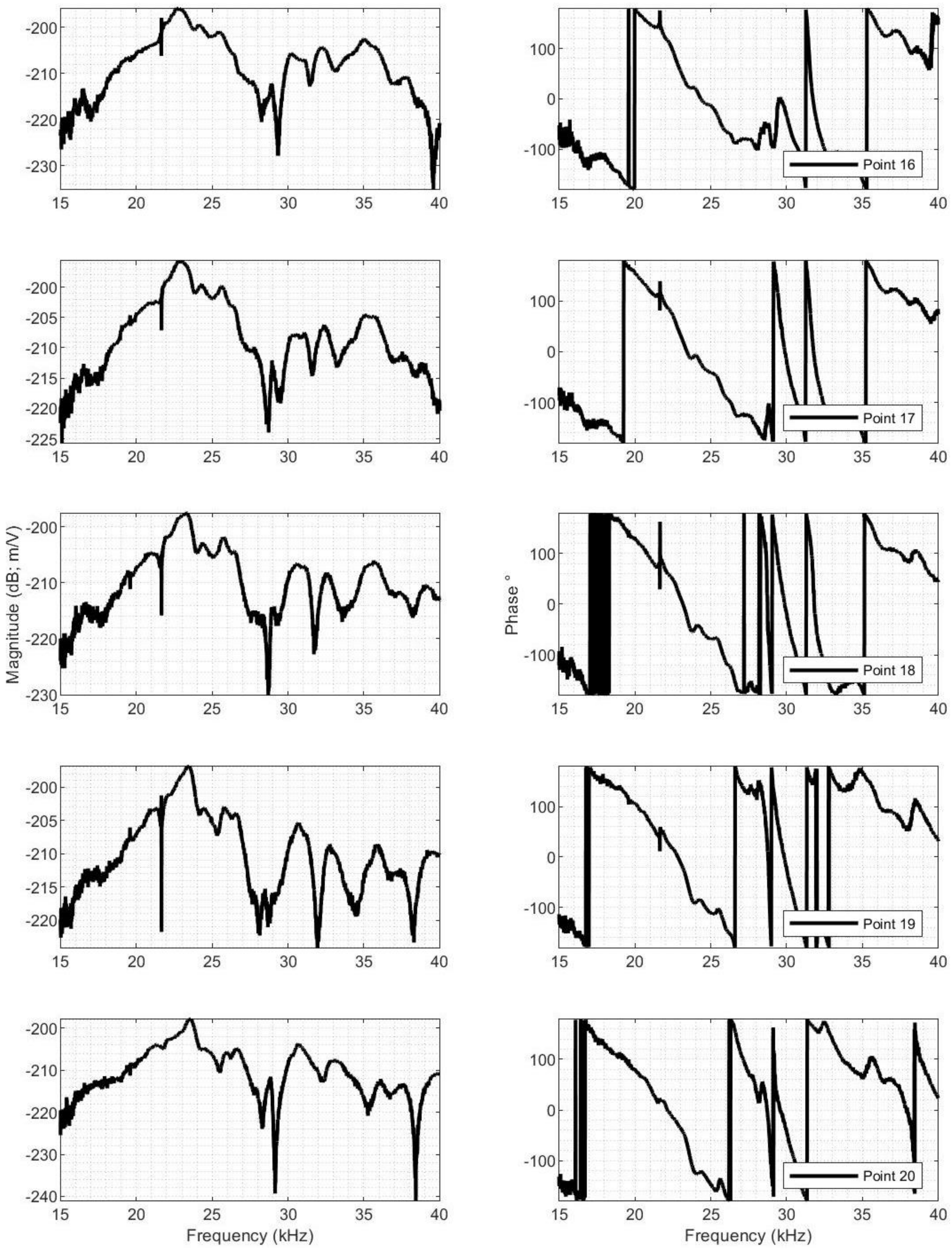
Magnitude (dB; m/V)
Phase °
Frequency (kHz)
15
20
25
30
35
40
-200
-205
-210
-215
-220
-225
-230
-240
100
0
-100
Point 16
Point 17
Point 18
Point 19
Point 20

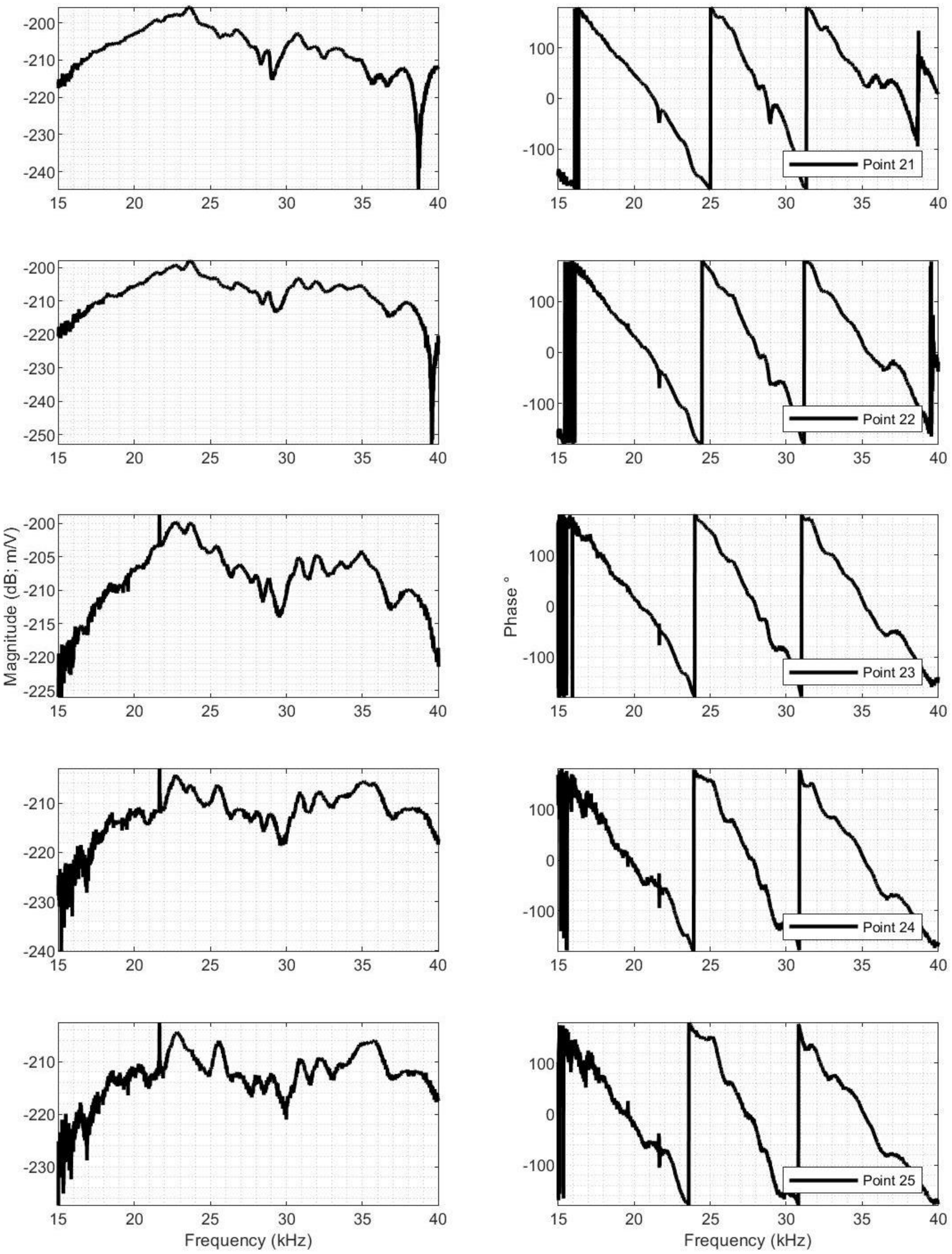
-200
-210
-220
-230
-240
-250
-205
-215
-225
Magnitude (dB; m/V)
100
0
-100
Phase °
15
20
25
30
35
40
Frequency (kHz)
Point 21
Point 22
Point 23
Point 24
Point 25

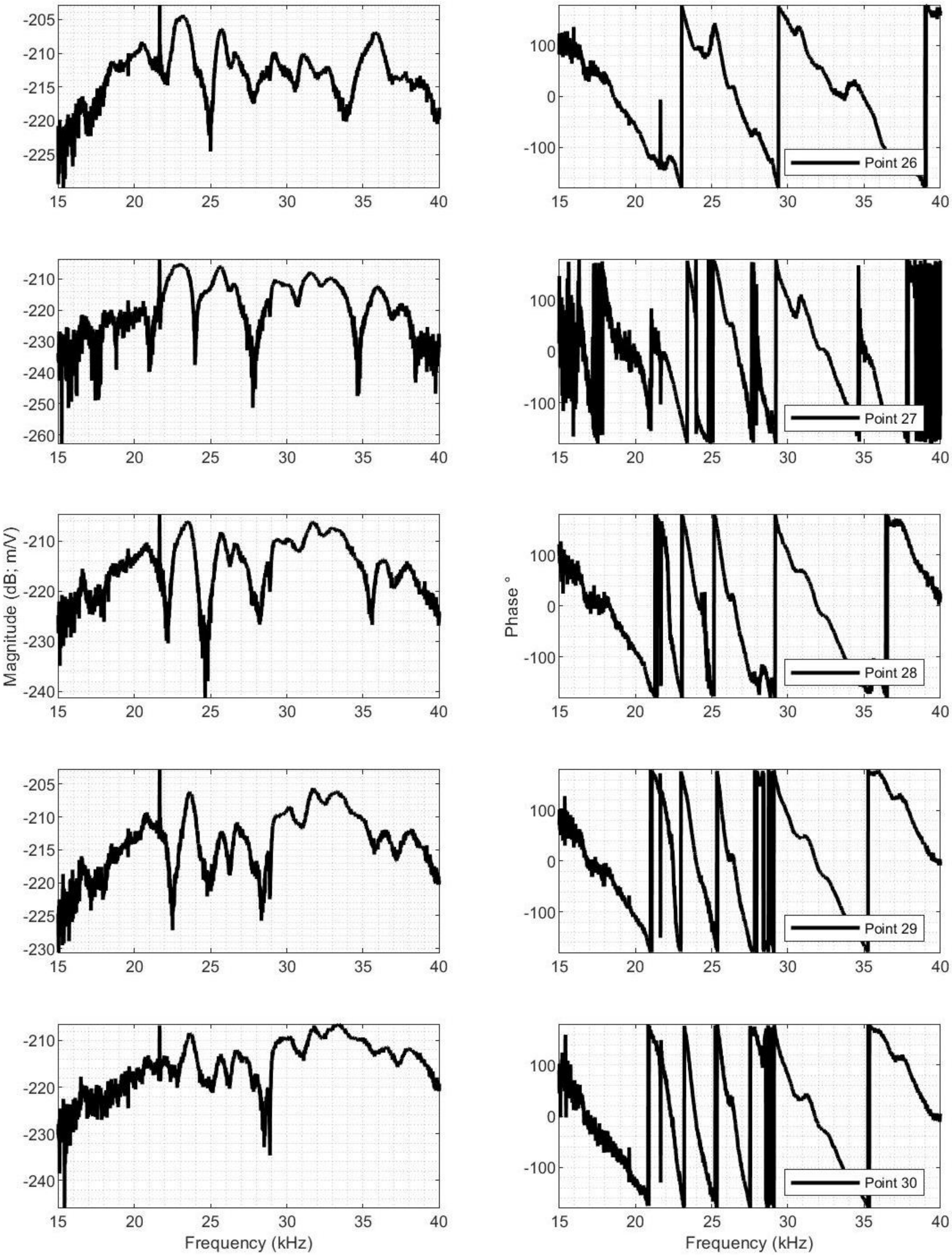
Magnitude (dB; m/V)
Phase °
Point 26
Point 27
Point 28
Point 29
Point 30
-205
-210
-215
-220
-225
-230
-240
-250
-260
100
0
-100
15
20
25
30
35
40
Frequency (kHz)
Frequency (kHz)

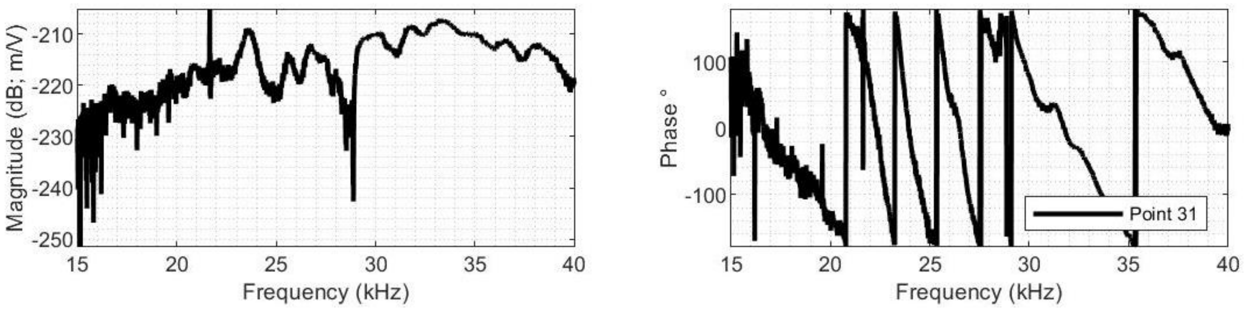
Magnitude (dB; m/V)
-210
-220
-230
-240
-250
15
20
25
30
35
40
Frequency (kHz)
Phase °
100
0
-100
15
20
25
30
35
40
Frequency (kHz)
Point 31

APPENDIX C

MEASUREMENTS FROM ACTUATOR 3

Table C1. Coordinates of measurement points along the length of the membrane for Actuator 3

Point #	1	2	3	4	5	6	7	8	9	10	11
X (mm)	0.5	1	2	3.02	4.03	5.02	6	6.88	8.07	9	9.96
Point #	12	13	14	15	16	17	18	19	20	21	22
X (mm)	9.96	11	11.97	13	14	15.1	16	17.02	18	19.05	20
Point #	23	24	25	26	27	28	29	30	31		
X (mm)	22.05	23.02	23.47	25.05	26	27	28.02	28.88	29.5		

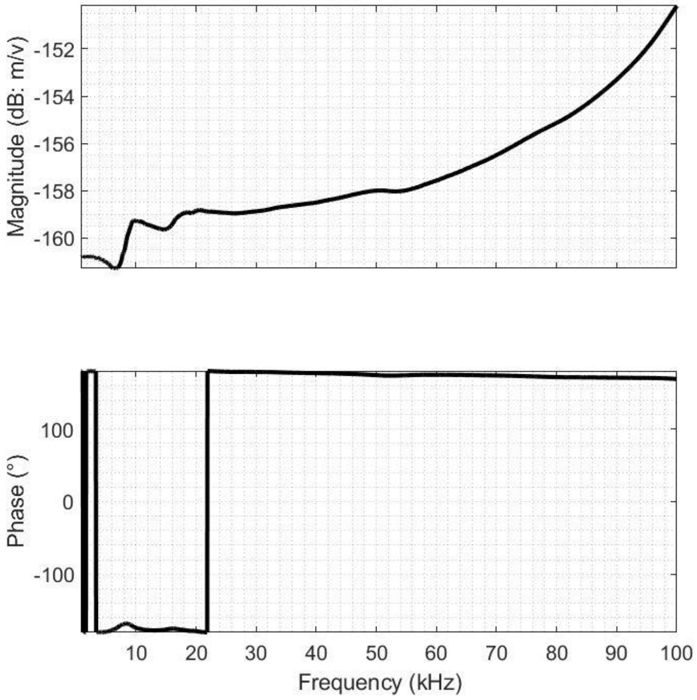

Figure C1. Frequency response function of actuator 3 in air

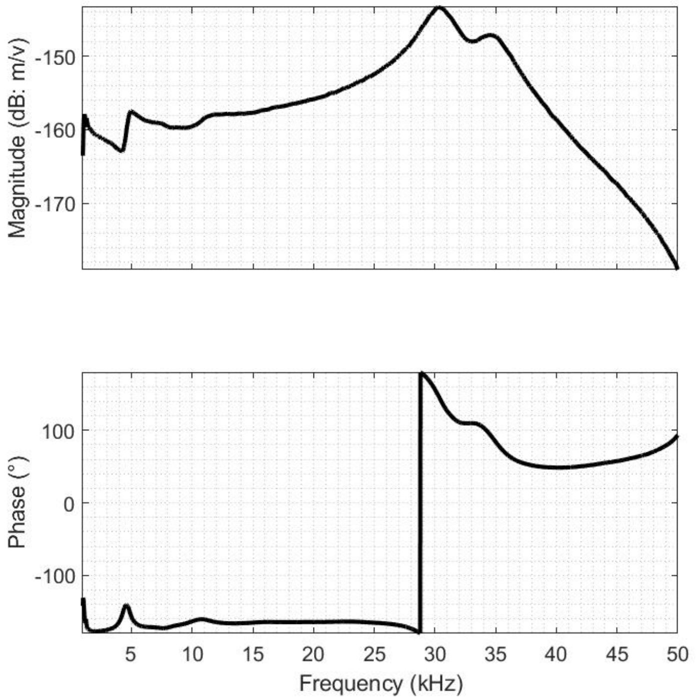

Figure C2. Frequency response function of actuator 3 in oil

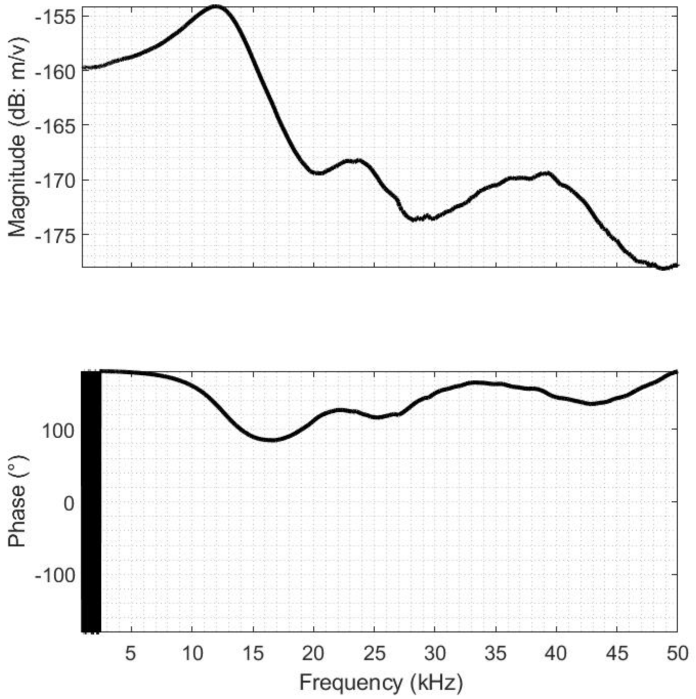

Figure C3. Frequency response function of actuator 3 in fluid channels

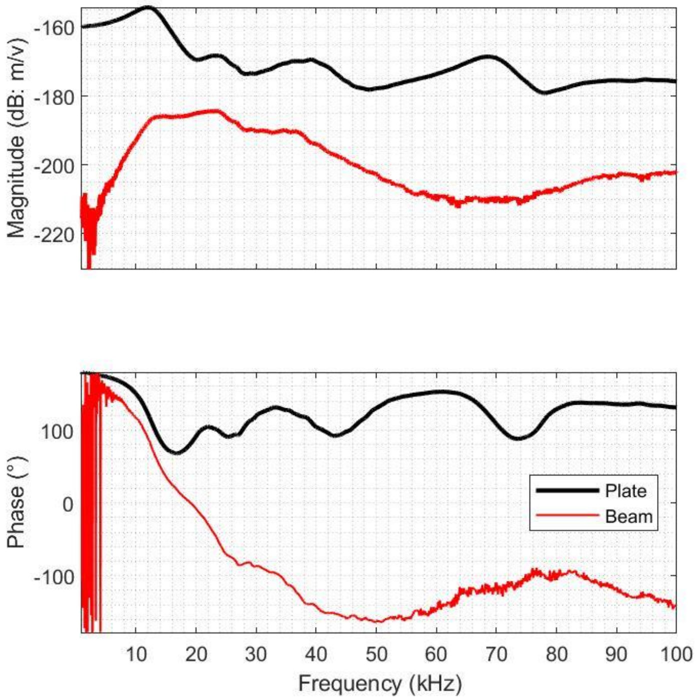

Figure C4. Frequency response functions of the actuator’s beam and plate portion inside the fluid channels for actuator 3

Figure C5. Frequency response function of the aluminum membrane for actuator 3

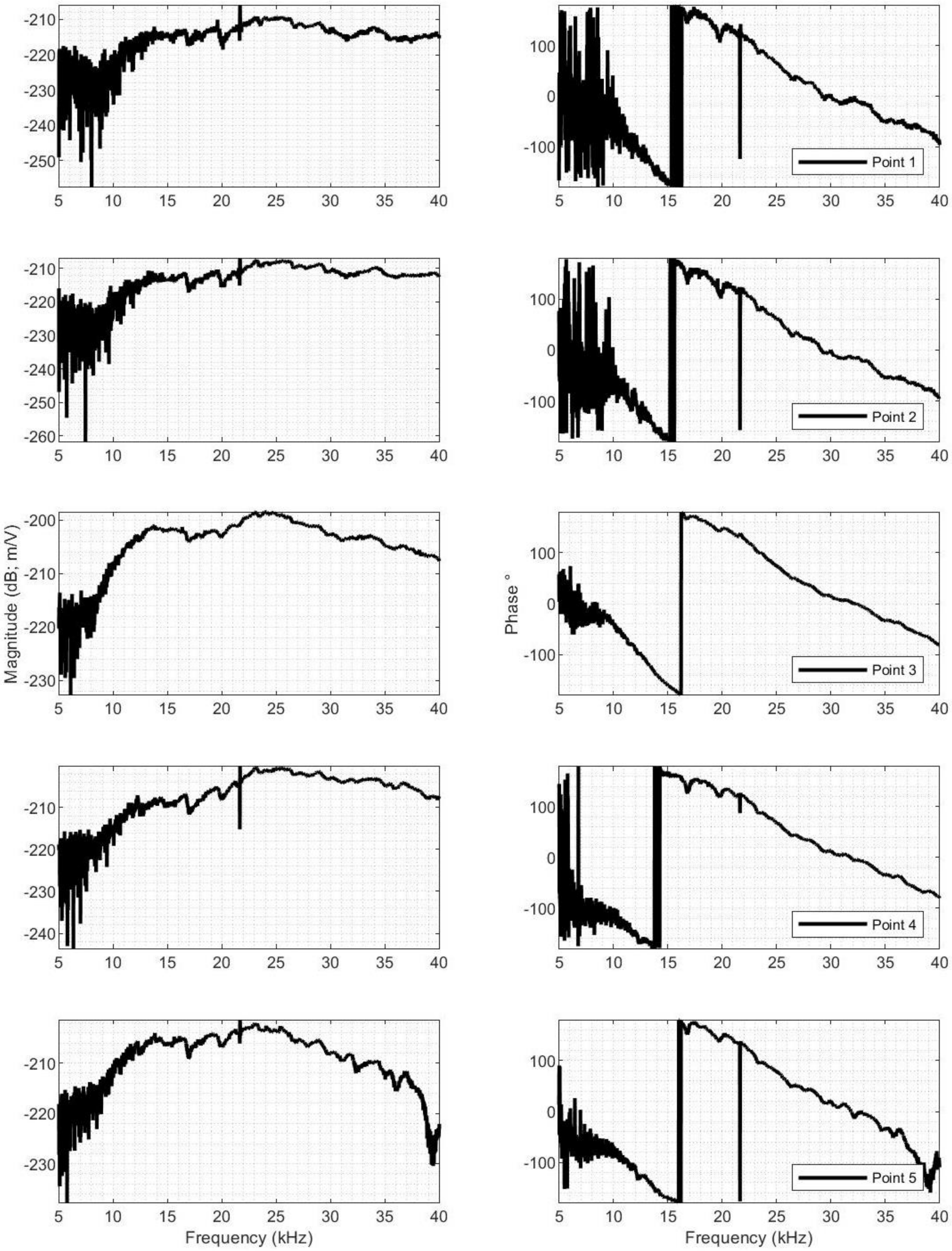
Magnitude (dB; m/V)
Phase °
Frequency (kHz)
Frequency (kHz)
5
10
15
20
25
30
35
40
-210
-220
-230
-240
-250
-260
-200
100
0
-100
Point 1
Point 2
Point 3
Point 4
Point 5

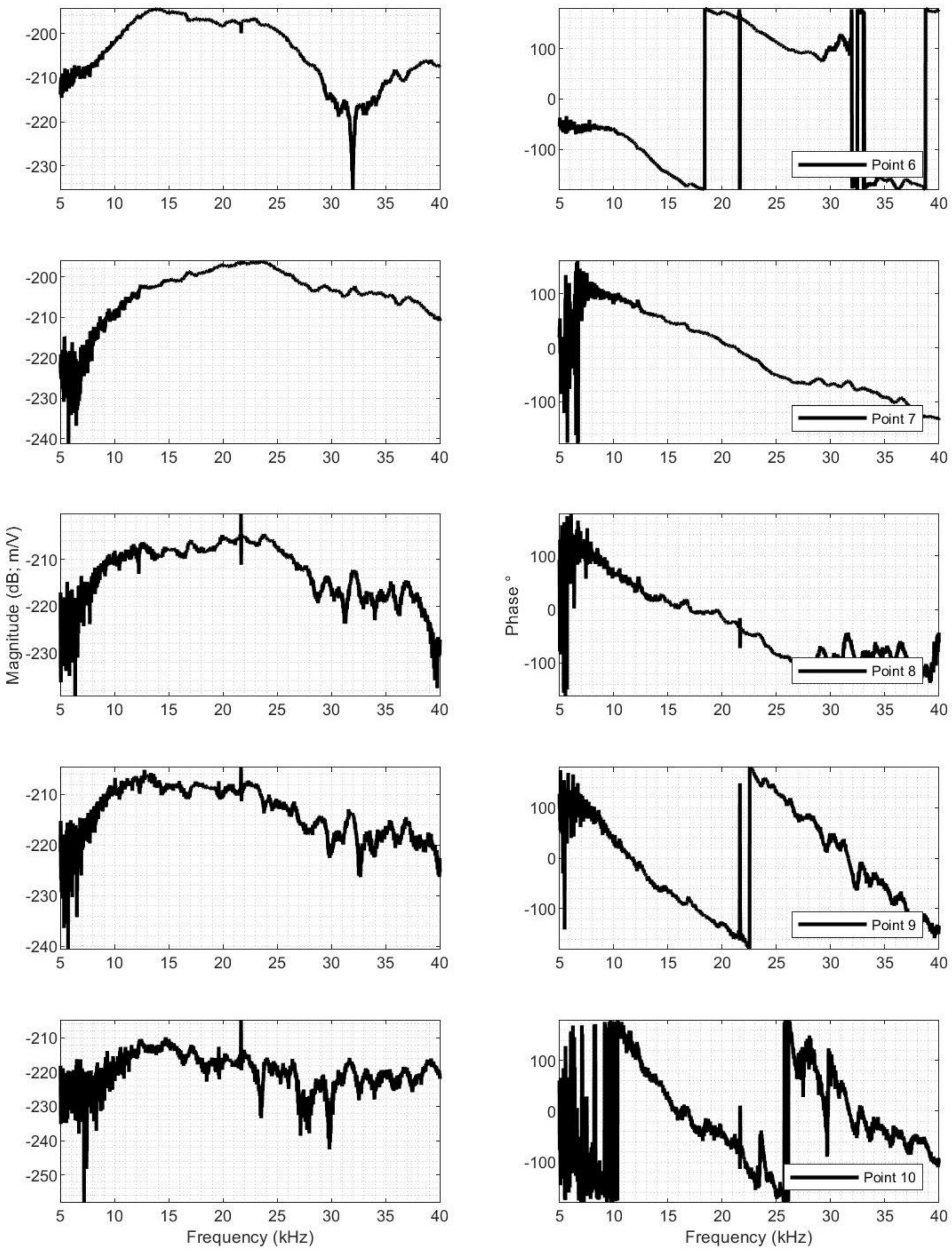
Magnitude (dB; m/V)
Phase °
Point 6
Point 7
Point 8
Point 9
Point 10
-200
-210
-220
-230
-240
-250
100
0
-100
5
10
15
20
25
30
35
40
Frequency (kHz)
Frequency (kHz)

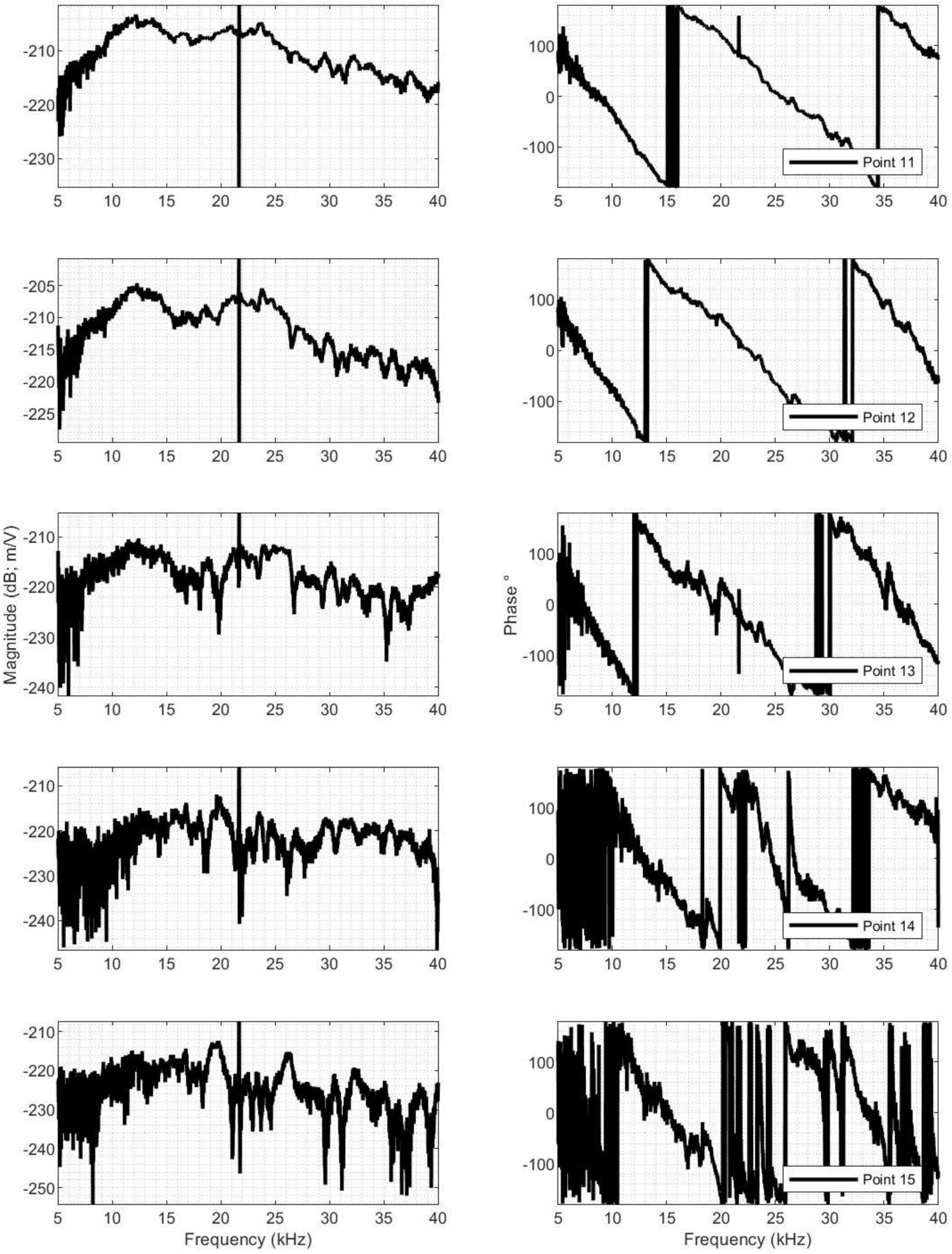
Magnitude (dB; m/V)
-210
-220
-230
-205
-215
-225
-240
-250
Phase °
100
0
-100
Point 11
Point 12
Point 13
Point 14
Point 15
5
10
15
20
25
30
35
40
Frequency (kHz)
Frequency (kHz)

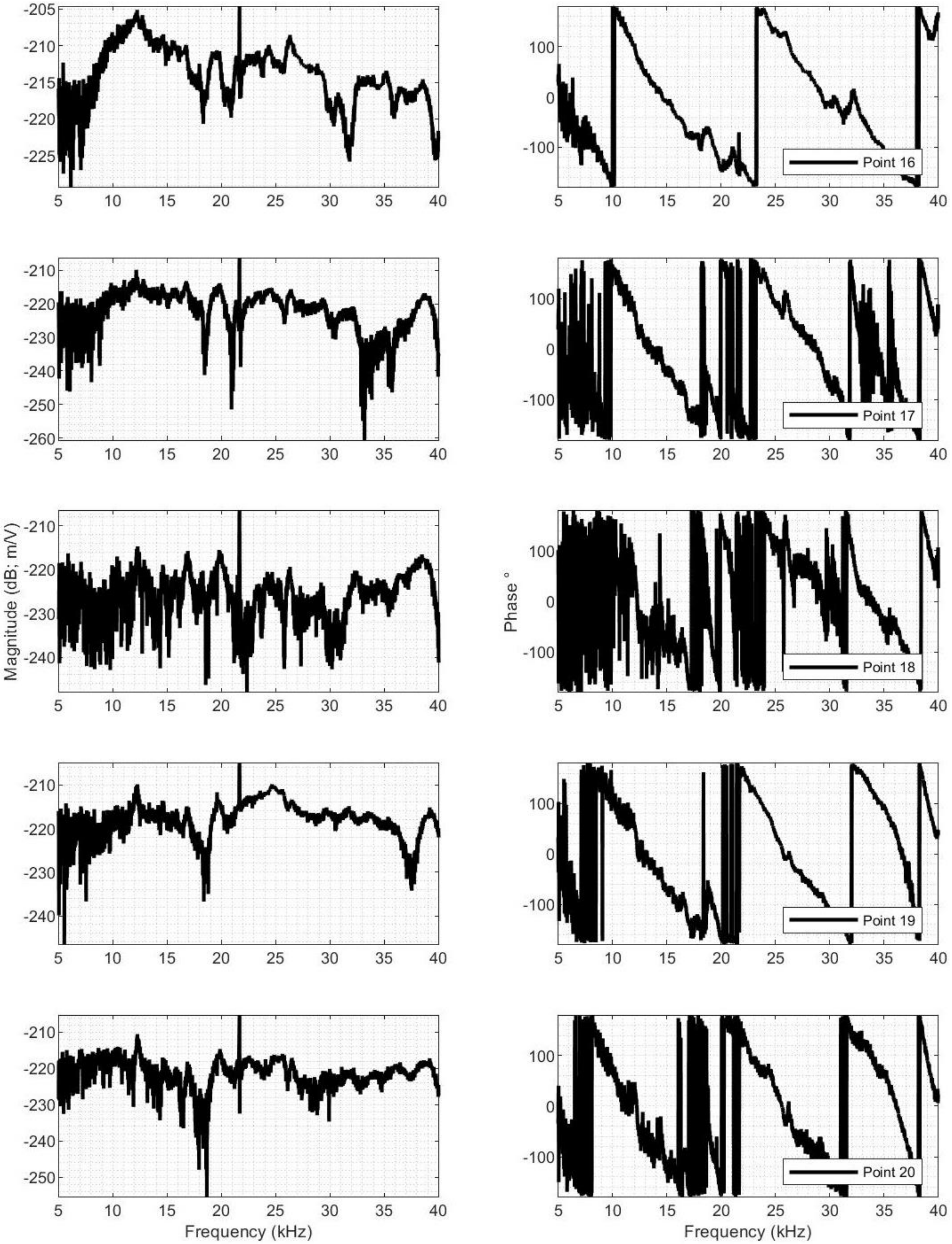
Magnitude (dB; m/V)
Phase °
Frequency (kHz)
Frequency (kHz)
5
10
15
20
25
30
35
40
-205
-210
-215
-220
-225
-230
-240
-250
-260
100
0
-100
Point 16
Point 17
Point 18
Point 19
Point 20

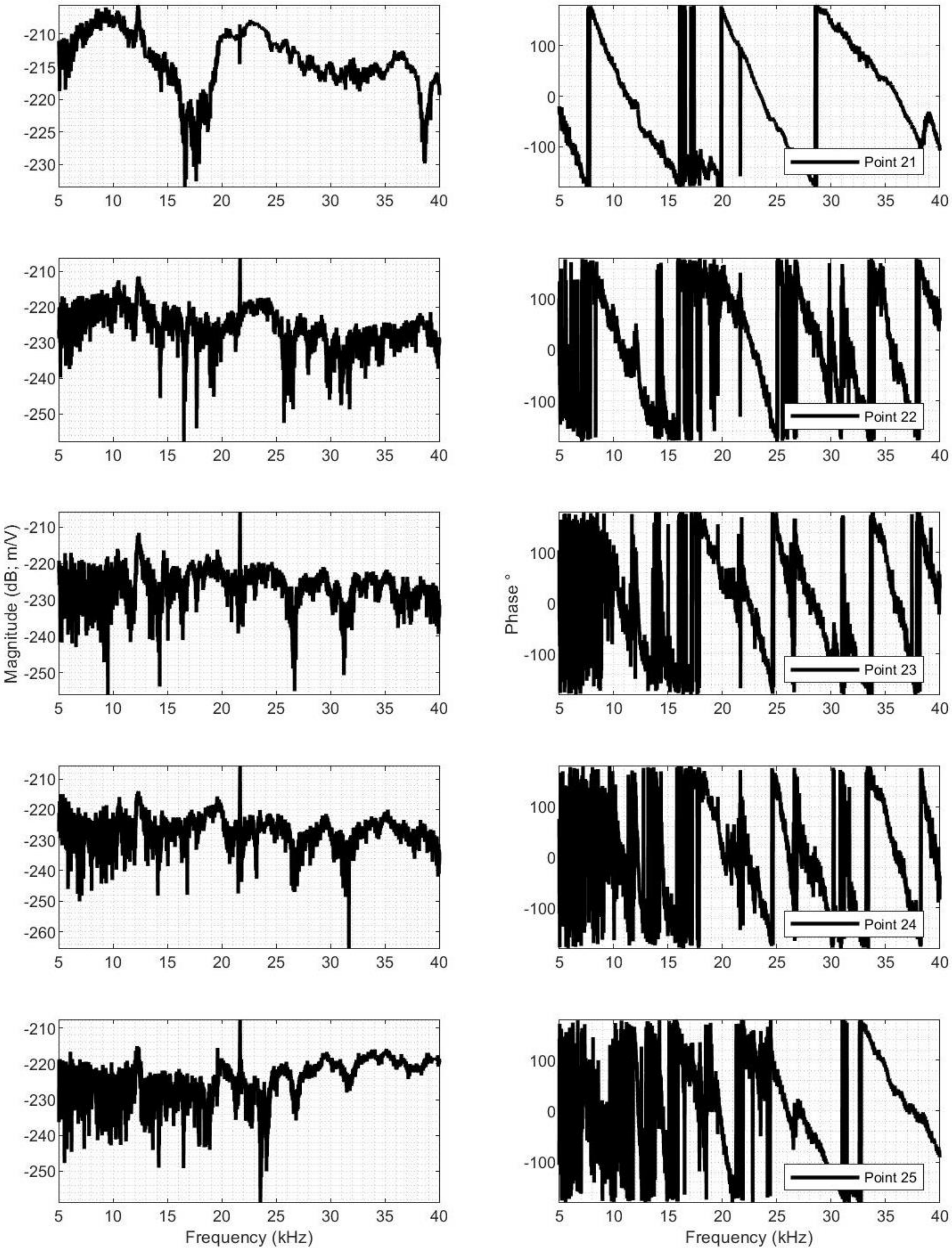
Magnitude (dB; m/V)
Phase °
Frequency (kHz)
Frequency (kHz)
Point 21
Point 22
Point 23
Point 24
Point 25
-210
-215
-220
-225
-230
-240
-250
-260
100
0
-100
5
10
15
20
25
30
35
40

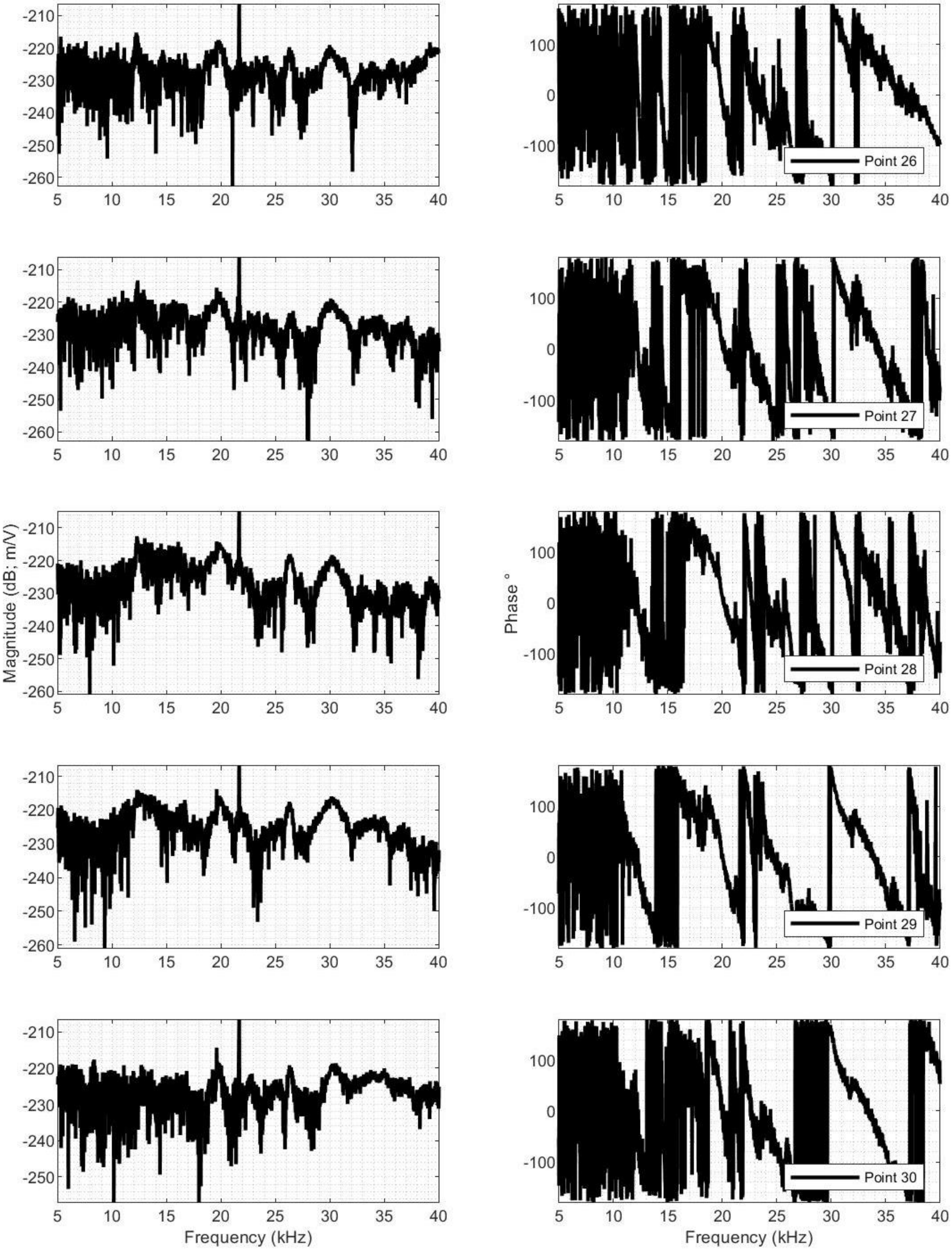
Magnitude (dB; m/V)
-210
-220
-230
-240
-250
-260
Phase °
100
0
-100
Point 26
Point 27
Point 28
Point 29
Point 30
5
10
15
20
25
30
35
40
Frequency (kHz)
Frequency (kHz)

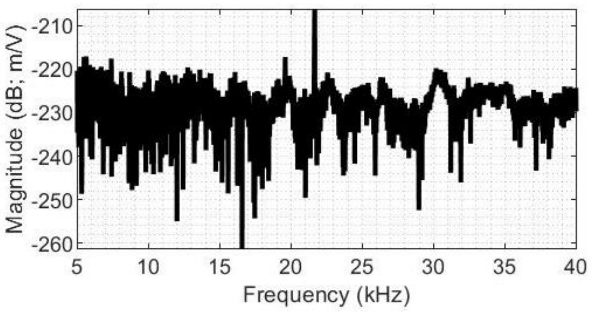
Magnitude (dB; m/V)
-210
-220
-230
-240
-250
-260
5
10
15
20
25
30
35
40
Frequency (kHz)

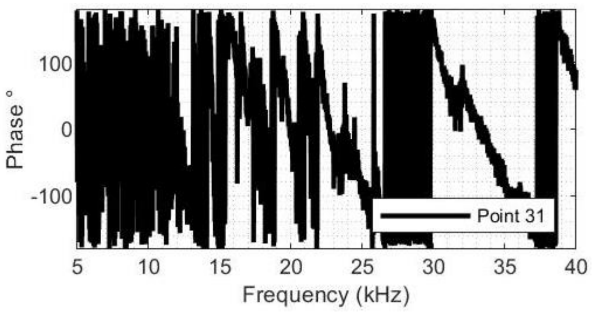
Phase °
100
0
-100
Point 31
5
10
15
20
25
30
35
40
Frequency (kHz)

APPENDIX D

MATLAB CODE

- ✓ Scripts used to process raw data

```
function [Data] = CombineASC(Filename_1, Filename_2, Filename)
% The magnitude and phase of the FRF was saved using frequency analyzer in
% two separate files. This function was used to combine magnitude and phase
% data into a single file.
% Filename_1 -  asc file containing frequency and amplitude data ('1.asc').
% Filename_2 -  asc file containing frequency and phase data from the same
%               measurement ('2.asc').
% Filename -    desired filename 'Experiment_1.asc'
% The resulting file contains 3 columns: 1st - Frequency in Hz,
% 2nd - Amplitude on linear scale (V/V), 3rd - phase angle in degrees.
% The example of the call: CombineASC('1.asc', '2.asc', 'Experiment_1.asc')
Amplitude = textread(Filename_1,'','headerlines',17);
Phase = textread(Filename_2,'','headerlines',17);
Data = [Amplitude(:,1:2) Phase(:,2)];
save(Filename,'Data','-ascii');
end


% The script was used to process raw FRF for further analysis. The example
% shown was used to process data related to the actuator 2
% In particular:
% - all FRF measurement related to a single actuator were saved in a single
% cell array
% - the data was adjusted for the time delay caused by the LDV
% - the phase of all FRF measurements was adjusted to be withing [-180 180]
% degrees interval
% - the data was converted to the velocity, position, or acceleration
% depending on the need, and saved together with the location of
% measurement points in the .mat file
% Actuator measurements
clear all; close all; clc;
RawDataA(:,:,1) = textread('Actuator 2\Air_1.asc');
RawDataA(:,:,2) = textread('Actuator 2\Air_2.asc');
RawDataA(:,:,3) = textread('Actuator 2\Oil_1.asc');
RawDataA(:,:,4) = textread('Actuator 2\Oil_2.asc');
RawDataA(:,:,5) = textread('Actuator 2\Oil_3.asc');
RawDataA(:,:,6) = textread('Actuator 2\Oil_4.asc');
RawDataA(:,:,7) = textread('Actuator 2\Oil_5.asc');
RawDataA(:,:,8) = textread('Actuator 2\Oil_6.asc');
RawDataA(:,:,9) = textread('Actuator 2\Oil_in_1.asc');
RawDataA(:,:,10) = textread('Actuator 2\Oil_in_2.asc');
RawDataA(:,:,11) = textread('Actuator 2\Oil_in_3.asc');
RawDataA(:,:,12) = textread('Actuator 2\Oil_in_4.asc');
RawDataA(:,:,13) = textread('Actuator 2\Oil_in_5.asc');
RawDataA(:,:,14) = textread('Actuator 2\Oil_in_6.asc');
```

```
LegA = {'Actuator 2 - Air HF5', 'Actuator 2 - Air HF5 SV200',...
        'Actuator 2 - Oil HF5', 'Actuator 2 - Oil HF5 SV200',...
        'Actuator 2 - Oil PLL5 SV200', 'Actuator 2 - Oil PLL1 SV200',...
        'Actuator 2 - Oil HF5 SV200 DP', 'Actuator 2 - Oil PLL1 SV200 No
fixture',...
        'Actuator 2 - Oil In HF5', 'Actuator 2 - Oil In HF5 DP',...
        'Actuator 2 - Oil In HF5 DP', 'Actuator 2 - Oil In PLL5',...
        'Actuator 2 - Oil In PLL1', 'Actuator 2 - Oil In HF5 Beam'};

% Adjusting phase for the time delay caused by vibrometer
RawDataA(:,3,[1:4,7,9:11,14]) = RawDataA(:,3,[1:4,7,9:11,14]) + ...
         0.0023*RawDataA(:,1,[1:4,7,9:11,14]); % HF 5
RawDataA(:,3,[5,12]) = RawDataA(:,3,[5,12]) + ...
         0.00256*RawDataA(:,1,[5,12]);      % PLL 5
RawDataA(:,3,[6,8,13]) = RawDataA(:,3,[6,8,13]) + ...
         0.0086*RawDataA(:,1,[6,8,13]);     % PLL 1

% Adjusting phase for measurements taken inside the setup from the back
RawDataA(:,3,9:10) = RawDataA(:,3,9:10) + 180; % Oil In
% 11-14 are left unchanged to make data look consistent

for k = 1:length(RawDataA(1,1,:))           % Adjusting phase [-180 180]
    for n = 1:length(RawDataA(:,3,k))
        while RawDataA(n,3,k) > 180
            RawDataA(n,3,k) = RawDataA(n,3,k) - 360;
        end
        while RawDataA(n,3,k) < -180
            RawDataA(n,3,k) = RawDataA(n,3,k) + 360;
        end
    end
end

% Converting to velocity m/s/V
DataVa = RawDataA;
DataVa(:,2,[1:5,7,9:12,14]) = DataVa(:,2,[1:5,7,9:12,14])*0.005; % 5 mm/s/v
range
DataVa(:,2,[6,8,13]) = DataVa(:,2,[6,8,13])*0.001; % 1 mm/s/v range

% Converting velocity FRF to dispacement FRF (m/V)
DataYa = DataVa;
DataYa(:,2,:) = DataYa(:,2,:)./(2*pi*DataYa(:,1,:)); % Converting magnitude
DataYa(:,3,:) = DataYa(:,3,:) - 90;          % Adjusting phase
for k = 1:length(DataYa(1,1,:))              % Adjusting phase [-180 180]
    for n = 1:length(DataYa(:,3,k))
        while DataYa(n,3,k) > 180
            DataYa(n,3,k) = DataYa(n,3,k) - 360;
        end
        while DataYa(n,3,k) < -180
            DataYa(n,3,k) = DataYa(n,3,k) + 360;
        end
    end
end

% Converting velocity FRF to accelaration FRF (m/s^2/V)
DataAa = DataVa;
DataAa(:,2,:) = DataAa(:,2,:).*(2*pi*DataAa(:,1,:)); % Converting magnitude
```

```
DataAa(:,3,:) = DataAa(:,3,:) + 90;          % Adjusting phase
for k = 1:length(DataAa(1,1,:))              % Adjusting phase [-180 180]
    for n = 1:length(DataAa(:,3,k))
        while DataAa(n,3,k) > 180
            DataAa(n,3,k) = DataAa(n,3,k) - 360;
        end
        while DataAa(n,3,k) < -180
            DataAa(n,3,k) = DataAa(n,3,k) + 360;
        end
    end
end

% Converting to format used in analysis
for k = 1:length(RawDataA(1,1,:))
    Va{k,1} = DataVa(:,:,k); Va{k,2} = LegA{k};
    Ya{k,1} = DataYa(:,:,k); Ya{k,2} = LegA{k};
    Aa{k,1} = DataVa(:,:,k); Aa{k,2} = LegA{k};
end

%% Membrane measurements
for k = 1:31
    filename = sprintf('Actuator 2\\Point_%i.asc', k-1);
    A = textread(filename,'');
    RawDataM(:,:,k) = A;
    LegM{k} = sprintf('Point %d', k);
end

% % Removing spike at 21647 and 21659 Hz
% [~, i] = min(abs(RawDataM(:,1,1)-21647));
% for k = 1:length(RawDataM(1,1,:))
%     RawDataM(i,2,k) = RawDataM(i+3,2,k);
%     RawDataM(i,3,k) = RawDataM(i+3,3,k);
% end
% [~, i] = min(abs(RawDataM(:,1,1)-21659));
% for k = 1:length(RawDataM(1,1,:))
%     RawDataM(i,2,k) = RawDataM(i+3,2,k);
%     RawDataM(i,3,k) = RawDataM(i+3,3,k);
% end

% Adjusting phase for the time delay caused by vibrometer
RawDataM(:,3,:) = RawDataM(:,3,:) + 0.00256*RawDataM(:,1,:);
for k = 1:length(RawDataM(1,1,:))            % Adjusting phase [-180 180]
    for n = 1:length(RawDataM(:,3,k))
        while RawDataM(n,3,k) > 180
            RawDataM(n,3,k) = RawDataM(n,3,k) - 360;
        end
        while RawDataM(n,3,k) < -180
            RawDataM(n,3,k) = RawDataM(n,3,k) + 360;
        end
    end
end

% Converting to velocity m/s/V
DataVm = RawDataM;
DataVm(:,2,:) = DataVm(:,2,:)*0.005;         % 5 mm/s/v range

% Converting velocity FRF to displacement FRF (m/V)
```

```
DataYm = DataVm;
DataYm(:,2,:) = DataYm(:,2,:)./(2*pi*DataYm(:,1,:)); % Converting magnitude
DataYm(:,3,:) = DataYm(:,3,:) - 90;          % Adjusting phase
for k = 1:length(DataYm(1,1,:))              % Adjusting phase [-180 180]
    for n = 1:length(DataYm(:,3,k))
        while DataYm(n,3,k) > 180
            DataYm(n,3,k) = DataYm(n,3,k) - 360;
        end
        while DataYm(n,3,k) < -180
            DataYm(n,3,k) = DataYm(n,3,k) + 360;
        end
    end
end

% Converting to format used in analysis
for k = 1:length(RawDataM(1,1,:))
    Vm{k,1} = DataVm(:,:,k); Vm{k,2} = LegM{k};
    Ym{k,1} = DataYm(:,:,k); Ym{k,2} = LegM{k};
    Am{k,1} = DataVm(:,:,k); Am{k,2} = LegM{k};
end

% Combininf data
V = [Vm;Va];
Y = [Ym;Ya];
A = [Am;Aa];

% Coordinates of the points
X2 = [0.5 1:14 15.1 16:23 23.54 24.9 26 27.03 28:29 29.45];

%% Saving data
Actuator_2 = Y;
save('Actuator 2.mat', 'Actuator_2', 'X2');
```

✓ Scripts used to extract vibration mode shapes of the membrane

```
clear all; close all; clc;
addpath('Functions/');
load('ExpData\Actuator 1B.mat');
load('ExpData\Actuator 2.mat');
load('ExpData\Actuator 3.mat');
[MS_PCA1,MS1,F1,U1,S1,V1,R1,RC1,VarR1,VarC1] = PCA_A(Actuator_1,[],X1,29,5);
[MS_PCA2,MS2,F2,U2,S2,V2,R2,RC2,VarR2,VarC2] = PCA_A(Actuator_2,[],X2,31,5);
[MS_PCA3,MS3,F3,U3,S3,V3,R3,RC3,VarR3,VarC3] = PCA_A(Actuator_3,[],X3,31,5);
[MS_E1,RE1,Var_RE1] = PCA_E(MS_PCA1,F1,X1,[]);
[MS_E2,RE2,Var_RE2] = PCA_E(MS_PCA2,F2,X2,[]);
[MS_E3,RE3,Var_RE3] = PCA_E(MS_PCA3,F3,X3,[]);

%% Movie
close all; clc;
% PlotMS(X1,F1,MS1,MS_PCA1,MS_E1,'Y');
PlotMS(X2,F2,MS2,MS_PCA2,MS_E2,'Y');
% PlotMS(X3,F2,MS3,MS_PCA3,MS_E3,'N');

function [MS_PCA,MS,F,U,S,V,R,R_C,Var_R,Var_C] = PCA_A(Data,W,X,NP,NC)
% PCA_A approximates the matrix with the membrane's modeshapes
% MS - matrix of modeshapes
```

```
% MS_PCA - matrix of modeshapes reconstructed using NC principal components
% F - frequency corresponding to MS and MS_PCA
% U,V,S - SVD decomposition of MS
% Data - cell array of experimental data
% W - range of frequency to use for analysis (if empty - use all data)
% X - coordinate of measurement points
% NP - number of points to use (Max 29 for A1; 31 for A2 and A3)
% NC - number of components to use in approximation
% Flag - 'Y' to save figure

if ~isempty(W)                                  % If W(w1,w2) is given
    [~, IL] = min(abs(Data{1,1}(:,1)-W(1)));    % Lower bound in Data
    [~, IU] = min(abs(Data{1,1}(:,1)-W(end)));  % Upper bound in Data
    for k = 1:NP
        Data{k,1}([1:IL-1 IU+1:end],:) = [];    % Truncating Data
    end
end

for k = 1:NP
    f(k,:) = Data{k,1}(:,1);                    % Frequency
    M(k,:) = Data{k,1}(:,2);                    % Magnitude
    P(k,:) = Data{k,1}(:,3);                    % Phase angle
end
F = f(1,:);
MS = M.*cosd(P);                                % Modeshapes
[U,S,V] = svd(MS,'econ');                       % SVD
MS_PCA = U(:,1:NC)*S(1:NC,1:NC)*V(:,1:NC)';     % Approximated modeshapes

Var = diag(S).^2/(NP-1);                        % Variance

for k = 1:10
    R(k) = 100*S(k,k)/sum(diag(S));             % Ratio
    R_C(k) = 100*sum(diag(S(1:k,1:k)))/sum(diag(S)); % Cumulative ratio
    Var_R(k) = 100*Var(k)/sum(Var);             % Relative variance
    Var_C(k) = 100*sum(Var(1:k))/sum(Var);      % Cumulative variance
end

figure();
subplot(5,4,[1:2]); plot(diag(S)/S(1,1),'.','Markersize',20);
ylabel('S'); grid minor; axis tight;
sgtitle('Principal Components');
for k = 1:9
    subplot(5,4,2*k+1); plot(X(1:NP), U(:,k),'linewidth',2);
    grid minor; axis tight; ylabel(['U', num2str(k)]);
    set(gca,'XTickLabels',[])
    if k == 8 || k == 9
        xticklabels('auto'); xlabel('X (mm)');
    end
    subplot(5,4,2*k+2);
    plot(F/1000,V(:,k),'linewidth',2);
    grid minor; axis tight; ylabel(['V', num2str(k)]);
    set(gca,'XTickLabels',[])
    if k == 8 || k == 9
        xticklabels('auto'); xlabel('Frequency (kHz)');
    end
end
end
```

```
function [MS_E,RE,Var_RE] = PCA_E(MS,F,X,W)
% PCA_E extract particular modeshape from the matrix
% MS - matrix of modeshapes
% F - frequency vector corresponding to MS
% W - frequency of interest (if empty - extract all)
a = 50;                                         % 2a measurements to use
if ~isempty(W)                                  % If W is given
    [~,Ind] = min(abs(F-W));                    % Coresponding index
    [U,S,V] = svd(MS(:,Ind-a:Ind+a),'econ');    % SVD
    MS_E = mean(U(:,1)*S(1,1)*V(:,1)',2);       % Approximated modeshapes
    RE = 100*S(1,1)/sum(diag(S));                % Ratio
    Var = diag(S).^2/(length(MS(:,1))-1);       % Variance
    Var_RE = 100*Var(1)/sum(Var);                % Relative variance
    figure();
    subplot(6,2,1:2);
    X_L = categorical({'R','\sigma^2'});
    bar(X_L,[RE; Var_RE]); grid minor; ylim([80,100]);
    legend(['R = ',num2str(RE,3),' %'],'Location','NorthWest');
    subplot(6,2,3:4);
    plot(X,MS_E,'linewidth',2); grid minor; axis tight; ylabel('MS');
    legend([num2str(F(Ind)/1000,3),' kHz'],'Location','SouthEast');
    for k = 1:4
        subplot(6,2,2*k+3); plot(X, U(:,k),'linewidth',2);
        grid minor; axis tight; ylabel(['U', num2str(k)]);
        set(gca,'XTickLabels',[])
        if k == 4
            xticklabels('auto'); xlabel('X (mm)');
        end
        subplot(6,2,2*k+4);
        plot(F(Ind-a:Ind+a)/1000,V(:,k),'linewidth',2);
        grid minor; axis tight; ylabel(['V', num2str(k)]);
        set(gca,'XTickLabels',[])
        if k == 4
            xticklabels('auto'); xlabel('Frequency (kHz)');
        end
    end
else
    for k = 1:length(MS(1,:))
        if k <= a
            [U,S,V] = svd(MS(:,1:2*a),'econ');          % SVD
        elseif k + a > length(MS(1,:))
            [U,S,V] = svd(MS(:,end-2*a:end),'econ');% SVD
        else
            [U,S,V] = svd(MS(:,k-a:k+a),'econ');        % SVD
        end
        MS_E(:,k) = mean(U(:,1)*S(1,1)*V(:,1)',2);  % Approximated modeshapes
        RE(k) = 100*S(1,1)/sum(diag(S));             % Ratio
        Var = diag(S).^2/(length(MS(:,1))-1);       % Variance
        Var_RE(k) = 100*Var(1)/sum(Var);             % Relative variance
    end
end
end
```

```
%% PlotMS
% Function used to search for eigenmodes
function [] = PlotMS(X,F,MS,MS_PCA,MS_E,Flag)
if Flag == 'Y'
    VideoObject = VideoWriter('Shapes', 'MPEG-4');
    VideoObject.Quality = 100;
    VideoObject.FrameRate = 25;
    open(VideoObject);
end
figure();
for k = 1:length(F)
    plot([0,X,30], 1e9*[0;MS_E(:,k);0], 'b-', 'linewidth', 4); hold on;
    plot([0,X,30], 1e9*[0;MS(:,k);0], 'r-', 'linewidth', 2);
    %plot([0,X,30], 1e9*[0;MS_PCA(:,k);0], 'k-', 'linewidth', 2);
    plot([0,X,30], zeros(size(X)+2), 'k.', 'Markersize',5)
    xlabel('X (mm)'); ylabel('Y (nm/V)'); grid minor; axis tight;
    legend([num2str(F(k)/1000,4),' kHz']); hold off;
    pause(0.01);
    if Flag == 'Y'
        currFrame = getframe;
        writeVideo(VideoObject,currFrame);
    end
end
if Flag == 'Y'
    close(VideoObject);
end
end
```